PREDICTING AND TESTING THE PERFORMANCE

OF NEXT GENERATION HEAT EXCHANGERS WITH

LOW-GWP REFRIGERANTS

By

SAAD SALEEM

Bachelor of Science in Mechanical Engineering
University of Engineering and Technology (UET), Lahore
Pakistan
2013

Master of Science in Renewable Energy
(InnoEnergy Double Degree Program)
Polytechnic University of Catalonia (UPC)
Spain
2016
KTH Royal Institute of Technology
Sweden
2015

Submitted to the Faculty of the
Graduate College of the
Oklahoma State University
in partial fulfillment of
the requirements for
the Degree of
DOCTOR OF PHILOSOPHY
December, 2021

PREDICTING AND TESTING THE PERFORMANCE OF

NEXT GENERATION HEAT EXCHANGERS WITH

LOW-GWP REFRIGERANTS

Dissertation Approved:

Dr. Craig R. Bradshaw

Dissertation Adviser

Dr. Christian K. Bach

Dr. Jeffrey D. Spitler

Dr. Jindal Shah

ACKNOWLEDGEMENTS

The work in my PhD dissertation has been made possible by many wonderful people, either directly or indirectly, and I want to express my gratitude to all of them. First and foremost, my family, who have always encouraged me to excel in my academic and professional career and supported me through all the highs and lows of my journey at OSU.

I could not have asked for a better and more patient advisor than Dr. Craig Bradshaw. His training, and guidance has been invaluable, and has made me grow tremendously during my doctoral studies. I am honored to call him my mentor, teacher, and friend.

Thank you, Dr. Christian Bach, for being my informal advisor. I have learnt a lot from you, and I am glad for all your guidance and support. I am thankful to my committee members, Dr. Jeffrey Spitler, and Dr. Jindal Shah for their advice and assistance in my work.

My fellow lab mates and friends have been a big part of my journey. I will definitely miss all our trips for conferences, and the lunches we had every Friday. Thank you, Omer Sarfraz, Abraham Lee, Seth Yarborough, Kalen Gabel, Andrew Quinton, Mazharul Islam and Mohsin Tanveer, for all the wonderful memories we have shared together at OSU.

Name: SAAD SALEEM

Date of Degree: December, 2021

Title of Study: PREDICTING & TESTING THE PERFORMANCE OF NEXT GENERATION
HEAT EXCHANGERS WITH LOW-GWP REFRIGERANTS

Major Field: Mechanical Engineering

Abstract: Energy efficiency regulations are forcing air conditioning (AC) and heat pump (HP) manufacturers to replace existing high global warming potential (GWP) refrigerants in their systems with more climate friendly alternatives. Air-to-refrigerant fin-and-tube heat exchangers (FTHXs), and water-to-refrigerant coaxial heat exchangers are commonly found in residential and commercial AC and HPs. To adapt to these new refrigerants, heat exchanger manufacturers need to make design changes in their equipment, in order to ensure that the next generations of their products is energy efficient, climate friendly, and cost effective. This thesis aims to develop a set of guidelines for pseudo-optimal design of FTHXs in order to accommodate the next generation of low-GWP refrigerants, with the goal to obtain near optimal performance under current manufacturing constraints.

A novel pumped refrigerant loop was developed, and coupled with an airside setup and a psychrometric chamber facility, to test FTHXs. The experimental facility was used for validating a segment-by-segment heat exchanger model called cross-fin (Xfin), by comparing model predictions against data collected from three custom designed FTHXs with distinct refrigerant circuitries. The mean absolute percentage error (MAPE) between the experimental, and model predicted capacities was found to be 1.0%, 2.4%, and 0.9%, for the interleaved, vertical, and block circuited FTHXs, respectively. A preliminary simulation study was performed using a four-component HP model to investigate the change in system performance metrics of an R410A based water-to-water HP, using R454B and R452B as low-GWP "drop-in" alternatives. A four-component heat pump model, validated against the performance datasheet, was used for simulations and showed that some design changes may be necessary to existing equipment, in order to adapt them for near optimum performance with low-GWP fluids. Then, Xfin model predictions were compared against experiments performed on the block circuited FTHX with R1234ze(E). The MAPE between the experimental and model predicted capacities was found to be 1.4%. A parametric simulation study was done by modifying the refrigerant circuitry and fin pitch, showing that FTHX performance metrics such as capacity ($\dot{Q}_{evap}$) and refrigerant pressure drop (ΔP_{ref}), are influenced by changes in geometry. Finally, simulations were executed to compare the performance of R1234yf and R1234ze(E) on the R410A based block circuited indoor evaporator FTHX. It was found that the performance, in terms of the ratio $\dot{Q}_{evap}/\Delta P_{ref}$, was most sensitive to the number of circuits, followed by the tube diameter, number of tubes in the FTHX, and the fin density. Based on the simulation results, two customized FTHX designs were suggested, with different changes to the FTHX slab size. One design prioritized increased FTHX capacity, and the other prioritized reduction in refrigerant pressure drop to acceptable limits.

TABLE OF CONTENTS

LIST OF FIGURES

LIST OF TABLES

NOMENCLATURE

3D …….......	Three dimensional
AC ………..	Air conditioning
AHRI ……..	Air conditioning, Heating and Refrigeration Institute
AIM ………	American Innovation and Manufacturing
ASHRAE …	American Society of Heating, Refrigeration and Air Conditioning Engineers
BPHE ……..	Brazed plate heat exchanger
CAD …........	Computer aided design
CFC ……….	Chlorofluorocarbon
CFD ……….	Computational Fluid Dynamics
CFM …........	Cubic feet per minute
CO_2 ….........	Carbon dioxide
COP ….........	Coefficient of Performance
DAQ …........	Data acquisition system
DB ………...	Dry bulb
DOE……….	Department of Energy
EER ….........	Energy Efficiency Ratio
EES ……….	Engineering Equation Solver
EIA ……….	Energy Information Administration
EPA ……….	Environmental Protection Agency
EU ………...	European Union
Evap……….	Evaporator
Exp.……….	Experimental
EWT ……...	Entering Water Temperature
EXV ……...	Expansion valve
FPI ……….	Fins Per Inch
FS …….......	Full scale
FTHX ……	Fin-and-tube heat exchanger
GHG ……...	Greenhouse Gas
GWP ……..	Global Warming Potential
HVAC ….....	Heating, Ventilation and Air Conditioning
HFC ……...	Hydrofluorocarbon
HFO ……...	Hydrofluoroolefin
HCFC …….	Hydro chlorofluorocarbon

HP…………	Heat pump
HPDM…….	Heat Pump Design Model
HPWH ……	Heat pump water heater
ISHED ……	Intelligent System for Heat Exchanger Design
MAE ……..	Mean Error
MAPE ……..	Mean Absolute Percent Error
N …………	Number of active circuits
N/A ………	Not available
ND ……….	Nozzle Diameter
NTU ……...	Number of Transfer Units
OD ………..	Outside tube diameter (m)
ORNL……..	Oak Ridge National Laboratory
POE ………	Polyolester
PPTD ……..	Pinch point temperature difference
RTD ………	Resistance temperature detector
RTU ………	Rooftop air conditioner
SC ……......	Subcooling (K)
SCR ………	Silicon-controlled rectifier
SH ……......	Superheating (K)
SST ………	Saturated suction temperature (°C)
TEWI ……	Total Equivalent Warming Impact (kg of CO_2 equivalent)
TP ………..	Two phase
TXV ……...	Thermostatic expansion valve
VFD ……...	Variable frequency drive
VRF ……...	Variable Refrigerant Flow
WB ………	Wet bulb
WCRS ….....	Walk-in cooler refrigeration system
VRF ………	Variable Refrigerant Flow
ΔP ………...	Pressure drop (kPa)
A ………….	Area (m^2)
C ………….	Capacitance (J/K)
D ………….	Diameter (m)
ε …………..	Heat exchanger effectiveness
f_Q …………	Heat loss factor for compressor
h ………….	Enthalpy (kJ/kg)
h_{fg} ……….	Latent heat of vaporization, kJ/kg
L ………….	Length (m)
$\dot{m}$ ………….	Mass flow rate (kg/s)
μ …………..	Viscosity (µPas)
N ………….	Number
$\dot{Q}$ ………….	Heat transfer, capacity (W)
ρ ………….	Density (kg/m^3)

T ………….	Temperature (°C)
U ………….	Overall heat transfer coefficient (kW/m^2-K)
$\dot{W}$ …………	Work (kW)
v, V ……….	Velocity (m/s)
V_{disp} ………	Volumetric displacement (m^3)
ω …………	Rotational speed (rad/s)
Xfin ………	Cross-fin

Subscripts/Superscripts

a, air ………	Air
aht ………...	After heat exchanger
avg ………..	Average
bht ………..	Before heat exchanger
$coax$ ……...	Coaxial heat exchanger
$c, cond$ …...	Condenser
$comp$ ……..	Compressor
$e, evap$ …...	Evaporator
exp ………..	Experimental
f ………….	Saturated liquid
g ………….	Saturated vapor
i …………..	Circuit number
in ……….	Inlet
iso, s ……..	Isentropic
l ………….	Liquid
min ……...	Minimum
o, out ……..	Outlet
r, ref ……...	Refrigerant
sat ……......	Saturated
sim ……….	Model predicted
suc ……......	Suction
sup ……......	Superheat
v ………….	Vapor
1 ……...........	State point 1 - Suction of compressor
2 ……...........	State point 2 - Discharge of compressor

3 ……........... State point 3 - Exit of condenser

4 ……........... State point 4 - Inlet of evaporator

Greek symbols

λ ……........... Ratio of active tubes to total number of tubes in test coil

α ……........... Ratio of active tubes with 1st order neighboring inactive tubes to inactive tubes with 1st order neighboring active tubes

CHAPTER I

INTRODUCTION

According to several studies, *e.g.*, US Environmental Protection Agency, (1989), people in North America and Europe spend 90% of their time indoors in buildings. In other developed countries around the world, such as the United Arab Emirates, this could amount to 99.9% for some people, owing to the weather conditions. Thermal comfort inside these buildings is provided by heat pumps, air conditioners (ACs), or chillers, for which the vapor compression system is most widely used. The two heat exchangers inside a simple vapor compression cycle, namely the evaporator and condenser, are responsible for providing heating and/or cooling in the building. These evaporators and condensers could either be liquid-to-refrigerant heat exchangers, or air-to-refrigerant heat exchangers, depending upon the application.

The majority of refrigerants inside heat pumps and AC systems today are hydrofluorocarbons (HFCs), such as R410A (McLinden & Huber, 2020). Leakage of these refrigerants from the systems contributes to climate change globally, due to their high Global Warming Potential (GWP). Several regulatory measures are forcing manufacturers of vapor compression systems, including those of heat exchangers, to replace these high GWP refrigerants with more climate friendly alternatives, such as the hydrofluoroolefins (HFOs) R1234yf and R1234ze(E). Manufacturers thus need to adapt their existing equipment to these new low-GWP fluids, to ensure their new line of products are cost

effective, energy efficient, and environment friendly at the same time. Thus, it is critical to understand the influence of these new low-GWP refrigerants on the thermodynamic performance existing heat exchangers. A cost effective and intuitive method to understand this is by numerical modelling of these heat exchangers with the new refrigerants. Parametric simulations can be executed once a model is developed, to observe if heat exchanger performance can be enhanced by modifying geometry. Results of these simulations can then be used to develop a set of design guidelines for heat exchanger manufacturers.

This research aims to answer the following two questions:

> *"How is heat exchanger performance affected if fin-and-tube heat exchanger coils and coaxial heat exchangers designed for R410A are operated with low-GWP refrigerants?"*

and,

> *"How does heat exchanger designed need to be changed to obtain near-optimum performance for low-GWP refrigerants under current manufacturing constraints?"*

The next sections in this chapter explore in detail the concepts mentioned previously, and concludes by stating how the stated research questions will be addressed in this dissertation document.

1.1 Vapor Compression Systems

Vapor compression systems are widely used in heat pump, AC and chiller applications for providing cooling and/or heating to occupants in residential, as well as commercial spaces. In its simplest configuration, the vapor compressions system consists of a compressor, evaporator, condenser, and an expansion device. Manufacturers of vapor compression systems are inclined to

use numerical simulation models for evaluation of their performance. This model-based design of new equipment has a cost that is substantially lower than developing physical prototypes for every new iteration of the system, or for parametric studies. Simulation models can be reliably validated with limited experimental data. However, it is imperative that models with high-fidelity utilize equally high-fidelity experimental data for their tuning (if any) and validation.

The next sub section explores the various types of heat exchangers, *i.e.*, evaporators, and condensers found in typical vapor compression systems. Emphasis is laid on air-to-refrigerant fin-and-tube heat exchangers, and water-to-refrigerant coaxial heat exchangers, which are the main focus of this research.

1.1.1 Coaxial and fin-and-tube heat exchangers in vapor compression systems

Of the four components in a typical vapor compression system, the condenser and evaporator are the two heat exchangers. Based on the type of load and source side fluids in the system, the heat exchangers can be broadly divided into two types:

- Liquid-to-refrigerant heat exchangers
- Air-to-refrigerant heat exchangers

Liquid-to-refrigerant heat exchangers are of three types:

1. Shell and tube
2. Brazed plate
3. Coaxial

Shell and tube heat exchangers usually consist of a carbon steel shell having end plates and copper tubes. When used as an evaporator, water circulates in the shell side while refrigerant flows in the tubes. When working as condenser, water flows through tubes and refrigerant circulates in the shell. Brazed plate heat exchangers are made up of stainless-steel plates held together by a copper-based brazing metal. Water and refrigerant circulate between alternate plates.

Coaxial heat exchangers, also known as tube-in-tube heat exchanger, consist of an outer plate made of steel or copper, while the inner tube can be titanium, copper or copper-nickel. Water flows in the inner tubes while refrigerant flows between the inner and outer tubes. The inner tubes often have spiral grooves, which help to enhance the heat transfer.

Air-to-refrigerant heat exchangers, for HVAC&R applications, are of two types:
- Micro-channel heat exchangers
- Fin-and-tube heat exchangers

Micro-channel heat exchangers have refrigerant flowing through the tubes while air flows cross-current through the connected fins. Fin-and-tube heat exchangers (FTHXs) consist of tubes with refrigerant flowing through them, with extended outside surface area (fins) to increase heat transfer from surface area of the fins. Figure 1.1 shows a typical FTHX. Compared to micro-channel heat exchangers, fin-and-tube heat exchangers are more widely used because of easy manufacturability and low cost. Since airside heat transfer coefficient is lower than that of the refrigerant flowing inside the tubes, additional heat transfer area is provided by the fins, enhancing the quantity of heat exchange between refrigerant and air.
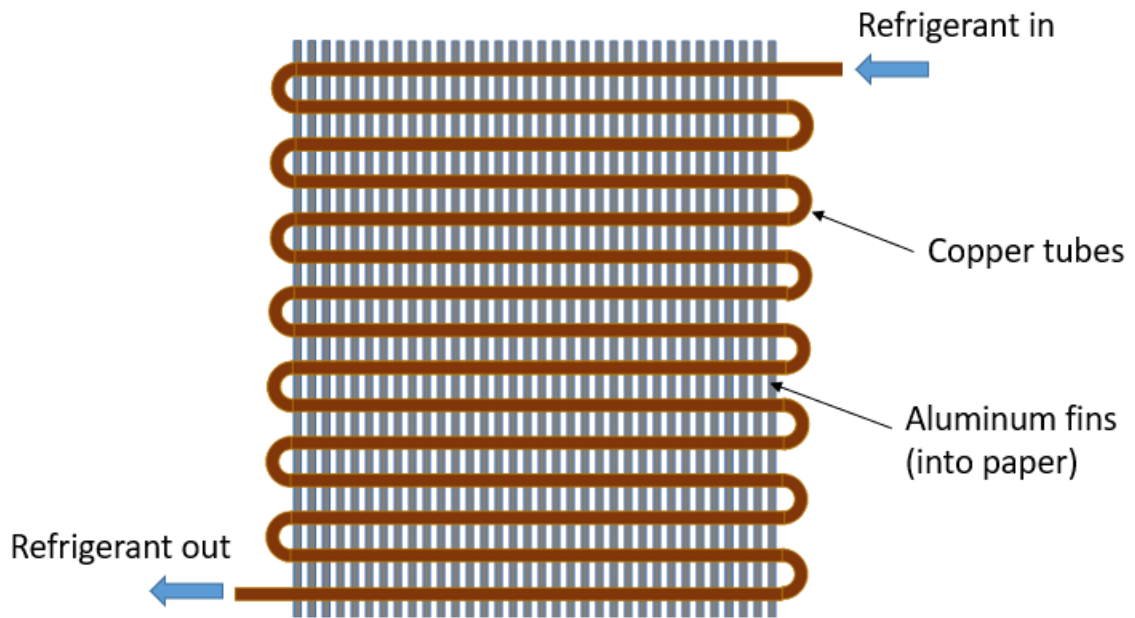
Figure 1.1.Simplified 2-D schematic of a fin-and-tube heat exchanger

1.2 Cross-fin (Xfin) air-to-refrigerant heat exchanger model

Since heat exchangers are a vital part of the vapor compression system, their steady state models have a pronounced effect on the overall accuracy of vapor compression system models. Based on the control volume approach, there are four different approaches to heat exchanger modelling, lumped, moving boundary, tube-by-tube, and segment-by-segment (Sarfraz *et al.,* 2018). The moving boundary approach allows to track the phase change point efficiently in the heat exchanger, and is commonly used for modelling coaxial heat exchangers, allowing accurate prediction of the thermal performance by employing different heat transfer and pressure drop correlations for single-phase and two-phase regions. The segment-by-segment (or discretized) approach requires the most computational effort and resources, but it allows the evaluation of important phenomenon that

influence air-to-refrigerant heat exchanger performance, such as refrigerant and airside 2D maldistribution, and cross-fin conduction.

Cross-fin conduction (or tube-to-tube conduction) is a phenomenon that is prevalent in multi circuit heat exchanger coils operating at part load, *i.e.,* some circuits have refrigerant flow through them while others do not. Since cross-fin conduction can significantly impact coil heat transfer, it needs to be accounted for in heat exchanger modelling. Figure 1.2 illustrates cross-fin conduction occurring inside a FTHX.

Part of this research utilizes a discretized heat exchanger model called cross-fin (Xfin), that has been developed by Sarfraz *et. al.,* (2019a) to evaluate cross-fin conduction (or tube-to-tube conduction) between first-order neighboring tubes in air-to-refrigerant FTHXs. The model allows the user to disable cross-fin conduction during the simulation process, called conduction ignored, so as to determine its influence on the model capacity calculations. The model takes into account refrigerant and air phase transitions, and also detailed input of the simulated heat exchanger`s geometry. It has a low-level segment solver that solves each exchanger segment, and an upper-level solver that can solve the entire heat exchanger by combining the simulation results of each segment in the refrigerant flow direction.
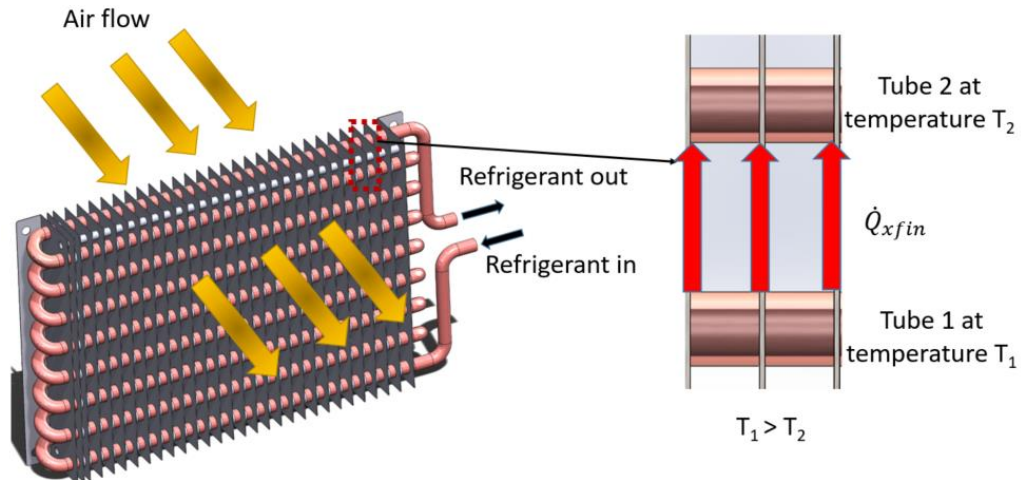
Figure 1.2. Cross-fin conduction in a fin-and-tube heat exchanger

To calculate the heat transfer by cross-fin conduction, the individual segment solver requires the calculation of tube wall temperatures for each segment. Conduction shape factors required to calculate cross-fin conduction are evaluated by a simplified conduction shape factor equation presented by Lee & Domanski (1997).The refrigerant and air side heat transfers in the segment solver are evaluated by applying a lumped analysis using the ε- NTU method.

The upper-level solver connects and solves each individual segment solver in the refrigerant flow direction, in order to solve for the entire heat exchanger. This is accomplished by using heat exchanger circuitry and neighboring tubes information. Circuitry information is incorporated in the Xfin model by adopting the algorithm developed by Jiang *et. al.,* (2006). Further details on the model development, including validation with single-phase experimental data is included in Sarfraz *et. al.,* (2019a).

1.3 Transition to low-GWP refrigerants in building energy use

In the last several years, several types of synthetic refrigerants for vapor compression systems have been introduced and then phased out, due to varying environmental concerns. CFCs (Chlorofluorocarbons), once considered as a long-term solution for cooling systems due their low toxicity and low flammability, were found to destroy the ozone layer. This is because the chlorine atoms in CFCs react with oxygen in the stratosphere, ultimately reducing formation of ozone molecules. Thus, the Montreal Protocol (UNEP, 2016) was enacted in 1987 to phase out CFCs and HCFCs, replacing them with HFCs. Despite having zero Ozone Depletion Potential (ODP) values, HFCs have high GWP) values, making them potent greenhouse gases. Thus, several regulations, such as the Paris Agreement (2015), the Kigali amendment (2016) to the Kyoto Protocol, and the US AIM Act (2021) are forcing the decrease of HFCs in the future. The replacements for HFCs are typically pure HFOs or zeotropic blends of HFOs/HFCs, with low (or near zero) GWP.

The transition to this latest fourth generation of refrigerants poses another challenge to AC and heat pump manufacturers, since their equipment must utilize these new refrigerants, while remaining energy efficient, and cost effective at the same time. A lot of experimental and simulation studies have shown that HFOs and HFO/HFC blends can replace common HFCs such as R134a, R22, R404A, and R410A with minor design modifications (Mota-Babiloni *et al.*, 2016, Heredia-Aricapa *et al.,* 2020, Nair, 2021). Although the literature search shows several system level simulation and experimental drop in studies (see Heredia-Aricapa *et al.,* 2020 and Nair, 2021), it did not reveal a coherent set of guidelines for manufacturers to adapt their existing FTHXs to new fluids.

According to the US Energy Information Administration (EIA), electricity use for space cooling in US residential and commercial sector was about 392 billion kWh, which accounts for 10% of the

total consumption of electricity in USA in 2020 (US EIA, 2020). Additionally, more than $114 billion dollars are spent each year by homeowners and building operators to operate these systems (US EIA, 2016). Hence, these figures, combined with energy efficiency regulations, make it crucial that design guidelines for low-GWP refrigerants for HVAC&R manufacturers are developed in a timely manner. The benefits of this to manufacturers for reducing their overall carbon footprint will be twofold:

- Direct - by utilizing low-GWP refrigerants, by reducing the impact of potential refrigerant leakage, and

- Indirect - having energy efficient equipment that saves emissions from fossil fuel-based power generation systems

1.4 Research objectives

The overall objective of this work is to have an improved understanding of the implication of low-GWP refrigerant onto the performance of existing FTHXs, and coaxial refrigerant-to-water heat exchangers designed for R410A. This will culminate as a set of guidelines for pseudo-optimal design of FTHXs in residential and commercial applications to accommodate the next generation of low-GWP refrigerants, with a goal to obtain improved performance under current manufacturing constraints. This is to ensure a smooth transition of HVAC&R equipment currently utilizing high GWP HFC refrigerants such as R410A, to low-GWP refrigerants which are HFOs, such as R1234yf and R1234ze(E), and HFO/HFC blends, such as R452B and R454B.

The goals of this research are met by a combination of experimental and simulation efforts. An experimental facility is used to test R410A and a low-GWP refrigerant over wide range of operating conditions. This experimental data will be used to validate the Xfin model, which will be then used to simulate several different fluids over a wide range of operating conditions, by varying the heat exchanger geometrical parameters. The following is a brief description of each of the following chapters:

- Chapter 2 details the design and development of a novel pumped refrigerant loop, which is combined with an airside ductwork and an in-house psychrometric chamber, to obtain high fidelity experimental data from multi circuit FTHXs. This chapter has been published as a paper in *International Journal of Refrigeration*,

- Chapter 3 validates the in-house Xfin model by obtaining two phase refrigerant (R410A) data from three multi circuit evaporator coils, having different circuitries and sizes. Model simulations are compared with experiments conducted on the facility described in chapter 2, over a wide range of operating conditions, at full load (all circuits having refrigerant flow through them) and part load (some circuits having refrigerant flow through them). This chapter has also been published as a paper in *International Journal of Refrigeration*,

- Chapter 4 details the development of a moving boundary water-to-refrigerant condenser model, coupled to a 4-component thermodynamic model of a commercial R410A based water-to-water heat pump. The goal of this model was to perform simulations using R454B and R452B as "drop-in" replacements to R410A and identifying performance trends. This chapter has been accepted for publication as a technical paper in *ASHRAE Transactions*,

- Chapter 5 shows how the performance of R1234ze(E) compares for an R410A based fin-and-tube evaporator coil. Experiments are done with both fluids, so that the Xfin heat exchanger model can be validated with R1234ze(E) as well. Simulations are then done with R1234ze(E) with modified heat exchanger circuitry and a range of fin densities, to observe how sensitive is capacity and refrigerant side pressure drop to geometry of the simulated heat exchanger. This chapter has been accepted for publication in the *International Journal of Refrigeration,*

- Chapter 6 shows the simulated comparison of R1234yf and R1234ze(E) for the R410A based fin-and-tube evaporator coil from Chapter 5. Simulations were done with the same air and refrigerant side operational conditions, keeping constant outlet superheat, with the parameters of interest being fin density, number of circuits, tube diameter, and number of tubes in the FTHX. This chapter is also a submitted paper in the *International Journal of Refrigeration,*

- Chapter 7 summarizes the thesis, presents the overall conclusions, and proposes some future work

CHAPTER II

DEVELOPMENT OF NOVEL EXPERIMENTAL INFRASTRUCTURE FOR COLLECTION OF HIGH-FIDELITY EXPERIMENTAL DATA FOR REFRIGERANT TO AIR HEAT EXCHANGERS

ABSTRACT

Fin-and-tube refrigerant-to-air heat exchangers are one of the most common styles of heat exchangers in residential and light-commercial HVAC&R applications. To optimize trade-off between unit efficiency and production costs for units that use them most manufacturers rely on predictive modeling tools. High-fidelity predictive modeling tools require equally high-fidelity experimental data to validate model predictions.

This paper presents the design and development of a custom-designed pumped refrigerant loop that can test fin-and-tube heat exchangers in three modes: (1) single-phase refrigerant, (2) evaporator, and (3) condenser mode. This pumped refrigerant loop will be combined with a small-scale wind tunnel installed in a psychrometric chamber facility to enable acquisition of high-fidelity data to validate recently developed segment-by-segment fin-and-tube heat exchanger numerical models

(Sarfraz *et. al.*, 2019a and 2019b). The pumped refrigerant loop allows precise control of desired test conditions, flowrate to each heat exchanger circuit, and is sized to test heat exchangers up to a capacity of five tons.

A preliminary test plan and detailed uncertainty analysis is developed for the first heat exchanger coil to be tested in the setup. The uncertainty analysis suggests that the experiment will be capable of measuring overall coil capacity within ±2%. A formalized design of experiments is also presented which suggests 9 tests per coil is a sufficient number to minimize experimental effort.

A preliminary experiment was performed in evaporator mode that shows that air and refrigerant side capacities agree within 5%, which is in accordance with the energy balance limit set by ASHRAE Standard 33.

This chapter is published in the International Journal of Refrigeration in 2020 (Saleem *et. al.,* 2020).

2.1 Introduction and Motivation

The vast majority of modern-day air-conditioning, heating, ventilation, and refrigeration (HVAC&R) applications utilize vapor compression systems. In its simplest configuration, a vapor compression system is comprised of a compressor, an expansion device, and two distinct heat exchangers *i.e.*, an evaporator and condenser. For air-to-refrigerant applications, fin-and-tube heat exchangers are widely used because they can be manufactured easily and have low cost. Since the airside heat transfer coefficient is lower than that of the refrigerant flowing inside the tubes, the fins provide additional heat transfer area, hence enhancing the quantity of heat exchange between air and refrigerant.

Modeling of fin-and-tube heat exchanger in a vapor compression system is critical in developing a predictive simulation platform that enables model-based design of new equipment. This is because once developed, numerical models can run at a fraction of the cost of developing prototypes. There are four distinct approaches to modelling of heat exchangers: lumped, moving boundary, tube-by-tube, and segment-by-segment approaches (Sarfraz *et. al.*, 2018). Since numerical heat exchanger models have a pronounced effect on the overall accuracy of vapor compression system models, it is critical that high-fidelity experimental data is obtained to validate the model. A pumped refrigerant loop has been constructed at Oklahoma State University with the purpose of testing fin-and-tube heat exchangers. This pumped refrigerant loop was combined with a small scale-wind tunnel and an existing psychrometric chamber facility to enable the acquisition of high-fidelity data to validate recently developed numerical models (Sarfraz *et. al.*, 2019a and Sarfraz *et. al.*, 2019b) that take into account the physics of cross-fin conduction in fin-and-tube heat exchangers.

2.2 Experimental Testing of Fin-and-Tube Heat Exchangers

Experimental testing of fin-and-tube heat exchangers has been carried out extensively to investigate various parameters concerning the heat exchangers, with a wide variety of test setup configurations and refrigerants. This section explores a variety of experimental investigations of fin-and-tube heat exchangers, outlining their purpose and the important details of their testing environments.

Liang *et. al.*, (2001) developed a segment-by-segment heat exchanger model to investigate the performance of fin-and-tube evaporator coils with complex refrigerant circuitry. The refrigerant conditioning loop was comprised of a vapor compression cycle in which a manual expansion valve (EXV) controlled refrigerant flow rate, and a variable speed compressor was used to set the refrigerant side capacity. A key limitation noted in the refrigerant conditioning loop was the

absence of automatically controlled EXVs for setting the refrigerant mass flow rate entering the test evaporator coils, in order to achieve a desired superheat. Moreover, it was not stated if the presented test rig could be used for testing condenser coils.

Lee *et. al.* (2003) also developed a segment-by-segment heat exchanger model whose experimental validation was performed by conducting several tests using R22 and R407C on two different multi circuit evaporators. The experimental setup comprised of a thoroughly instrumented vapor compression system, along with a pumped cooling water loop to control refrigerant sub-cooling at the inlet to the evaporator distributor. It was evident from the explanation of the refrigerant loop and it's schematic that it could be used only for testing evaporator coils. Moreover, the loop had incorporated capillary tubes instead of EXVs, downstream of the distributor, to ensure uniform distribution of refrigerant to each circuit. This meant that the test loop lacked any capability to assign varying refrigerant flow to each individual circuit.

Song *et. al.* (2012) evaluated numerically and experimentally evaluated the performance of multi-circuit fin-and-tube evaporator coils in residential AC units. They found that the performance was affected by non-uniform air velocity distribution at the coil face. The test rig comprised of a split type residential AC, whose indoor and outdoor heat exchanger coils were installed in indoor and outdoor psychrometric chambers, respectively. The outdoor section comprised of a rotary compressor, reversing valve, outdoor coil, main and auxiliary capillaries and an accumulator. The indoor section included the indoor coil. The auxiliary and main capillaries were used as the main expansion device for the heat pump. Additionally, there were no valves downstream of the distributors of the indoor coils, implying that it was not possible to independently control the refrigerant mass flow rate entering each of the evaporator circuits or to control refrigerant enthalpy

entering the evaporator.

Domanski *et. al.* (2007) experimentally assessed how tube-to-tube heat transfer occurring by conduction through fins affected the performance of finned-tube evaporators at varying refrigerant exit superheats. The experimental setup comprised of a vapor compression loop as the test rig, a chilled water loop and an air flow loop. The vapor compression loop comprised of a variable speed compressor, water cooled shell-and-tube condenser, sub cooler and three EXVs. The compressor was used to set the overall refrigerant flow rate while condensing pressure and evaporator inlet enthalpy (sub cooling at inlet of EXVs) were set by the water flow rate and temperature entering the sub cooler. A pressure regulating valve downstream of the evaporator coil was used to control evaporator exit pressure, while the three EXVs were used for controlling exit superheat of each circuit by altering the refrigerant flow rate entering each evaporator circuit. When compared to the previously mentioned experimental setups, this facility provided an additional control of controlling refrigerant flow rate to each independent circuit. However, it could not be used for testing condenser coils.

Wang *et al.* (2016) did experimental testing and numerical modelling to evaluate how refrigerant side maldistribution is affected by inlet tube length of distributor, inclination angle, non-uniform airflow, and feeder tube length on a multi-circuit evaporator. The test setup, using R410A as the refrigerant, comprised of a vapor compression loop with some additional components including an extra compressor and sub-condenser cooling loop, for testing cooling coils ranging from a capacity of 3 to 40 kW. It was observed that the test setup was built around the concept of strictly testing evaporators.

Castro *et. al.* (2005) performed experimental testing and numerical modelling of a reversible air-

to-water heat pump, using R290 as refrigerant, to find the best fin-and-tube heat exchanger coil configuration. The heat pump comprised of a fin and tube heat exchanger, scroll compressor, brazed plate heat exchanger (BPHE) and a TXV. The water-side of the heat pump unit was comprised of a pumped hydraulic loop that interfaced with the heat pump by the BPHE. The heat pump was installed in a psychrometric chamber for testing purposes and was operated in heating as well as cooling mode. Two different evaporators were tested, having different number of circuits and circuit lengths. Even though both the test heat exchanger coils were multi circuit, the facility lacked any provision for part load testing of the coils by controlling the individual refrigerant flow to each circuit

Several fin-and-tube heat exchanger analysis have been done by using only single-phase refrigerant as the working fluid. Ma *et. al.* (2007) experimentally investigated the airside heat transfer and pressure drop characteristics of 14 enhanced fin-and-tube heat exchangers with hydrophilic coating under wet coil conditions. The conditioning loop in the experimental setup comprised of a pumped water loop. The inlet temperature of water to the test section was adjusted by means of a thermostat. From the explanation of the conditioning loop, it was evident that it could only be used to test evaporator coils. Furthermore, there was no mention of a Variable Frequency Drive (VFD) attached to the water pump, implying that it was running at a fixed speed. This was further confirmed by the test conditions of the experiment, where the only parameter that were varied on the refrigerant (water) side was the flow rate and inlet temperature to the test coil.

Kim (2016) also used water as the working fluid to investigate how heat transfer and pressure drop characteristics of radial slit-finned heat exchangers were affected under wet operating conditions. The test section was located inside a psychrometric chamber. Water flow rate and temperature

17

could be adjusted by a constant temperature water bath. However, the inlet water temperature and mass flow rate were both held constant during the experiments , and similar to Ma *et. al.,* (2007) , there was no VFD used for controlling pump speed.

Similarly, Blecich (2015) evaluated how non-uniform airflow effected the performance of a multi-circuit fin-and-tube heat exchanger. The heat exchanger being tested was served by a closed pumped water loop on the load side, and was placed inside a wind tunnel. To achieve non-uniform airflow, part of the heat exchanger entrance cross section was blocked. Even though the tested heat exchanger had multiple circuits, the test setup lacked any provision for providing varying refrigerant (water) flow rate to each individual circuit. Having precise control of refrigerant flow rate for every individual circuit could lead to the mitigation of refrigerant side maldistribution (by ensuring uniform refrigerant exit temperature from each circuit), thus giving more accurate experimental data to study the effect of non-uniform airflow. Several examples of the COP and capacity benefits of precise control of individual circuit flowrates for AC, heat pump, and refrigeration systems` evaporators are shown in Bach (2014).

Even though there has been extensive research conducted on investigating fin-and-tube heat exchanger performance, the literature search revealed very limited experimental setup configurations that tested both, evaporator (cooling) as well as condenser (heating) coils. Finally, no experimental facility was found that could do the above while also providing the flexibility to test single-phase refrigerant.

This paper presents the design and development of a custom-designed pumped refrigerant loop coupled with a small-scale wind tunnel and an existing psychrometric chamber facility that will achieve all aforementioned features. This will enable the acquisition of high-fidelity data to validate

a numerical model developed by Sarfraz *et al.* (2019a) that is being developed for evaluating the performance of fin-and-tube heat exchangers. The pumped refrigerant loop allows precise maintenance of the desired test conditions and flowrate of refrigerant and has been sized to test heat exchanger coils up to a capacity of five tons in cooling and heating mode. In addition, the pumped refrigerant loop has the ability to test both, evaporator as well as condenser coils, simply by using a combination of different valves in open and closed positions.

2.3 Heat Exchanger Testing Facility

The experimental apparatus for evaluating the performance of fin-and-tube heat exchanger test coils combines an airside ductwork with an ASHRAE code tester installed in a psychrometric chamber facility with a pumped refrigerant loop as shown in Figure 2.1. The main focus of this article is the refrigerant loop. Details of the psychrometric chamber facility can be found in Lifferth (2009) and Aslan (2010), while the airside ductwork is explained in Lee *et. al.*, (2018 and 2019).

2.3.1 Pumped refrigerant loop design and operation

Tests will be conducted in a wind tunnel that allows the flow of conditioned air through the test heat exchanger coils. A schematic of the wind tunnel is shown in Figure 2.1, and a photograph is shown in Appendix A. The wind tunnel has been designed for the first test coil, having a length of 44.5 cm (17.5 inches) and height of 40.64 cm (16 inches). To achieve uniform air flow in the wind tunnel, ASHRAE Standard 33 was used as the guideline for minimum velocity and temperature uniformity at the test section. Experiments were performed by Lee *et. al.*, (2019) in accordance with ASHRAE 33, and it was found that the measured highest and lowest air face velocities were

19

within 20% and the entering dry-bulb temperatures were within 0.56 K (1 R) at the face of the test coil.

Test heat
exchanger coil

Air flow from
psychrometric
chamber loop

Air flow to
code tester

Inlet air
sample tree (T_{db}, T_{wb})

Outlet air
sample tree (T_{db}, T_{wb})

T Temperature measurement
wb Air wet bulb
db Air dry bulb

Pumped
refrigerant loop
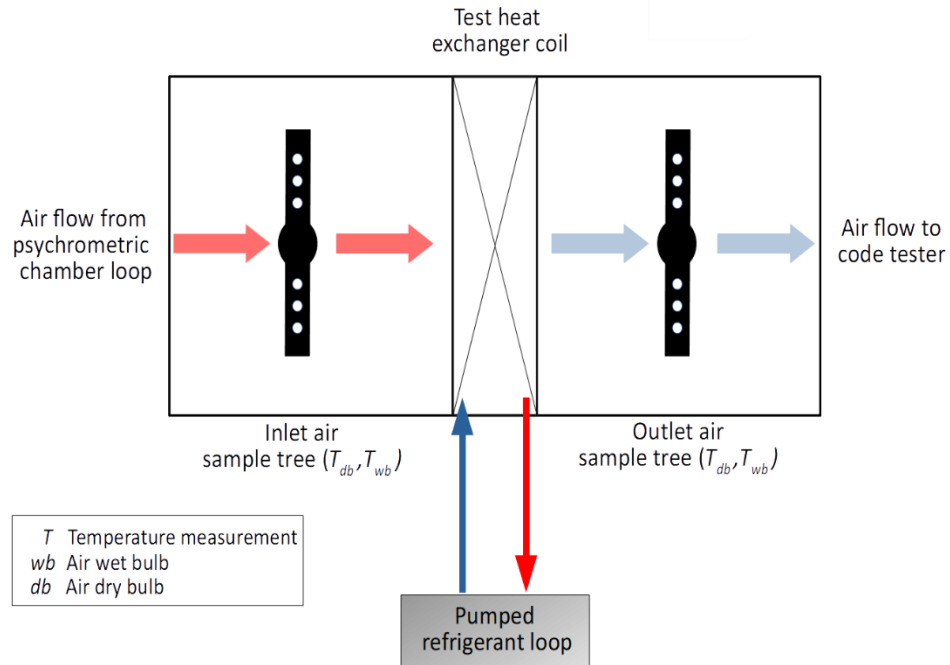
Figure 2.1. Schematic diagram of wind tunnel

The wind tunnel is housed in the outdoor room of a psychrometric chamber facility, whose temperature and humidity control ranges are well suited for the desired test conditions of this study (Cremaschi & Lee, 2008). The outdoor room`s flow measurement bay (code tester) generates the required air flow for coil testing as well as measures the air flow rate. Air circulation in the chamber can be seen in Figure 2.2 where the coils tested for this study will be installed in the "setup" section upstream of the code tester.

Air flowing over the test coils passes onto the flow measurement bay after which the flow splits into two and goes to two conditioning bays. Each conditioning bay is equipped with a set of heaters,

cooling coils and humidifier, to generate the required inlet air conditions (dry bulb and wet bulb temperature) to the test coils. The conditioned air flow is then directed to the room through the chamber`s perforated floor. Part of the conditioned air re-enters the wind tunnel shown in Figure 2.2, while the remainder rises up to the ceiling and goes back to the conditioning bays via the ceiling plenum. Air going through the ceiling mixes up with the air going through the flow measurement bay, and the air circulation process explained above repeats until testing is complete.
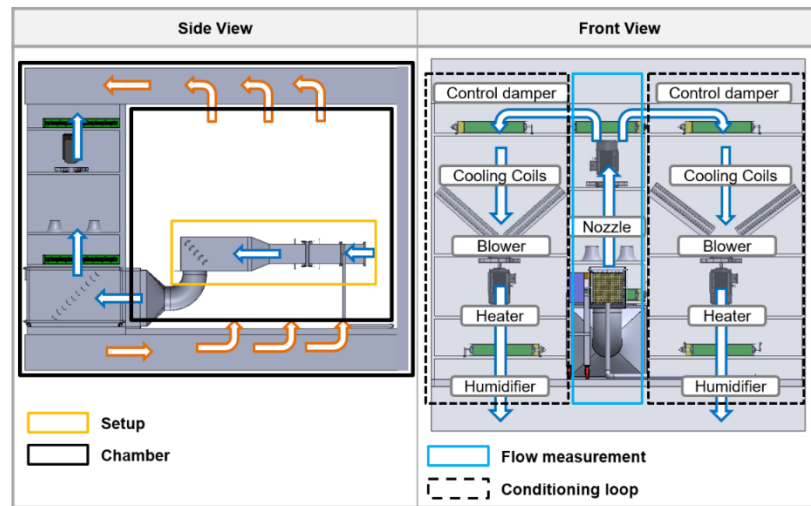
Figure 2.2. Air circulation within the psychrometric chamber (Lee *et al.,* 2018)

The pumped refrigerant loop has been designed to operate with R410A and sized to test heat exchanger coils up to a capacity of 5 tons (17.5 kW). The overall testing environment has been designed to provide control of the following operating parameters:

- Refrigerant mass flow rate, $\dot{m}_r$, in the loop,

- Saturated suction temperature (SST) of refrigerant at inlet to the heat exchanger, and

- Test superheat (SH) of refrigerant at outlet of the heat exchanger for evaporator testing and test subcooling (SC) for condenser testing,

21

Figure 2.3 (a) and (b) show the operation of the pumped refrigerant loop operating in evaporator and condenser mode respectively. A 3D CAD model of the refrigerant loop and trim heating loop is shown in Figure 2.4, and a photograph is shown in Appendix A. For heat exchanger coil testing in evaporator mode, refrigerant is evaporated in the test coil from points 1 to 2 and enters the heat rejection units at point 3, which are modified water-to-water heat pumps, each having a cooling capacity of 10.6 kW (3 tons), *i.e.*, combined cooling capacity of 21.1 kW (6 tons), where refrigerant vapor is condensed. After exiting the 2nd heat rejection unit at point 5, the subcooled refrigerant passes through the refrigerant pump to point 6. The refrigerant exiting the gear pump now passes through a filter drier, which ensures that the refrigerant is free of contaminants and moisture. It is then pumped through a water-to-refrigerant BPHE (points 7 to 8) to set the refrigerant at the desired temperature. Finally, the refrigerant is now at the desired state and enters the test heat exchanger at point 1 via the EXVs, which are able to expand the refrigerant down to the desired inlet two-phase quality. The entire refrigerant circulation process mentioned above is repeated during the operation of the refrigerant conditioning loop. The pumped refrigerant loop has additional features including, a sight glass installed at the suction to the gear pump to monitor flow conditions. It also includes a bladder accumulator in which the refrigerant (bottom) is separated from nitrogen (top) by a membrane. The accumulator is charged with nitrogen gas in accordance with the required refrigerant mass in the setup. It is used to set refrigerant pressure during single-phase refrigerant tests.
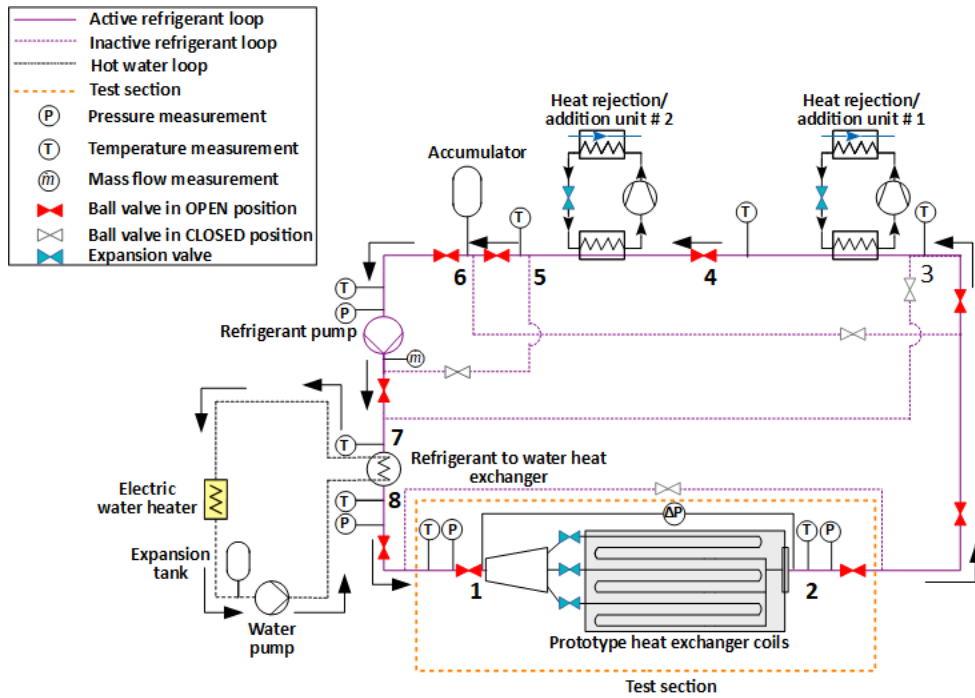
a) Operation of refrigerant loop in evaporator mode (Refrigerant flow path:1→2→3→4→5→6→7→8→1)
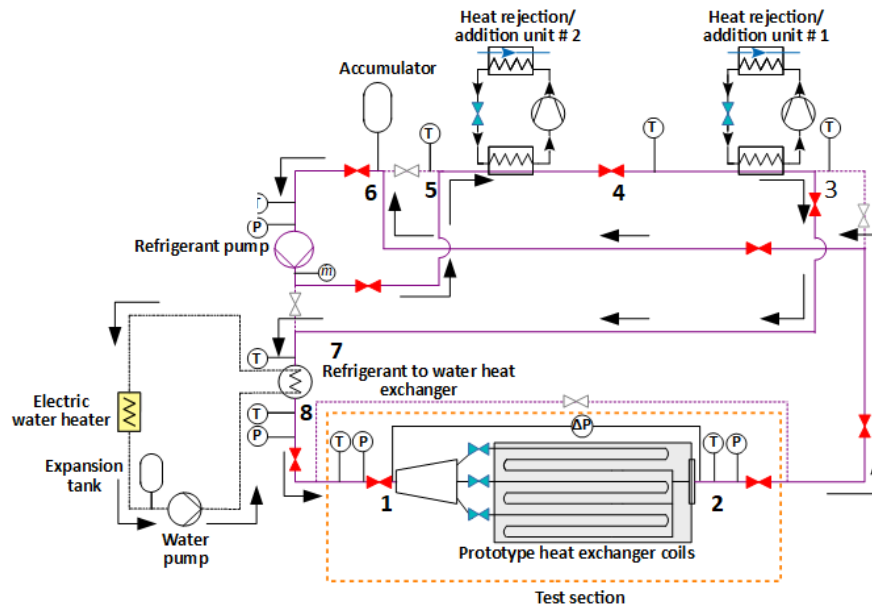
b) Operation of refrigerant loop in condenser mode (Refrigerant flow path: 1→2→6→5→4→3→7→8→1)

Figure 2.3. Schematic diagram of pumped refrigerant loop and trim heating loop
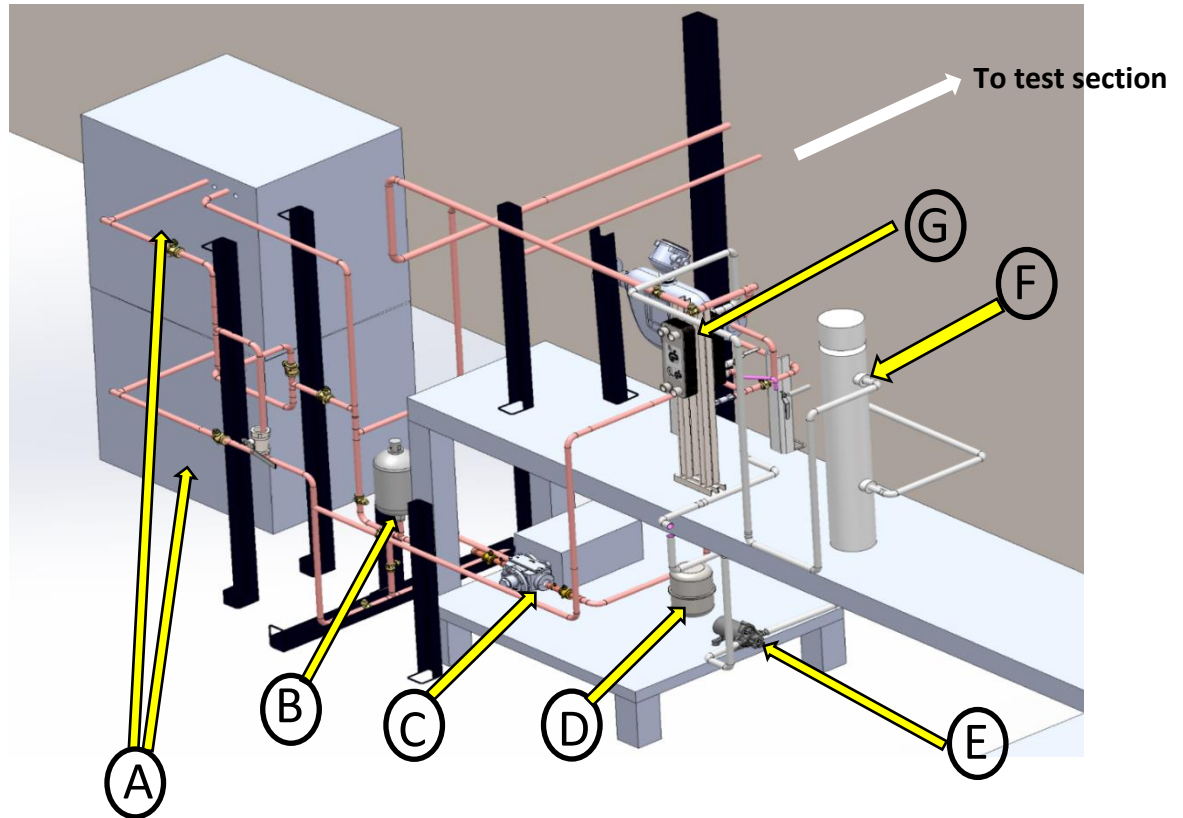
Figure 2.4. Isometric view of pumped refrigerant loop design (excluding the test section) with major components labelled. (A) heat rejection units; (B) accumulator; (C) refrigerant pump; (D) expansion tank; (E) water pump; (F) electric water heater; (G) refrigerant-to-water heat exchanger. Both heat rejection units are stacked on top of one another to save space, while the refrigerant pump is located below majority of the equipment, allowing easy displacement of refrigerant throughout the loop.

2.3.2 Pumped refrigerant loop controls scheme

LabVIEW was used to implement a control scheme of the pumped refrigerant loop and data collection from the instrumentation attached to it. The refrigerant mass flow rate is controlled by adjusting the frequency output of the variable frequency drive attached to the refrigerant pump. The refrigerant SST is controlled via adjustment of the input power to the water heater by means of a Silicon-Controlled Rectifier (SCR). By adjusting the input power, the temperature of the hot water leaving the heater changes, thus changing the water-to-refrigerant heat transfer in the BPHE shown

in Figure 2.3 (points 7 to 8), ultimately altering the refrigerant SST. Additionally, a series of EXV's are installed at the inlet to the tested coil (state 1) which are adjusted automatically to control superheat at heat exchanger exit when operated in evaporator mode, and the sub cooling when operated in condenser mode. Figure 2.5 shows a flow chart of the controls scheme when the refrigerant loop is used for testing in evaporator mode.
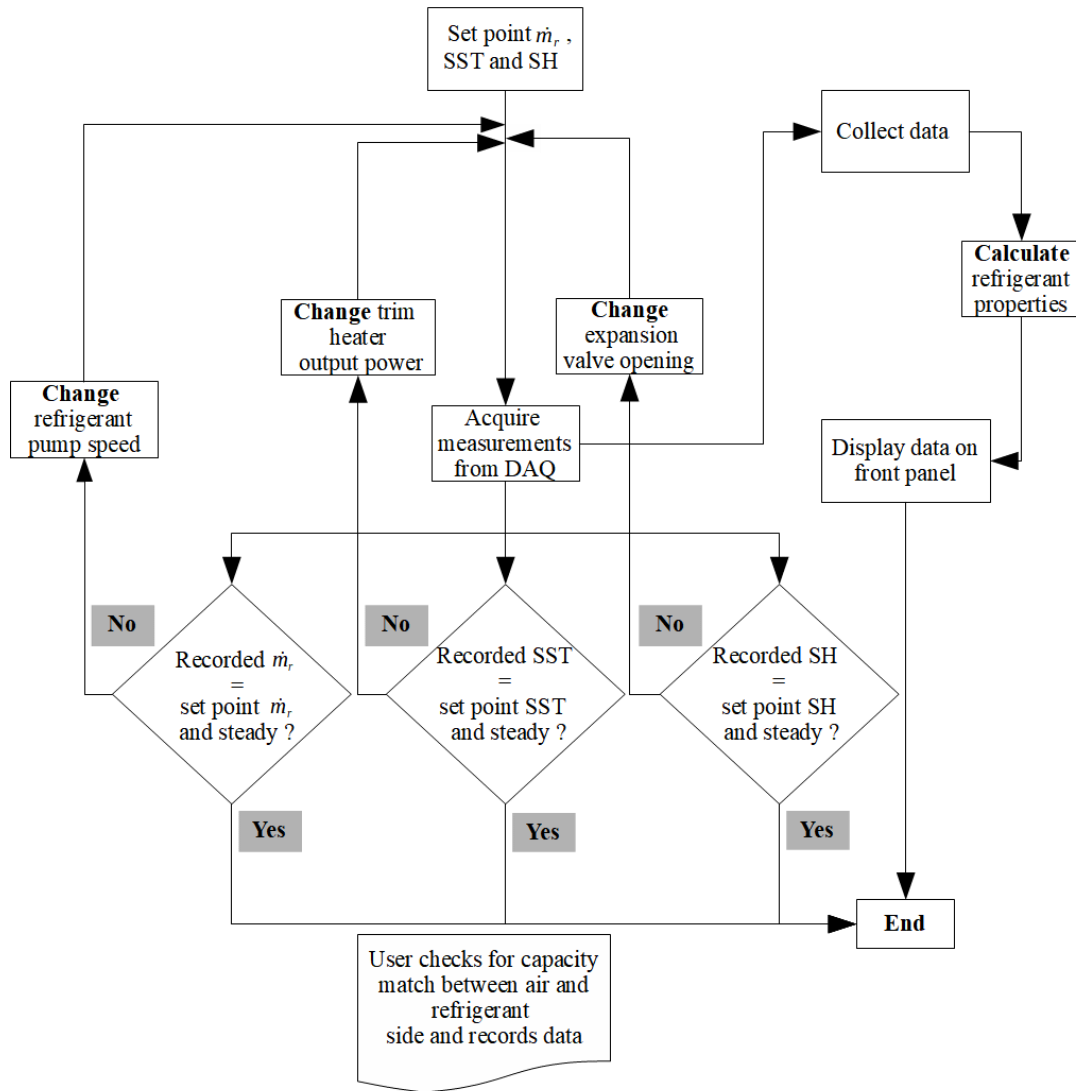
Figure 2.5. Flowchart of data acquisition and controls of pumped refrigerant loop running in evaporator mode

2.3.3 Pipe diameter selection

Using the state of refrigerant at each state, tables specific to R410A from the 2010 ASHRAE Handbook: Refrigeration (2010) were used to size the copper tubing for a capacity of 5 tons (17.6 kW) , depending if the piping section was considered as a vapor line at suction pressure, a vapor line at discharge pressure or liquid line. The copper tubing extending from points 2-5 will have superheated vapor when performing two-phase evaporator testing, and hence has been sized as a vapor line at suction pressure with an outer diameter (OD) of 7/8" (22.2 mm). Similarly, the tubing from points 5-7 has been sized as a liquid line with an OD of 1/2" (12.7 mm), because it will always contain liquid refrigerant, regardless of the mode of testing. Finally, the tubing from points 8-1 will have refrigerant vapor during condenser testing, and hence has been sized as a vapor line at discharge pressure with an OD of 5/8" (15.9 mm).

2.3.4 Safety Circuit Design

A safety circuit has been designed that ensures a complete shutdown of all equipment in case of any equipment malfunction or emergency. It is equipped with an emergency stop button to allow the user for performing a manual shut down. A pressure relief valve connected to the discharge line of the refrigerant pump prevents any damage to the equipment in the event that refrigerant pressure exceeds the overall system`s rated pressure of 41.4 bar (600 psig). A low-pressure cutout is set at 8.62 bar (125 psig) at suction of the refrigerant pump ensures that the system will not run, in case if refrigerant has leaked out of the system. A high temperature cutout, set at 90°C (194°F) is attached on the discharge side of the water heater to protect the water pipes from overheating if the water boils, while a low temperature cutout, set at 5°C (41°F), attached to the refrigerant-to-water

exchanger prevents it from being damaged from water freezing. A pressure relief valve is connected at the outlet of the water heater that prevents damage to the water loop if the water pressure exceeds 10.3 bar (150 psig). At the suction of the hot water circulator, a low flow switch is installed and integrated into a separate independent safety circuit, ensuring that the water heater will not turn on in case there is insufficient water circulation in the hot water loop.

2.4 Preliminary test plan

A preliminary test plan is formulated for the first coil that will be tested in the refrigerant conditioning loop. This coil has 4 circuits with 12 tubes in each circuit and 48 tubes in total as shown in Figure 2.6 which presents a photograph and circuiting schematic of this coil. The coil has sine-wave fins. The objective of this test plan is to minimize the number of data points required to explore each test variable, called design factors, in order to test the highest number of unique test variables. To accomplish this, a formalized method called full factorial design is used.

The preliminary test plan is based on the full factorial design of experiments with the control run (center point), presented by Myers & Montgomery (1995) where the full number of required experiments is estimated by $2^n + 1$, where n is the number of design factors. The control run (or center point) of the design space where all factors have an average value between their low and high level is included to:

- Provide a measure of process stability and inherent variability, and
- Check for the curvature of the response surface *i.e.* whether relationship between the outcome and input variables is linear or non-linear (curvature).

a) Photograph of test coil (not to scale)   b) Circuit schematic of test coil
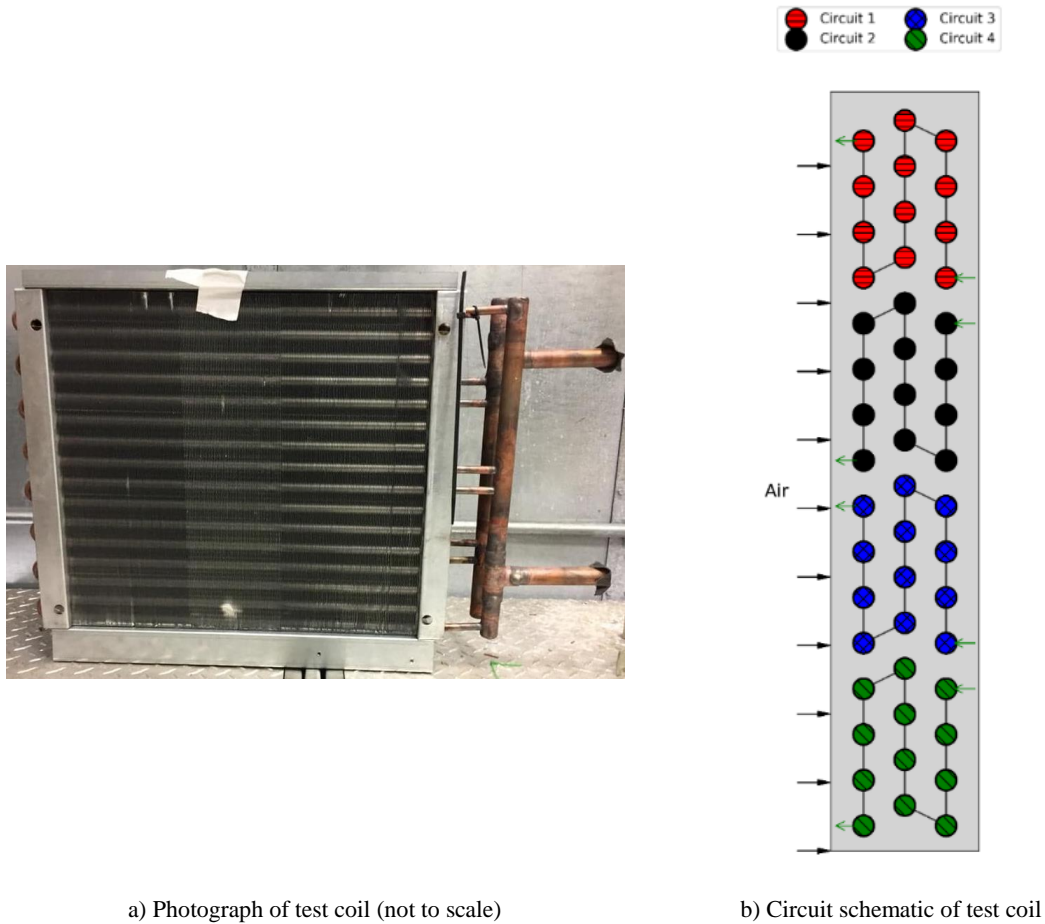
Figure 2.6. Tested coil with a cooling capacity of approximately 1.5 tons

In this experiment, the heat exchanger coil capacity is the critical outcome and the design factors are selected based on the authors' and collaborators experience with the heat exchanger testing and resulted in the following three factors: (1) SST of refrigerant, (2) SH of refrigerant, and (3) air velocity at coil face ($v_{a,i}$). The range of the design factors selected for testing the first coil in evaporator mode are listed in Table 2.1.

Table 2.1. Range of design factors

Factors	Minimum value ($-$)	Maximum value ($+$)
Saturated suction temperature (SST)	7.22°C (45°F)	12.78°C (55°F)
Air inlet velocity ($v_{a,i}$)	1 m/s (200 fpm)	2 m/s (400 fpm)
Test superheat (SH)	5.56°C (10°F)	12.22°C (22°F)

The design space containing the points for full factorial design are shown in Figure 2.7.
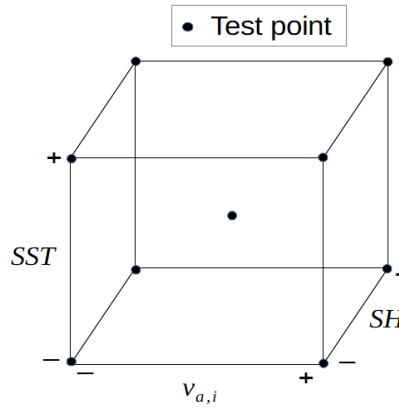
Figure 2.7. Design space showing design points

Both the refrigerant enthalpy at the coil inlet and the air inlet dry and wet bulb temperatures will be fixed during the exploration of the design space. These 9 test points in the design space will be repeated for a variety of different inlet air conditions and coil models of operation including wet and dry evaporator tests and condenser tests. The air dry and wet bulb and dew point temperatures to test the coil in evaporator and condenser modes are given in Table 2.2. The air dew point is selected such that it is above the SST of the refrigerant for the wet evaporator test and below the SST for the dry evaporator test.

Table 2.2. Air temperatures for tests in evaporator and condenser mode

Mode	Dry bulb temperature	Wet bulb temperature	Dew point temperature
Evaporator dry	26.67°C (80°F)	14.44°C (58°F)	4.44°C (40°F)
Evaporator wet	26.67°C (80°F)	19.44°C (67 °F)	15.56°C (60°F)
Condenser	26.67°C (95°F)	23.89°C (75°F)	19.17°C (66.5°F)

Table 2.3 lists the test conditions for the wet evaporator test.

Table 2.3. Conditions for the wet evaporator test

Air dry bulb temperature	Air wet bulb temperature	Liquid line temperature	SST	$v_{a,i}$	SH
26.67°C (80°F)	14.44°C (58°F)	35°C (95°F)	7.22°C (45°F)	1 m/s (200 fpm)	5.56°C (10°F)
			12.78°C (55°F)		
			7.22°C (45°F)	2 m/s (400 fpm)	
			12.78°C (55°F)		
			7.22°C (45°F)	1 m/s (200 fpm)	12.22°C (22°F)
			12.78°C (55°F)		
			7.22°C (45°F)	2 m/s (400 fpm)	
			12.78°C (55°F)		
			10°C (50°F)	1.5 m/s (400 fpm)	8.89°C (16°F)

The critical (or sensitive) design points will be located and isolated after the execution of the initial

test matrix. The critical design points are the points that produces a considerable change in the coil

capacity. These critical design points will be used as a litmus test to determine which of the parameters are most critical and encourage additional testing between those points to add additional test fidelity. Figure 2.8 shows an example of 2 critical design points out of 9 design points obtained after the execution of initial test matrix.
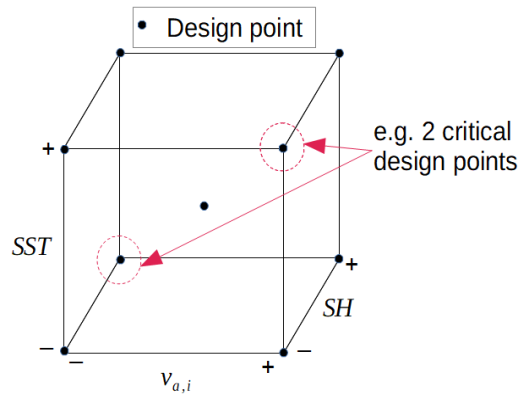
Figure 2.8. Example of critical design points

Once the critical design points will be located, further design points in the vicinity of the critical design points will be explored as shown in Figure 2.9.
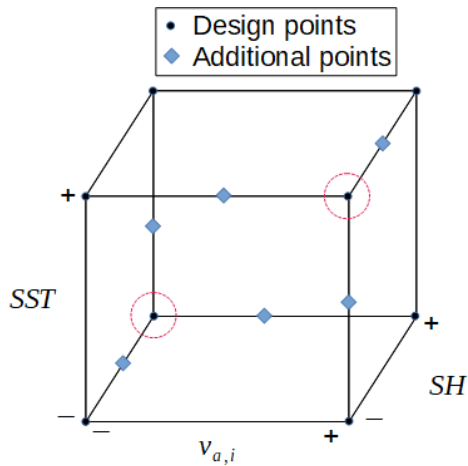
Figure 2.9. Exploration of points in the vicinity of the critical design points

31

2.5 Uncertainty analysis

An uncertainty analysis is performed for the air and refrigerant side based on the standard uncertainty of the selected instrumentation.

2.5.1 Airside uncertainty

The overall airside capacity, $\dot{Q}_{air}$ is given by equation 2.1 as

$$\dot{Q}_{air} = \dot{m}_{air} \cdot \left(h_{a,bht} - h_{a,aht}\right), \tag{2.1}$$

where $\dot{m}_{air}$ is the air mass flow rate, $h_{a,bht}$ and $h_{a,aht}$ are the air enthalpies before and after the coil, respectively. The uncertainty of each term will be individually explored in the following section starting with the air mass flow rate.

The air volumetric flow rate is calculated using a nozzle box containing different set of nozzles to cover a wide range of flow rates. This nozzle box has been utilized for several previous experimental studies (Cremaschi & Perez, 2017, Yatim *et. al,.* 2017).To calculate the air mass flow rate, measurements of differential pressure across the nozzle set, the air temperature and pressure at the nozzle inlet, and the nozzle diameter are required as inputs to the equations given in ASHRAE Standard 37 (2009). The type, measurement range, and the accuracy of instruments used to measure these parameters in this facility are listed in Table 2.4.

The uncertainty propagation in flow rate due to the uncertainties of the parameters in Table 2.4 is calculated using ASME PTC 19.1 (2013). It states that for the result R and its parameters

$(X_1, X_2, \ldots, X_i, \ldots, X_N)$, the sensitivity coefficient θ_i for parameter X_i can be found using partial differentials as: $\theta_i = \frac{\partial R}{\partial X_i}$, where partial derivative can be evaluated analytically or numerically using finite difference approach. The uncertainty in the result, δR if the uncertainty in the parameters $(X_1, X_2, \ldots, X_N)$ are $\delta X_1, \delta X_2, \ldots, \delta X_N$ can be found using equation 2.2.

$$\delta R = \sqrt{(\theta_1 \cdot \delta X_1)^2 + (\theta_2 \cdot \delta X_2)^2 + \cdots + (\theta_N \cdot \delta X_N)^2} \tag{2.2}$$

Table 2.4. Information on instrumentation for parameters needed for airflow calculation

Parameter	Instrument		
	Type	Range	Accuracy
Differential pressure across nozzle	Differential pressure transducer	0-747 Pa	±0.25% full scale
Nozzle diameter (ND)	NA	0-6 in	0.002·ND*
Temperature (dry and wet bulb) at nozzle inlet	RTD	5-75°C	±0.06°C**
Pressure at nozzle inlet	Pressure transducer	-374-374 Pa	±0.25% full scale

Conforms to accuracy limit set by ASHRAE Standard 51-16
**calibrated to a reference thermometer with ±0.06°C rated accuracy
NA → Not applicable, RTD → Resistance temperature detector

The velocity at the coil inlet will be controlled to vary from 1 to 2 m/s (200 to 400 fpm) as described in the test plan section. The first coil to be tested in this environment has a face area of 0.18 m² (1.94 ft²). This results in an airflow rate of 0.19 to 0.38 m³/s (400 to 800 cfm) for the first test coil.

Figure 2.10 shows the uncertainty propagation results of airflow rate due to the uncertainties of its parameters. The maximum relative uncertainty in the airflow rate is within 0.7% of the measured value across the predicted operating envelope. At the lowest air flowrate where the relative

uncertainty in the air flowrate is highest, the differential pressure measurement across the nozzle

(ΔP) is the main contributor to this uncertainty, accounting for more than 80%. This is followed by

the uncertainty in the nozzle diameter measurement that accounts for more than 18% of the

uncertainty in the air flow rate. The contribution of the other parameters *i.e.,* air side dry bulb

temperature, $T_{a,db}$ and wet bulb temperature, $T_{a,wb}$ and pressure at nozzle inlet (P_a) to the air

volumetric flow uncertainty is below 0.01%.

With an increase in the air flowrate due to an increase in the air differential pressure across nozzle,

the contribution of the differential pressure measurement to the overall air volumetric flowrate

uncertainty decreases due to the decrease in its relative uncertainty.
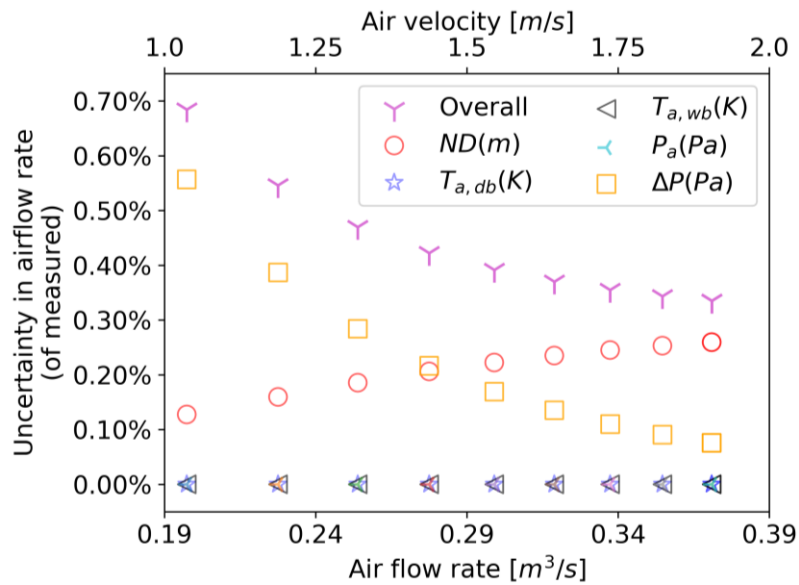
Figure 2.10. Effect of air flowrate on uncertainty contributors (using 4 in (0.1016 m) and 3 in (0.0762 m) diameter nozzles)

The outlet and inlet air enthalpies are also required for air capacity calculation and are calculated

by measuring air dry and wet bulb temperatures. There are two RTDs at the coil inlet and two RTDs

at the coil exit with the each calibrated to a reference thermometer with ±0.06 °C rated accuracy and measurement range of 5-75 °C. The wet bulb temperature is the main contributor to the uncertainty in enthalpy with the contribution of greater than 99% with dry bulb temperature contributing less than 1%, although both the wet and dry bulb RTDs' have similar uncertainties as stated above.

The individual uncertainties calculated previously can then be incorporated into a total propagated uncertainty of the coil capacity. To accomplish this, the nominal capacity of the initial test coil is used (5.5 kW) to first estimate the outlet air conditions from the coil for a given set of inlet conditions for the wet evaporator test (see Table 2.3) at an air flow rate of air flow rate of $0.38 \text{m}^3/\text{s}$ (800 cfm) (*i.e.* maximum flow rate). The air outlet conditions are then fixed and the airflow rate is varied from 800 cfm ($0.38 \text{ m}^3/\text{s}$) to 400 cfm ($0.19 \text{ m}^3/\text{s}$) to obtain the airside capacity as a function of airflow rate.

Figure 2.11 shows the result of this uncertainty propagation analysis in the airside capacity due to the uncertainty in its various parameters. The air wet bulb temperature is the main contributor to the overall uncertainty in airside heat transfer with the percentage contribution of more than 80%. The contributions of the differential pressure measurement and nozzle diameter are greater than 13% and 3% respectively. The contribution of the remaining parameters *i.e.,* air dry bulb temperature and pressure to the overall uncertainty in the heat transfer is negligible *i.e., <*1%.
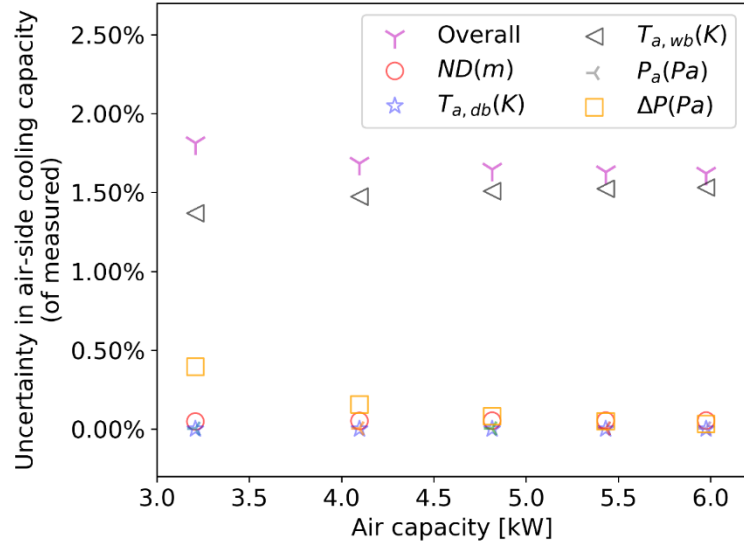
Figure 2.11. Effect of air-side cooling capacity on uncertainty contributors

2.5.2 Refrigerant side uncertainty

The refrigerant capacity, $\dot{Q}_{ref}$ is given by equation 2.3.

$$\dot{Q}_{ref} = \dot{m}_r \cdot \left(h_{r,out} - h_{r,in}\right), \tag{2.3}$$

where $\dot{m}_r$ is the refrigerant mass flow rate, $h_{r,in}$ and $h_{r,out}$ are the refrigerant enthalpies at the inlet and outlet of the coil, respectively.

The refrigerant enthalpy is calculated by measuring its temperature and pressure. The type, measurement range, and accuracy of instruments used to measure the parameters for refrigerant capacity calculation are provided in Table 2.5.

36

Table 2.5. Instrumentation information for refrigerant capacity calculation

Parameter	Instrument		
	Type	Range	Accuracy
Refrigerant mass flow rate	Mass flow meter	0-1 Kg/s	±0.05% of measured
Refrigerant temperature before and after coil	RTD	5-90°C	±0.06°C*
Refrigerant pressure before and after coil	Pressure transducer	0-500 psi	±0.42 psi

calibrated to a reference thermometer with ±0.06°C rated accuracy
*** in-house calibrated, manufacturer rated accuracy is* 0.13% full scale

Figure 2.12 shows the uncertainty propagation in the refrigerant capacity due to the individual uncertainty in its parameters. The overall relative uncertainty in the refrigerant capacity is within 0.2% of the measured value with refrigerant pressure contributing more than 44% to the overall uncertainty. The refrigerant temperatures (before and after the coil) and the mass flow rate contribute 36.44% and 19.33% to the overall uncertainty.
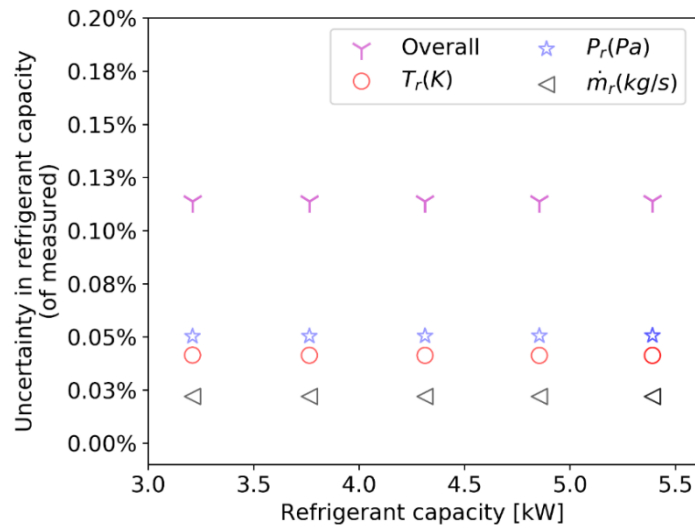
Figure 2.12. Relative uncertainty in refrigerant capacity due to different parameters

2.6 Preliminary Testing - Energy balance between air and refrigerant capacities

According to ASHRAE Standard 33, the capacities on the air and refrigerant side shall agree within 5% as the average of these capacities is the capacity of the coil. The overall uncertainty on the air and refrigerant side, therefore, must be a percentage of measured such that the maximum difference between the uncertainties is within 5% capacity limit mentioned in ASHRAE Standard 33. The instrumentation on the air and refrigerant side are selected with the standard uncertainties so that the maximum difference between the air and refrigerant side uncertainties is within 2% of the measured within the operating range given in the test setup.

To verify that the experimental facility is capable of conforming to ASHRAE 33 capacity tolerance limits, a preliminary test was run, using single-phase refrigerant in evaporator (dry) mode. For the given test, the set points for SST and $\dot{m}_r$ were 10°C (50°F) and 0.022 kg/s (174.6 lbs. per hour) respectively. On air side, the set points for the $v_{a,i}$ and $T_{a,db}$ were and 26.67°C (80°F) respectively.

Data collection was initiated at a rate of 1 sample per second once air and refrigerant side reached steady state and the capacities were within 5% of each other. Data was recorded for a total of 3 minutes. Figure 2.13 shows the comparison of air and refrigerant side capacities for the preliminary test.
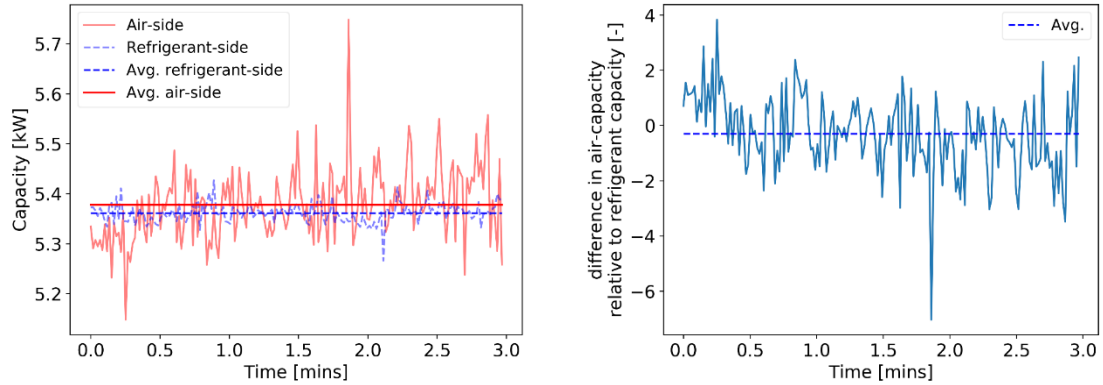
Figure 2.13. Plots of air and refrigerant side capacities over a 3-minute period

The refrigerant side capacity has a lower random uncertainty in comparison to the airside. Moreover, for majority of the testing duration, air and refrigerant side capacities were within 5% of each other as required by ASHRAE 33.

2.7 Conclusions

The paper presents the design and development of a custom designed pumped refrigerant loop to collect high-fidelity data for validating a segment-by-segment fin-and-tube heat exchanger model. A literature survey found that the designed pumped refrigerant loop is unique because it can test cooling (evaporator) as well as heating (condenser) coils in the same test setup simply by using different combinations of open and closed valves in the refrigerant loop in addition to single-phase refrigerant tests.

The design and operation of this novel facility is presented which highlights its flexibility and features. Additionally, detailed operation is described for the loop in evaporator mode. A preliminary test plan is provided for the first coil that will be tested in the experimental setup.

Initially, tests will be performed in both the evaporator and condenser mode. The design of experiments method presented will be used to identify areas of critical sensitivity in need of additional experimental fidelity.

A detailed uncertainty analysis is also presented which determines the uncertainty propagation in the air and refrigerant side capacity based on the standard uncertainty of the selected instrumentation. It was found that the relative uncertainty in the refrigerant capacity is within 0.2% while relative uncertainty in the airside capacity is within 2% for all planned points in the initial test matrix. A preliminary experiment shows that the experimental facility confirms to the 5% energy balance limit on refrigerant and airside as per ASHRAE Standard 33.

In future, the numerical models will be compared against the high-fidelity experimental data obtained from the experimental facility.

CHAPTER III

VALIDATION OF A MULTI-CIRCUIT HEAT EXCHANGER MODEL FOR EVALUATING THE EFFECT OF REFRIGERANT CIRCUITRY ON CROSS-FIN CONDUCTION IN EVAPORATOR MODE

ABSTRACT

Air-to-refrigerant fin-and-tube heat exchangers can have active circuits directly adjacent to inactive circuits at part load conditions, leading to cross-fin conduction. Cross-fin conduction needs to be accounted for in heat exchanger modelling to accurately predict heat exchanger performance metrics. This study explores how refrigerant circuitry can influence cross-fin conduction in multi-circuit evaporator coils. Our advanced segment-by-segment heat exchanger model is validated against two-phase refrigerant data obtained from our experimental facility. Three, custom designed, multi circuit fin-and-tube heat exchanger coils with distinct refrigerant circuities were used for validation purposes, including an interleaved, vertical and block circuited coils, respectively. A total of 162 experiments with a range of refrigerant and air inlet conditions, at full load (all circuits active) and part load (some circuits active) were carried out. All tested coils results were compared against model results with evaporator capacities of 2 kW to 18 kW. At full load, for all coils, the differences in coil capacity between simulated and experimental capacities were no greater than 10%, for part load the differences are larger. For the test coil with interleaved circuitry, operating

with 3 of 8 circuits active, the mean average percentage error (MAPE) between experimental and simulated capacity was 2.7% when cross-fin conduction was considered, increasing to 7.7% when cross-fin conduction was ignored. Similarly, for the test coil with block circuitry, operating with 2 out of 4 circuits active, the MAPE between experimental and simulated capacity was 1.7% when cross-fin conduction was considered, and 3.4% when it was ignored. Overall, the results suggest that the effect of cross-fin conduction on coil capacity is directly proportional to the number of inactive circuits, and that its affect is more pronounced on interleaved circuitry compared to block circuitry, mainly due to larger proportion of inactive tubes directly neighboring active tubes at part load operation of the former, compared to latter.

This chapter is published in the International Journal of Refrigeration in 2021 (Saleem *et. al.,* 2021a).

3.1 Introduction and motivation

Air-to-refrigerant fin-and-tube heat exchangers are a staple in modern day Heating, Ventilation, Air Conditioning and Refrigeration (HVAC&R) equipment. As a result of their wide use, they are available in different sizes, have varying levels of refrigerant circuitry arrangement, and are subject to a wide range of operating conditions. All these factors play an important role in the performance of fin-and-tube heat exchangers. To accurately predict this performance, numerous simulation models have been developed. Based on the control-volume approach, these simulation models have four types (Sarfraz *et al.,* 2018), lumped element, moving boundary (or moving interface), tube-by-tube and segment-by-segment (or discretized). Overall model fidelity and computation time generally increases while transitioning from the lumped approach to segment-by-segment. The

tube-by-tube and segment-by-segment approach is used when investigating some notable heat exchanger phenomenon such as refrigerant and air side maldistribution and cross-fin conduction.

Cross-fin (tube-to-tube) conduction through heat exchanger fins is a phenomenon that can drastically influence the performance of heat exchangers when the operating conditions call for some of the circuits to be active (refrigerant flow in the tubes), while others to be inactive (no refrigerant flow in tubes). This situation is common when multi-circuit and multi-compressor packaged commercial AC units operate at part load. Cross-fin conduction can also occur when there is a notable difference in refrigerant side heat transfer rates of neighboring tubes, such as in gas (CO_2) coolers, and multi-circuit coils having non-uniform refrigerant flow rates.

Heun & Crawford (1994) analytically modelled a cross-counter flow fin-and-tube heat exchanger for investigating cross-fin conduction. They evaluated the capacity of two heat exchangers of identical size operating in evaporator mode, one having continuous fins and the other having split fins. The heat exchanger with continuous fins was found to have up to 40% less capacity than the one with slit fins.

Domanski *et al.* (2007) experimentally evaluated the effect of cross-fin conduction by using a single 5 kW evaporator coil run at superheats of 5.6°C and 16.7°C. For the test with superheat of 16.7°C, they observed a capacity reduction of 20% in the heat exchanger with slit fins, compared to that with slit split fins (*e.g.* split = tube depth rows separated from each by cut in fins). This indicated that overall superheat of a multi circuit coils will influence the impact of cross-fin conduction on overall coil capacity. Though cross-fin conduction has been shown to have demonstrable impact on fin-and-tube heat exchanger performance, many modern and advanced segment-by-segment models, such as CoilDesigner (Jiang *et. al*., 2006) and ACMODEL (Shen, 2006) do not consider it.

Sarfraz *et. al.* (2019a) developed a detailed segment-by-segment heat exchanger model (Xfin) that takes cross-fin conduction into account. The initial model validation was performed against single-phase experimental data obtained from an air-to-refrigerant heat exchanger, which was operated at both full and part load. It was found that the model capacity prediction differed from the experimental capacity by 20% when cross-fin conduction was ignored. In later work, (Sarfraz *et al.*, 2020), Xfin is validated using two-phase refrigerant data from a custom heat exchanger testing facility, developed by Saleem *et. al.* 2020 (detailed in Chapter 2). This validation used a single multi-circuit evaporator coil with 8 circuits. Tests included three cases: 7 circuits active, 4 circuits active, and 3 circuits active. In all test cases the refrigerant saturated suction temperature (SST), air inlet temperature, air inlet relative humidity, and the airflow rate over the test coil were kept constant, and the refrigerant mass flow rate was varied. It was found that the Xfin model predictions were within 0-8% of the experimental capacity for all test cases when cross-fin conduction was considered. However, a maximum difference of 30% was found between the model predicted capacity and experimental capacity when cross-fin conduction was not considered. It was found that the effect of cross-fin conduction on coil capacity is directly proportional to the number of inactive circuits in the coil. The previous study, which motivated the current work, was limited to only dry air inlet conditions, a single airflow rate, single superheat (SH), and limited refrigerant side capacities of 5.5-8.0 kW on a coil with fixed circuitry.

It is expected that the influence of cross-fin conduction on coil performance would be affected by its direction, which is dependent mainly on refrigerant circuitry. Refrigerant circuitry modifications are a cost effective method for improving performance of evaporator coils (Tosun *et. al.*, 2021). Several researchers have demonstrated the difference in coil performance by varying circuitries. Martínez *et. al.* (2010) presented an optimization technique for refrigerant circuitries of evaporators

44

and condensers using a commercial AC unit. They observed an improvement in COP of 6%-6.5% for the system running R410A. Bach *et. al.* (2014) investigated how the relative performance of evaporators with refrigerant and air side maldistribution could be improved by using active superheat control and passive interleaved circuitry. Simulations showed that a maximum of 75% and 95% of the losses due to maldistribution could be recovered by interleaved circuitry and superheat control methods, respectively. Although interleaved circuitry recovered lesser losses in evaporator capacity, its implementation cost was expected to be significantly lower than active individual circuit superheat control. Bahman & Groll (2017) investigated interleaved circuitry application in a packaged AC unit. They found that the interleaved circuitry method improved the cooling capacity and system coefficient of performance (COP) by 17% and 12%, respectively.

In literature, no study was found that evaluated the effect of cross-fin conduction experimentally by testing multi circuit coils at part-load with different circuitries and distinct sizes. Additionally, only the model validation by Singh *et. al.* (2008) compared experimental refrigerant temperatures with simulated temperatures, and that too for a supercritical carbon dioxide gas cooler, which is currently a niche application. This paper will extend the work from Sarfraz *et al.* (2020) and compare the predictions of the Xfin model against two-phase refrigerant experimental data for three different heat exchanger coils for full load (all circuits active) and part load (some circuits active) configuration. Tests were conducted over a wide range of refrigerant and air side inlet conditions and two different coil sizes. This, combined with the distinct geometries of the three test coils, allows for a robust validation of the Xfin model, by predicting how cross-fin conduction is influenced by refrigerant circuitry, coil size and operating conditions.

3.2 Experimental approach

This section provides details of the experimental facility used for obtaining validation data, details of the three heat exchanger coils tested, the inlet refrigerant and air side conditions for each of the test coils, and the data reduction method.

3.2.1 Experimental facility and test coils

The test facility for obtaining experimental data for model validation complies with ASHRAE Standard 33 (2016), which details the methodology for testing of air-cooling and air-heating coils in laboratories. The test facility is based on Sarfraz *et. al.,* (2020), with minor modifications of the test section to accommodate the different test coils. It consists of:

- A pumped refrigerant loop for controlling refrigerant conditions at coil inlet,

- A coil test duct for allowing conditioned air to flow over the test coil housed in it, and

- A psychrometric test facility to allow for precise control of air conditions at coil inlet as well as measurement and control of air flowrate.

The pumped refrigerant conditioning loop has been developed to operate with R410A and sized to test heat exchanger coils up to a capacity of 17.5 kW (5 tons). A schematic diagram of the refrigerant loop is shown in Figure 3.1 with detailed description of the refrigerant loop presented in Chapter 2. Major components of the loop are:

- Variable speed refrigerant pump - provide refrigerant flow through the system,

- Modified heat pumps with a combined cooling capacity of 21.1 kW (6 tons) - used to provide cooling when testing evaporator coils and heating when testing condenser coils,

- Trim heating loop with capacity of 18 kW controlled by a Silicon Controlled Rectifier (SCR) - controls the inlet refrigerant temperature to the test coil, and

- Electronic expansion valves (EXV) at each circuit inlet - control the refrigerant flow rate entering that circuit; a control scheme comprising of three nested loops is used for adjusting their openings to achieve uniform refrigerant exit temperature at the outlet of all active circuits.
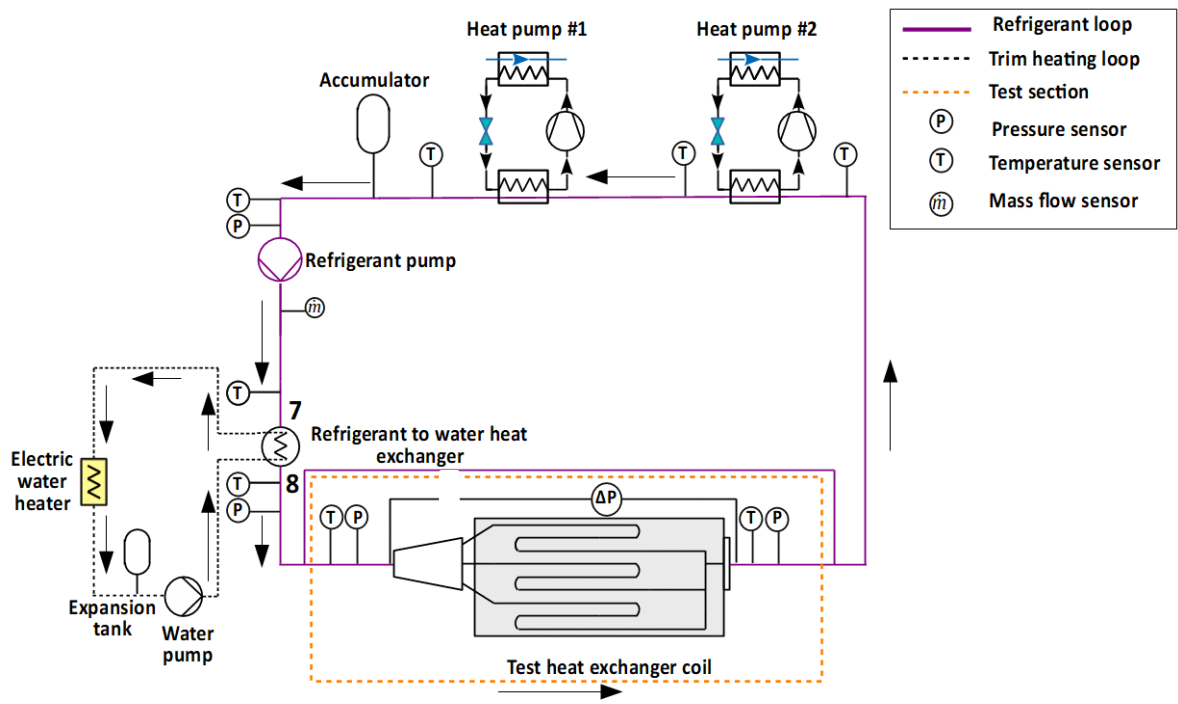
Figure 3.1. Schematic diagram of pumped refrigerant loop (modified from Chapter 2)

Two different coil test ducts are used to accommodate the two sizes of heat exchangers. Both ducts include:

- Two sampling devices for measuring the inlet and outlet average air, dry bulb (DB) and wet bulb (WB) temperatures,

- Flow straighteners for achieving uniform velocity to comply with ASHRAE Standard 33 (2016),

- Thermocouple grid (5 x 3) for verifying compliance with ASHRAE Standard 33 (2016)

A general schematic of the ducts is shown in Figure 3.2. Details of the two ducts, subsequently referred to as ducts A and B, are shown in Table 3.1. Both ducts need to be tested for compliance with ASHRAE Standard 33 (2016) for entering air DB temperature uniformity and air face velocity uniformity, and ASHRAE Standard 37 (2016) for air leakage. The upper limits and/or target values for each of the standards are shown in Table 3.2. Table 3.1 shows that both ducts comply with the limits of ASHRAE Standards 33 and 37. A detailed description of and the design and construction of test duct A is presented in Sarfraz *et. al.,* (2020). Duct A was used for testing coils #1 and #2, while duct B was used for testing coil #3 (see Table 3.1).
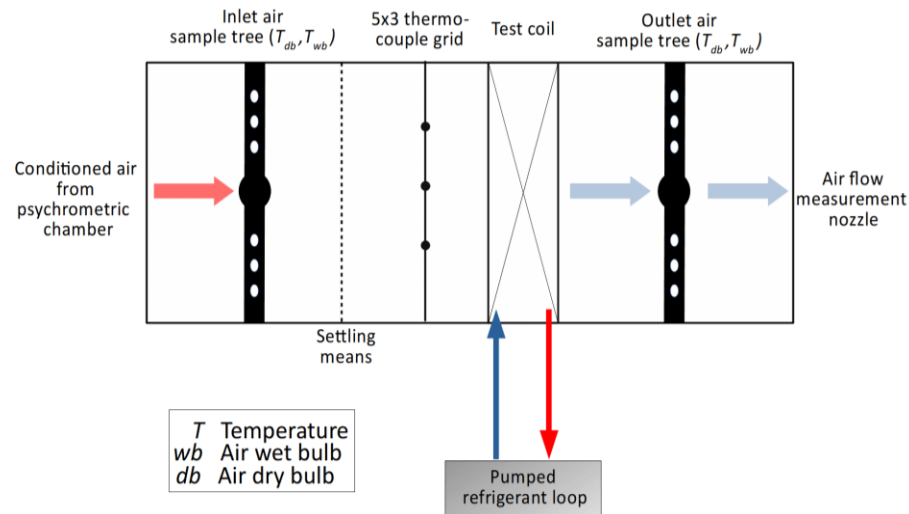
Figure 3.2. Schematic diagram of air side setup (modified from Chapter 2)

Table 3.1. Details of the two test ducts and results of compliance with ASHRAE testing standards

	Test duct A	**Test duct B**
Dimensions	1.2 m by 0.61 m (48 in. by 24 in.)	0.45 m by 0.41 m (17.5 in. by 16 in.)
Construction material	Insulated board	Sheet metal
Thickness	51 mm (2.0 in.)	0.76 mm (0.03 in.)
Coil(s) tested	#1, #2	#3
Air velocity uniformity test results	Highest face velocity exceeded lowest by maximum of 15%	Highest face velocity exceeded lowest by maximum of 17%
Air temperature uniformity test results	DB temperature had max. absolute deviation of 0.28°C (0.50°F)	DB temperature had max. absolute deviation of 0.48°C (0.86°F)
Air leakage test result[1]	0.42% relative to target flowrate of 1.1 m^3/s (2250 CFM)	0.40% relative to target flowrate of 0.32 m^3/s (675 CFM)

Table 3.2. Thresholds of various parameters and the respective standards that test ducts A and B need to comply with

Standard	**Parameter**	**Upper limit /target value**
ASHRAE Standard 33 (2016)	Entering air DB temperature	$\pm$ 0.6°C (1°F) deviation from average entering DB temperature
ASHRAE Standard 33 (2016)	Air face velocity	Highest air face velocity cannot exceed lowest by more than 20%
ASHRAE Standard 37 (2009)	Air leakage	Cannot exceed 1%

Table 3.3 shows the schematics of the three test coils, along with geometric parameters. Coils #1 and 3 have interleaved and block tube circuitries respectively, that are representative of typical residential and commercial evaporator coil geometries. Coil #3 is also significantly smaller than coils #1 and #2 and will provide information on the influence of the tube length and total coil height. Coil #2 has a vertically circuited geometry, which is not typical in application but serves as an extreme case for model validation. All three test coils have smooth tubes, which was necessary to ensure that model validation data obtained for this work should be pre-competitive.

---

[1] Static pressure found for target flow rates of 1.1 m^3/s and 0.32m^3/s for ducts A, and B respectively. Leakage rates then found at the target static pressures for the two ducts, at the targeted air flow rates.

Table 3.3. Schematics and geometrical parameters of test coils

	Coil #1	Coil #2	Coil #3
Schematic			
No. of circuits	8	5	4
No. of rows	4	5	3
No. of tubes per row	24	24	16
No. of tubes per circuit	12	24	12
Tube type	Smooth		
Tube material	Copper		
Tube wall thickness	$0.51 \cdot 10^{-3}$ m		
Tube outer diameter	$9.53 \cdot 10^{-3}$ m		
Tube longitudinal spacing	$2.19 \cdot 10^{-2}$ m		
Tube traverse spacing	$2.54 \cdot 10^{-2}$ m		
Tube length	1.219 m		0.593 m
Fin type	Wavy		
Fin thickness	$1.14 \cdot 10^{-4}$ m		
Fins spacing	$1.57 \cdot 10^{-3}$ m		
Half wavelength of fin wave	$5.51 \cdot 10^{-3}$ m		
Wave amplitude	$2.1 \cdot 10^{-3}$ m		

3.2.2 Test matrix

The experimental test plan for evaporator mode was formulated with a full factorial design of experiments approach (see Chapter 2), where refrigerant side capacity is the critical outcome of the experiments, and the following three variables were chosen as design factors:

- Air inlet velocity ($V_{a,i}$),

- Refrigerant SST, and

- Overall refrigerant superheat (SH).

Table 3.4 shows the test matrix for each test coil. All experiments of Table 3.4 will include two inlet air conditions, namely dry and wet, for which the air inlet DB temperature and RH are shown in Table 3.5. Refrigerant R410A is used as working fluid. Full load conditions were run by keeping all circuits active in each test coil, while part load was run by keeping only some of the circuits active. Each experiment was provided a unique test number, ranging from 1 to 162, each number corresponding to a specific test coil, load condition, refrigerant SST, refrigerant superheat, air inlet velocity, and air inlet condition.

Cross-fin conduction on heat exchanger performance is most prevalent when one or more of the circuits are inactive (Sarfraz *et. al.,* 2019a, Sarfraz *et. al.*, 2020). To best capture this, 96 out of 162 experimental test points, were conducted at part load conditions.

Table 3.4. Test matrix for each test coil; see Table 3.5 for air inlet conditions

Test coil	Active circuits	Saturated suction temperature (SST)	Air inlet velocity ($V_{a,i}$)	Test Superheat (SH)	# of tests
Coil #1	1-8	7.22°C (45°F) 10°C (50°F) 12.8°C (55°F)	1 m/s (200 fpm) 1.5 m/s (300 fpm) 2 m/s (400 fpm)	8.33 K (15 R) 11.1 K (20 R)	36
	1,4,7				36
Coil #2	1-5	7.22°C (45°F) 12.8°C (55°F)	1 m/s (200 fpm) 1.5 m/s (300 fpm) 2 m/s (400 fpm)	11.1 K (20 R)	12
	1,3,5	7.22°C (45°F) 12.8°C (55°F)	1 m/s (200 fpm) 1.5 m/s (300 fpm) 2 m/s (400 fpm)	8.33 K (15 R) 11.1 K (20 R)	24
		10°C (50°F)	1 m/s (200 fpm) 2 m/s (400 fpm)	8.33 K (15 R) 11.1 K (20 R)	8
	1,5	10°C (50°F)	1.5 m/s (300 fpm)	11.1 K (20 R)	4
Coil#3	1-4	7.22°C (45°F) 10°C (50°F) 12.8°C (55°F)	1.2 m/s (240 fpm) 1.5 m/s (300 fpm) 2 m/s (400 fpm)	11.1 K (20 R)	18
	2,3	7.22°C (45°F) 10°C (50°F) 12.8°C (55°F)	1.5 m/s (300 fpm) 2 m/s (400 fpm)	8.33 K (15 R) 11.1 K (20 R)	24
				Total # of experiments:	**162**

Table 3.5. Air inlet conditions for testing in evaporator mode

Mode	Dry bulb temperature	Relative humidity
Evaporator dry	26.67°C (80°F)	25%
Evaporator wet	26.67°C (80°F)	50%

3.2.3 Data reduction

The main quantities of interest for the experiment are the overall refrigerant side capacity, $\dot{Q}_{ref}$, air side capacity, $\dot{Q}_{air}$, bulk superheat, $T_{sup,bulk}$, and overall average superheat, $T_{sup,avg}$, given as

$$\dot{Q}_{ref} = \dot{m}_r \cdot \left(h_{r,out} - h_{r,in} \right), \tag{3.1}$$

$$\dot{Q}_{air} = \dot{m}_{air} \cdot \left(h_{a,bht} - h_{a,aht} \right), \tag{3.2}$$

$$T_{sup,bulk} = T_{r,out,bulk} - SST, \text{ and} \tag{3.3}$$

$$T_{sup,avg} = \frac{\sum_{i=1}^{n} T_{r,out,i}}{n} - SST, \tag{3.4}$$

where $\dot{m}_r$ is the refrigerant flow rate, $h_{r,out}$ is refrigerant enthalpy at coil outlet, $h_{r,in}$ is refrigerant enthalpy at coil inlet, $\dot{m}_{air}$ is the air flow rate, $h_{a,bht}$ is humid air enthalpy before coil, $h_{a,aht}$ is humid air enthalpy after coil, $T_{r,out,bulk}$ is the refrigerant temperature at coil outlet, n is the number of active circuits, and $T_{r,out,i}$ is the refrigerant temperature at the exit of circuit number i.

The refrigerant mass flow rate is measured by a Coriolis flowmeter with an accuracy of ±0.05% of measured value, and a range of 0 to 1 kg/s. Refrigerant enthalpy at inlet and outlet of the coil is calculated using REFPROP 10 (Lemmon *et. al.*, 2018), by measuring temperatures and pressures using Resistance Temperature Detector (RTD) sensors and pressure transducers, respectively. The RTD sensors are calibrated to a reference thermometer with ±0.06°C rated accuracy and measurement range of 5 to 90°C. The pressure transducers have an accuracy of ±2.9 kPa and can measure from 0 to 3,447 kPa. The RTD at coil outlet also measures bulk superheat, while thermocouples soldered to the copper tubes at each circuit are used for calculating refrigerant temperatures at each circuit exit. The thermocouples have an accuracy of ±0.33°C after in-house calibration, and measurement range of 5 to 90°C.

The air volumetric flow rate was calculated using the differential pressure across a nozzle in the psychrometric chamber's code tester. The differential pressure transducer for measuring this differential pressure had a full scale (FS) accuracy of ±0.25% and a measurement range of 0 to 747 Pa. Other measurements required to calculate the air flow rate were DB and WB temperature at nozzle inlet (measured with RTD sensors calibrated to previously mentioned reference thermometer and measurement range of 5 to 75°C) and the pressure at nozzle inlet (measured with a differential pressure transducer with FS accuracy of ±0.25% and measurement range of -374 to 374 Pa, and a barometer with accuracy of ±0.03 kPa and measurement range of 80-110 kPa). To calculate air enthalpies before and after the test coil, the air inlet and outlet DB and WB temperatures are measured by RTD sensors that are also calibrated to the previously mentioned reference thermometer, and have a measurement range of 5 to 75°C. The air enthalpies are calculated using CoolProp 6.0 (Bell *et. al.,* 2014).The uncertainty propagation in the calculated quantities of interest, i.e., refrigerant and air side capacities, is determined by calculating the total uncertainties in their respective parameters, using ASME PTC 19.1 (2013).

For each of the parameters, the total uncertainty comprises of a combination of the systematic uncertainty, based on the standard accuracy of the instrumentation previously described, and the random uncertainty, which varies experiment to experiment. The uncertainty propagation method has been detailed in Chapter 2 for a preliminary experiment and is reflected in the figures in Section 4.

For each experiment, data is recorded for a period of 20 minutes at a sampling rate of 0.5 Hertz, once the following conditions are satisfied:

- The instantaneous refrigerant flow rate is within ±2% of the average, as per ASHRAE Standard 33 (2016),

- The average refrigerant and air side capacities are within ±5% of each other, to comply with ASHRAE Standard 33 (2016),

- The individual superheat of each active circuit is within ±1.5 K of the overall average superheat, and the overall average superheat is within ±0.5 K of bulk superheat, to ensure uniform refrigerant flow rate across all active circuits,

The average of the refrigerant and air side capacity is

$$\dot{Q}_{avg} = \frac{\dot{Q}_{ref} + \dot{Q}_{air}}{2}.$$ (3.5)

An example set of results are presented in Figure 3.3 and Figure 3.4, which show the steady state data recorded for an experiment on coil #1 with all 8 circuits active, for which the refrigerant and air side operational parameters are shown in Table 3.6.

Table 3.6. Operational parameters for a sample experiment shown in figures 3.3 and 3.4

Parameters	Target from Test Matrix	Results
Refrigerant SST	10°C (50°F)	10.4°C (50.8°F)
Refrigerant inlet pressure	Floating variables to allow control of superheat	1172 kPa (170 psia)
Refrigerant mass flowrate		0.075 kg/s (592 lbs./hr.)
Air inlet DB temperature	26.7°C (80°F)	26.7°C (80°F)
Air inlet relative humidity	26%	25%
Air volumetric flow rate	1.5 m³/s (3150 CFM)	1.4 m³/s (2968 CFM)
Air inlet pressure	Uncontrolled variable	98 kPa (14.2 psia)
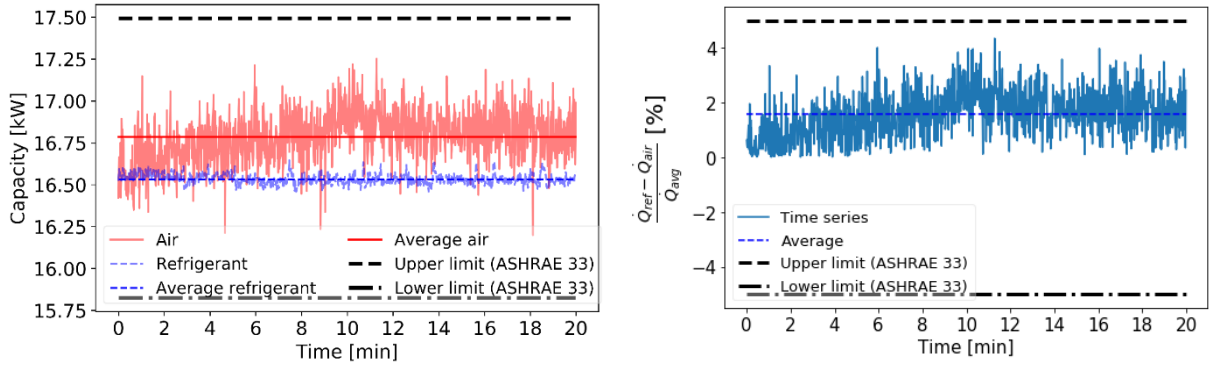
Figure 3.3. Energy balance on refrigerant and air side for a sample experiment, (1) Refrigerant and air side capacity, (2) Difference between air and refrigerant capacity expressed as a ratio to the avg. of the two
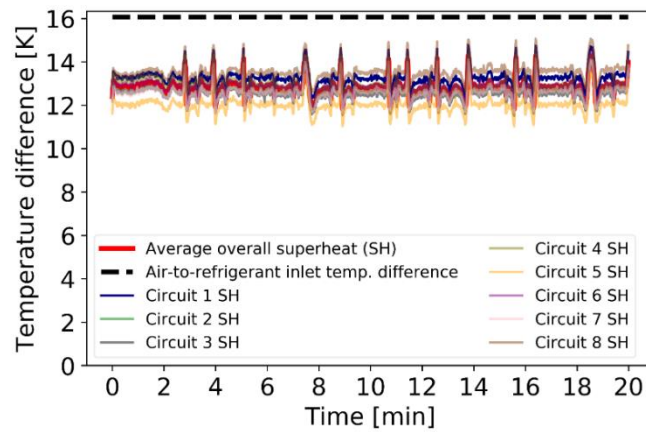
Figure 3.4. Overall average superheat and individual circuit superheat results for a sample experiment

3.3 Overview of cross-fin model

The cross-fin (Xfin) model is a detailed segment-by-segment fin-and-tube heat exchanger model developed by Sarfraz *et al.,* (2019a) that has the capability to evaluate cross-fin conduction between first-order neighboring tubes in the heat exchanger. The model allows the user to disable cross-fin conduction during the simulation process, called conduction ignored, so that its effect on the model`s capacity calculations can be determined. The model not only accounts for refrigerant and

moist air phase transitions, but also takes detailed input of the simulated heat exchanger`s geometry. Broadly, the model has a low-level segment solver that solves each exchanger segment, and an upper-level solver that can solve the entire heat exchanger by combining the simulation results of each segment in the refrigerant flow direction.

To calculate the heat transfer by cross-fin conduction, the individual segment solver requires the calculation of tube wall temperatures for each segment. Conduction shape factors required to calculate cross-fin conduction are evaluated by a simplified conduction shape factor equation presented by Lee & Domanski (1997). The refrigerant and air side heat transfers in the segment solver are evaluated by applying a lumped analysis using the ε- NTU method.

The upper-level solver connects and solves each individual segment solver in the refrigerant flow direction, in order to solve for the entire heat exchanger. This is accomplished by using heat exchanger circuitry and neighboring tube information. Circuitry information is incorporated in the Xfin model by adopting the algorithm developed by Jiang *et. al.,* (2006). Further details on the model development, including validation with single-phase experimental data, is included in Sarfraz *et al.,* (2019a).

In a previous work (Sarfraz *et. al.,* 2019b), another model that addresses cross-fin conduction was developed, but by associating the fin surface area of inactive tubes with active tubes by discretizing surface area. This model, called Fin Discretized (FD) took only 10% time of the simulation time of the Xfin model (conduction considered). However, the Xfin model was more accurate than the FD model by 1% and 1.5% for part load single-phase(Sarfraz et. al., 2019b), and part load two-phase data (Sarfraz *et. al.,* 2020), respectively. Additionally, the approach of fin area association cannot inform how pronounced the effect of cross-fin conduction is on different multi circuit coil

geometries. Thus, the Xfin model is the best modelling tool to address all the goals outlined in this paper.

3.4 Results and discussions

The model, Xfin, was utilized to compare the predicted refrigerant capacity against experimental refrigerant capacities, collected using the processes described in Section 3.2. The information in Tables 3.3-3.5 was provided as inputs to the model to run all simulations. Table 3.7 shows the correlations on refrigerant and air side provided to the model.

Table 3.7. List of refrigerant and air side correlations used in the model's simulation runs

Refrigerant (Single-phase)	Heat transfer	Dittus Boelter equation (Winterton, 1998)
	Pressure drop	Blasius equation (Blasius, 1913)
Refrigerant (Two-phase)	Heat transfer	Shah (1982)
	Pressure drop	Lockhart and Martinelli (1949)
Air	Heat transfer & pressure drop	Correlation for wavy fins (Wang *et. al.,* 1997)

Figure 3.5, 3.6, and 3.7 show parity plots to demonstrate how the experimental refrigerant capacities compare with the model predicted capacities of coils #1, 2, and 3, respectively. The comparison of experimental superheat with the model predicted superheat is given by Figure 3.8, 3.9, and 3.10. For each coil, simulations were run in two modes, (1) cross-fin conduction considered and (2) cross-fin conduction ignored, at full load, as well as part load configurations. The time taken to run the simulations with cross-fin conduction ignored was 5-10% of the time taken for simulations when cross-fin conduction was considered, which was also observed in Sarfraz *et. al.,* (2020). For each coil tested and simulated under each configuration, the parity plots indicate the upper and lower error bounds for 95% of the data. The agreement between experimental and simulated capacity is quantified by the Mean Absolute Percentage Error (MAPE),

$$MAPE = \frac{|\dot{Q}_{evap,exp} - \dot{Q}_{evap,sim}|}{\dot{Q}_{evap,exp}} \cdot 100\%, \qquad (3.6)$$

where $\dot{Q}_{evap,exp}$, and $\dot{Q}_{evap,sim}$ are the experimental and model predicted refrigerant side capacities, respectively. For quantifying the agreement between the experimental and simulated superheat, the Mean Absolute Error (MAE) is used, given by,

$$MAE = |T_{sup,exp} - T_{sup,sim}|, \qquad (3.7)$$

where $T_{sup,exp}$, and $T_{sup,sim}$ are the experimental and model predicted refrigerant superheat, respectively.

Figure 3.5, representing coil #1, covers a range of experimental capacities from 5-18 kW. This wide range is because at part load, less than half of all tubes are active, denoted in Table 3.4. In contrast, Figure 3.6, representing coil #2 shows experimental capacities from 10-18 kW. This reduced range is because its part load testing had 60% of the tubes active. Finally, Figure 3.7 shows that coil #3 covered a range of only 2.3-5.0 kW, since it is significantly smaller in size than coils #1 and #2.
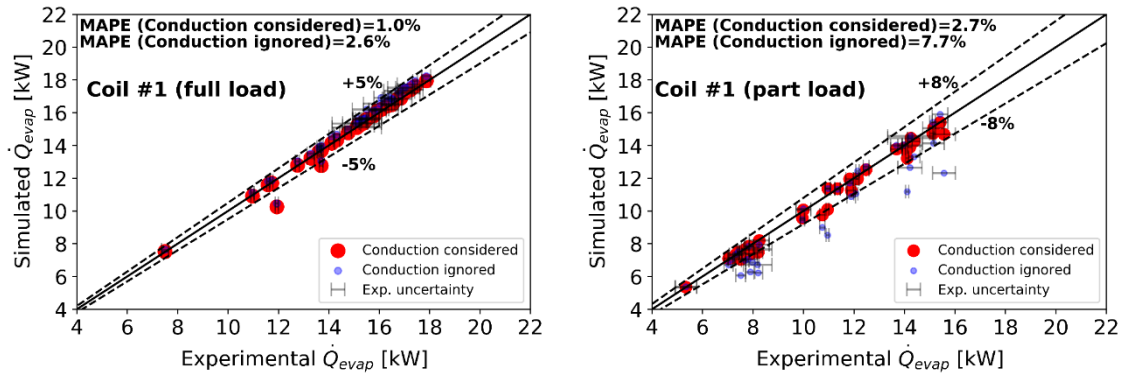
Figure 3.5 Comparison of model predicted refrigerant capacity with experimental data for coil #1 at full load (all 8 circuits active) and part load (circuits 1, 4 and 7 active only)
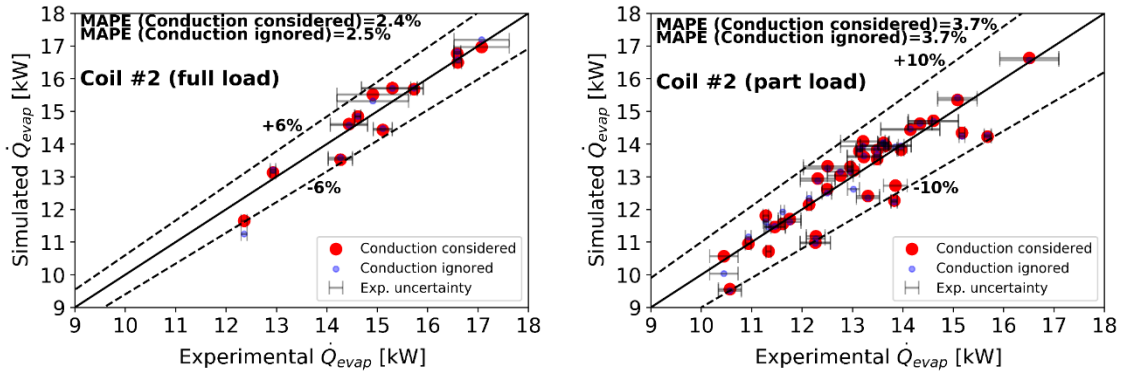
Figure 3.6. Comparison of model predicted refrigerant capacity with experimental capacity for coil #2 at full load (all 5 circuits active) and part load (circuits 1, 3 and 5 active only)
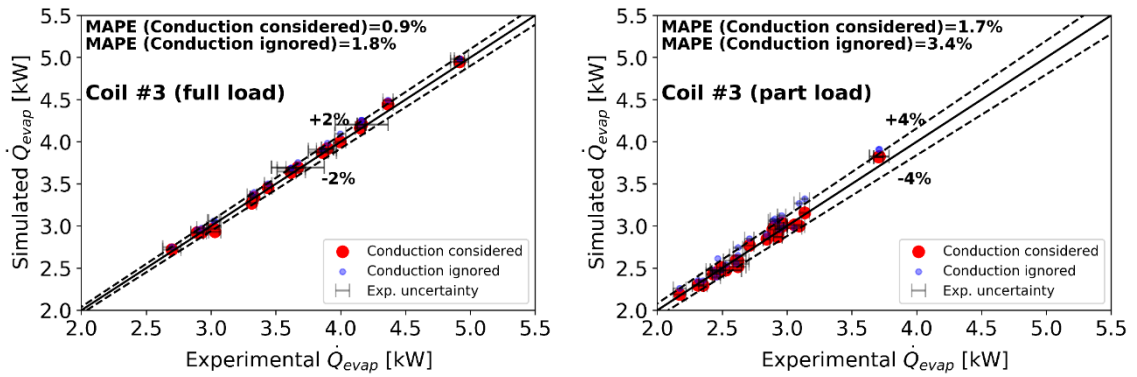
Figure 3.7. Comparison of model predicted refrigerant capacity with experimental data for coil #3 at full load (all 4 circuits active) and part load (circuits 2, and 3 active only)
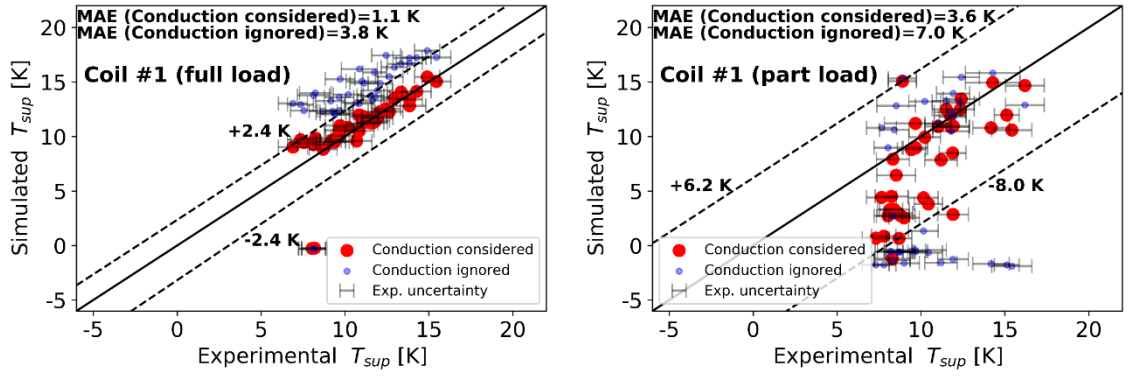
Figure 3.8. Comparison of model predicted superheat with experimental data for coil #1 at full load (all 8 circuits active) and part load (circuits 1, 4 and 7 active only)
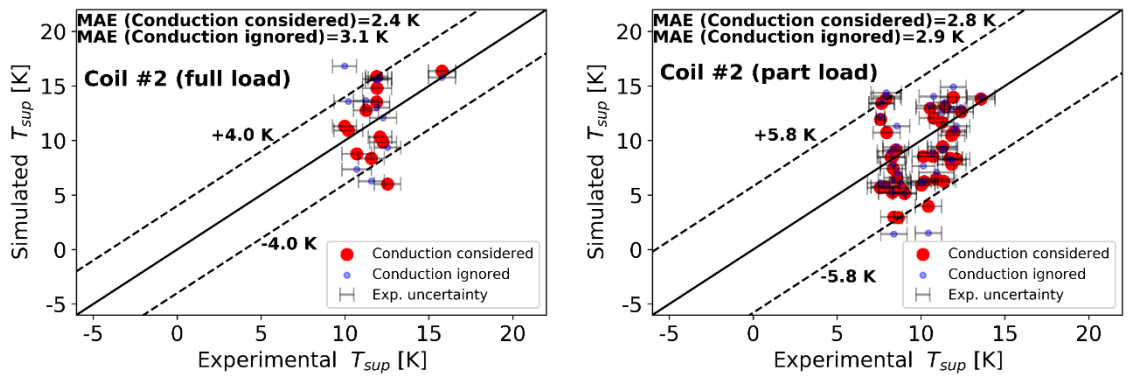
Figure 3.9. Comparison of model predicted superheat with experimental data for coil #2 at full load (all 5 circuits active) and part load (circuits 1, 3 and 5 active only)
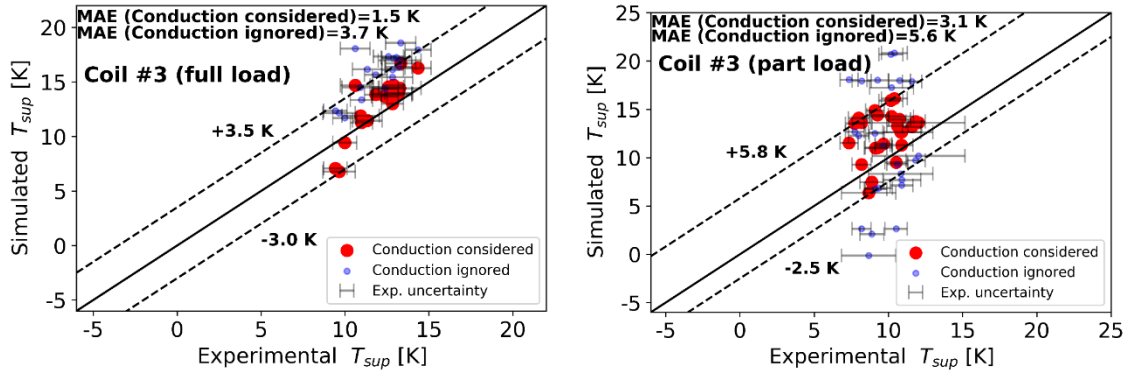
Figure 3.10. Comparison of model predicted superheat with experimental data for coil #3 at full load (all 4 circuits active) and part load (circuits 2, and 3 active only)

Figures 3.5, 3.6, and 3.7 show that when the coils are operating at full load (all circuits active), the MAPE between the experimental and simulated refrigerant capacities is 1.0%, 2.4%, and 0.9% of similar magnitude, regardless if cross-fin conduction is considered or not. Shown in Figure 3.7 and highlighted in Table 3.8, coil #3 has the lowest values of MAPE between experimental and simulated refrigerant capacities across all configurations (part load and full load), regardless of whether cross-fin conduction is considered or not. The major differentiation between coil #3 and the other coils is a much smaller size and capacity. It is hypothesized that these physical attributes are related to improved model predictions and this should be investigated further.

Figures 3.8, 3.9, and 3.10 show that the difference in MAE when cross fin conduction is considered for full load conditions, and when it is ignored is 2.7 K, 0.7 K, and 2.2 K for coils #1,2, and 3 respectively. This corresponds to the trend in MAPE differences in capacities of 1.6%, 0.1%, and 0.9% for coils#1, 2, and 3 respectively.

In order to explain the trends observed in Figures 3.5-3.10, at part load conditions, two new parameters are defined,

62

$$\lambda = \frac{Total\ number\ of\ active\ circuits}{Total\ number\ of\ circuits\ in\ test\ coil} \le 1, \tag{3.7}$$

and

$$\alpha = \frac{Number\ of\ active\ tubes\ with\ 1st\ order\ inactive\ neighboring\ tubes}{Number\ of\ inactive\ tubes\ with\ 1st\ order\ active\ neighboring\ tubes}. \tag{3.8}$$

Note that for a coil operating with all circuits active, λ will be equal to 1. The parameter α provides an indication of the ratio of active and inactive tubes that participate in cross-fin conduction. Table 3.8 shows the values of λ and α for each of the three coils when operating at their respective part load configurations. While calculating cross-fin conduction, Xfin model accounts only for inactive tubes that are immediately adjacent to active tubes, *i.e.*, first order neighboring tubes. This is because conduction between tubes through fins is inversely proportional to tube-to-tube distance and decreases with increasing distance between tubes (Incropera *et. al.*, 2011). Hence, the definition of α considers only the first-order neighboring inactive tubes.

The trends in MAE of superheat correspond to the trends in MAPE of coil capacity for each coil. For brevity, only coil capacity is used to explain the influence of cross-fin conduction on the coils when operating at part load.

From Table 3.8, the general trend for any coil operating at part load is that as λ becomes smaller, and α becomes larger, the MAPE between experimental and simulated refrigerant capacities by ignoring cross-fin conduction becomes larger. This implies that for multi circuit coils operating at part load with high values of α and low values of λ, the influence of cross-fin conduction on coil performance is more notable. This can be illustrated by analyzing the results for each coil.

Table 3.8. Assessment of cross-fin conduction in the test coils using data of active and inactive tubes

			Coil #1	Coil #2	Coil #3
Total # of active circuits at part load			3	3	2
Total # of circuits in test coil			8	5	4
λ (-)			0.38	0.60	0.50
# of active tubes with 1st order neighboring inactive tubes			36	72	6
# of inactive tubes with 1st order neighboring active tubes			41	48	6
α (-)			1.1	0.67	1.0
MAPE between experimental and simulated capacities	Full load	Cross-fin conduction considered	1.0%	2.4%	0.9%
		Cross-fin conduction ignored	2.6%	2.5%	1.8%
	Part load	Cross-fin conduction considered	2.7%	3.7%	1.7%
		Cross-fin conduction ignored	7.7%	3.7%	3.4%

It can be seen from for coil #1 operating with 3 out of 8 circuits active, the MAPE between experimental and simulated refrigerant capacities is 2.7% when cross-fin conduction is considered but it increases to 7.7% when cross-fin conduction is ignored. This is because the model ignored the effect of tubes of inactive circuits when cross-fin conduction is not taken into account, causing the model to significantly under predict coil capacity. Additionally, less than half of all tubes in coil #1 are active and have refrigerant flowing through them, and all of them are influenced by the neighboring inactive tubes. This results in it having the lowest λ and highest α out of all three test coils.

For coil #2 operating with 3 out of 5 circuits active, the MAPE between experimental and simulated refrigerant capacities are similar for when cross-fin conduction is considered or ignored *i.e.*, 3.7%. This is because compared to coil #3, coil #2 has a higher number of active circuit tubes (normalized with total number of tubes in the coil) and also has a lesser proportion of inactive tubes that are first-order neighbors of the active circuits, causing it to have λ higher and an α lower than coil#1. Therefore, capacity for a coil that has refrigerant circuitry like coil #2 will not be influenced notably

by cross-fin conduction when it is operating at part load.

For coil #3 operating with 2 out of 4 circuits active, the MAPE between experimental and simulated capacities is 1.7% and 3.4% when cross-fin conduction is considered and ignored, respectively. By comparing these errors to those of coil #1 (see Table 3.8), it can be observed that the amount of cross-fin conduction is higher in coil #1 compared to coil #3. This can be explained by the fact that:

- Coil #3 has a higher proportion of active tubes/circuits when compared to coil #1, *i.e.*, higher value of λ,

- Only 6 out of 24 active tubes in coil #3 have first-order neighboring tubes that are inactive, while all 36 active tubes in Coil #1 have first-order neighboring inactive tubes, *i.e.* lower value of α

Figure 3.11 shows the comparison of experimental coil capacities at part load of coils #1 and #3 compared against model predicted capacities, with conduction disabled. Thus, the results indicate that coil circuity (interleaved vs. block), combined with the values of λ and α dictate the extent to which cross-fin conduction would have an influence on the overall coil capacity when operating at part load.
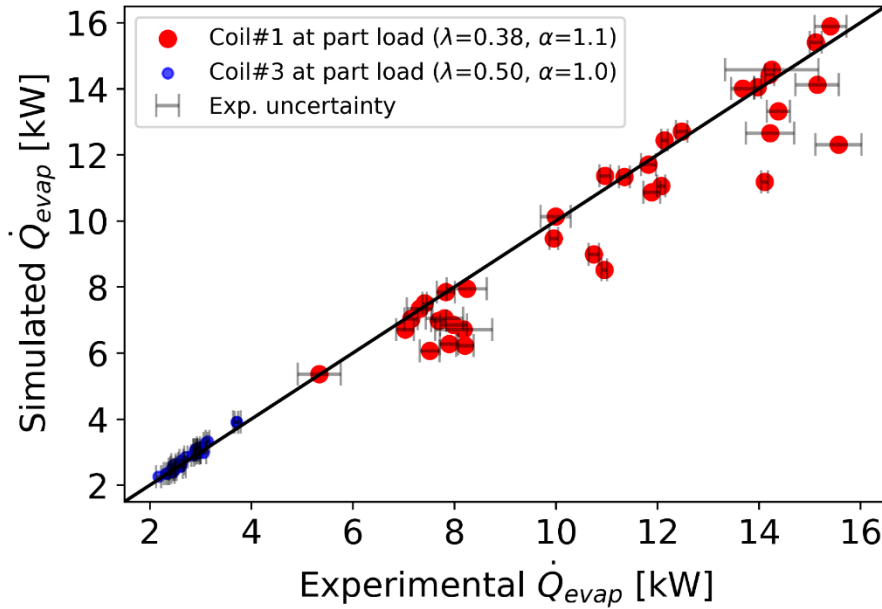
Figure 3.11. Comparison of model predicted coil capacities at part load of coils #1 and #3 with conduction disabled; showing the relation of λ and α values with impact of cross-fin conduction on coil performance

3.5 Conclusions

This paper presents the validation results of a discretized fin-and-tube heat exchanger model that takes the influence of cross-fin conduction into account. Three custom heat exchanger coils with distinct geometries were tested that included a range of geometry and circuitry variations. The experimental facility used for testing the coils in evaporator mode with two-phase refrigerant data complies with ASHRAE standards 33 (2016) and 37 (2009). A total of 162 test points were collected by testing the coils over arrange of inlet refrigerant and air conditions, operating at full load and part load. The experimental evaporator coil capacities ranged from 2 kW to 18 kW.

The experimental results were compared against model predicted results. Simulations were run in two modes, 1) cross-fin conduction considered and 2) conduction ignored. For part load

configuration in coil #1 when cross-fin conduction was ignored, the MAPE between experimental and simulated coil capacity was 7.7%, and the MAE between experimental and simulated refrigerant superheat was 7.0 K. However, for coil #3 operating at part load with cross-fin conduction ignored, the MAPE was only 3.4%, and the MAE was 5.6 K. For all coils operating at part load, the model was able to predict coil capacities within 0-10% of the experimental data when cross-fin conduction was taken into account.

Key results are:

- The effect of cross-fin conduction on coil capacity is minimal when all refrigerant circuits are active, regardless of coil capacity and circuitry,

- The amount of cross-fin conduction is inversely proportional to the number of active circuits normalized against the total number of circuits in the coil, *i.e.*, λ, and directly proportional to the ratio of number of active tubes that have inactive tubes as first-order neighbors to the number of inactive tubes that have active tubes as first-order neighbors, *i.e.*, α

- For heat exchangers with interleaved circuitry operating at part load, a large proportion of inactive tubes that are directly adjacent (first-order neighboring) to the active tubes have a significant impact on the coil capacity due to large amount of cross-fin conduction,

- For heat exchangers with blocked circuitry operating at part load, the effect of cross-fin conduction is not as significant as in interleaved circuitry. This is because not all the active tubes will have first-order neighbors that are inactive, resulting in lower amount of cross-fin conduction.

Overall, we expect the present study on investigating the relation of cross-fin conduction to refrigerant circuitry in multi circuit fin-and-tube heat exchangers to support manufacturers' cost-effective design of unitary equipment. It indicates that neglecting the effect of cross-fin conduction in their predictive modelling tools will lead to inaccurate prediction of heat exchanger performance, especially when some of the circuits are inactive. By using information on the heat exchanger circuitry, and the values of λ and α for the respective part load configurations, they will have an insight to how notable the effect of cross-fin conduction will be on coil performance. The manufactures/designers can then simulate part load coil performance by considering and also ignoring cross-fin conduction, to exactly observe how coil performance is different in the two modes.

In the future, simulations will be done at part load with heat exchangers having a variety of circuitry, so as to propose correction factors for heat exchanger models that do not calculate cross-fin conduction. Additionally, more refrigerants may be simulated, especially zeotropic refrigerant mixtures, that have significant temperature glide in the two-phase region.

CHAPTER IV

DROP-IN PERFORMANCE OF LOW-GWP ZEOTROPIC MIXTURES IN AN R410A WATER-SOURCE HEAT PUMP

ABSTRACT

Regulations aimed at mitigating climate change are forcing air conditioning (AC) and Water Source Heat Pump (WSHP) manufacturers to replace the existing halogenated refrigerants (chlorofluorocarbons and hydrofluorocarbons) in their systems with more climate friendly alternatives that have a lower Global Warming Potential (GWP). Some of the proposed low-GWP refrigerants to replace R410A are zeotropic mixtures of refrigerants. These refrigerants have a moderate to significant temperature glide that may have either positive or negative consequences in the refrigerant-to-water heat exchangers in WSHP. This study explores the ramifications of using zeotropic mixtures as ″drop-in″ replacements for R410A in WSHP in heating mode. A four-

component heat pump model is developed of a commercial R410A WSHP unit to operating in heating mode. The heat pump model consists of a moving boundary condenser, lumped element evaporator and a fixed efficiency compressor sub models. The model was validated against manufacturer data for an R410A WSHP, with 2.5% and 8.2% MAE in predicting the heating capacity and unit power consumption, respectively, in heating mode. The model was used to simulate the same system with R452B and R454B as "drop-in" replacements for R410A. Results

showed that R454B caused the system COP to increase by as much as 5%. The heating capacity of the system is also reduced for R452B and R454B by 4 and 6%, respectively. Additionally, for R454B, a reduction in Pinch Point Temperature Difference (PPTD) of up to 1.5°C is simulated which suggests a reduction of heat exchanger surface area may be possible while maintaining efficiency levels.

This chapter, with the exception of Table 4.2, is a technical paper that has been accepted for publication in ASHRAE Transactions (Saleem, S. & Bradshaw, C. R., 2022).

4.1 Introduction and Motivation

In recent years, regulations aimed at mitigating climate change, such as the Montreal Protocol, are forcing air conditioning (AC) and Water Source Heat Pumps (WSHPs) to replace the existing halogenated refrigerants (chlorofluorocarbons and hydrofluorocarbons) with more climate friendly alternatives. Some of these alternative low Global Warming Potential (GWP) refrigerants are zeotropic mixtures of refrigerants. Zeotropic mixtures (or non-azeotropic mixtures) are blends of two or more individual components, having different compositions of each component in the vapor and liquid phase at thermodynamic equilibrium as a saturated liquid-vapor mixture. At any given concentration, the zeotropic mixture will condense and boil over a temperature range. This non-isothermal evaporation and condensation is referred to as temperature glide. This glide, if matched with the temperature change of the source-side heat transfer fluid in the heat exchanger of a water source heat pump (WSHP), can result in reducing the thermodynamic irreversibilities in the heat exchangers (condenser and evaporator), as a result of improved heat exchanger effectiveness. The improved heat exchanger effectiveness ultimately transforms into an improved Coefficient of Performance (COP) of the system.

While temperature glide, can improve the system efficiency of a WSHP (Radermacher & Hwang, 2005), it may also cause significant errors in designing heat exchangers if their effects are ignored (S. P. Wang & Chato, 1995). Hence, understanding the potential ramifications of dropping-in a zeotropic mixture into their units is critical to ensure efficient operation of new, more environmentally friendly, WSHP products.

The present study explores the potential benefits of using zeotropic mixtures as "drop-in" replacements for R410A in a commercially available WSHP. A four-component heat pump model, comprising of a moving boundary condenser, lumped evaporator and fixed efficiency compressor, based on this WSHP was developed and was validated from the performance datasheet available from the manufacturer for R410A as refrigerant. Finally, simulations were run using two zeotropic mixtures, R454B and R452B, over a range of load side conditions, and the results were compared against R410A as the benchmark refrigerant.

4.2 Literature review

Several experimental and numerical studies have been done in recent years to investigate the effects of using low-GWP alternative refrigerants in ACs and WSHPs, with a wide variety of mixtures, testing environments and numerical modelling techniques. This section explores a variety of these studies, outlining the alternative mixtures used, and their potential advantages to the benchmark refrigerant, quantified by experimental and/or numerical studies.

Sethi & Motta (2016) evaluated R452B and R447B as drop-in replacements by running simulations, in heating and coooling mode, on a residential air-source heat pump. The heat pump comprised of air-to-refrigerant fin-and-tube heat exchangers as the evaporator and condenser.

The authors found that above ambient temperature below 35°C, both refrigerants showed a performance similar to R410A. Above 35°C, an increase in system efficiency of 3-4% was observed, with respect to R410A.

Devecioğlu (2017) evaluated how the seasonal efficiency of an air-source heat pump (comprising of fin-and-tube heat exchangers) was influenced by operating with R455A, R447A, R452B and R454B as drop-in alternatives to R410A. A validated numerical model of the heat pump was used to evaluate the COP and Energy Efficiency Ratio (EER) in heating and cooling mode. In heating mode, the capacities of R452B and R454B were found to be 3-5% lower than R410A. Another low-GWP zoetropic refrigerant mixture proposed as an alternative to R410A is R463A. This was evaluated by Hughes & Minor (2018) who showed through various tests, such as plastics and elastomers compatibility, dielectric properties, lubricant miscibility, and thermal stability test that R463A can easily replace R410A in commercial refrigeration and AC applications.

Chen *et. al.,* (2018) investigated the drop-in performance of R452B and R447B in air-to-water heat pumps with a sub-cooler vapor injection cycle designed for R410A. The test heat hump comprised of a plate heat exchanger as the condenser, and a fin-and-tube heat exchanger as the evaporator. Tests were conducted in heating as well as cooling mode. It was found that the improvement in COP of the system for the R452B system is 4-9% and 1.4-2.4%, and that of the R447B system is 3-12% and 0.4-3.8% with and without vapor injection, respectively.

Zühlsdorf *et. al.,* (2018) developed a numerical model of a water-to-water heat pump where the aim was to find which zeotropic mixtures of refrigerants would best increase the unit performance. Results of the analysis showed that a reasonable glide match on the source side improved performance. For four different cases, the COP of the system was calculated. Each case assumed

the same temperature difference between the entering and exiting water temperatures on the sink side and the same heat source inlet temperature (of 40°C). In Case 1, the heat source was cooled down to 35°C, which step-by-step increased such that it was cooled down to 20°C in Case 4.

Interestingly, pure refrigerants showed the best performance for Case 1. For Case 4, a performance improvement of 20% was observed with several refrigerant mixtures having 5 K superheating, which increased to 27% without superheating.

Shen *et. al.,* (2018) did an experimental and numerical investigation on a rooftop air conditioner (RTU) , comprising of fin-and-tube heat exchangers as the evaporator and condenser, to evaluate drop-in alternatives for R22 and R410A. Results showed that refrigerants R457A and ARM20B would be the best replacements for R22. For R410A, R452B turned out to be a better alternative than R32. This is because with R452B, the required compressor displacement volume and the most optimum heat exchanger geometry configuration was identical to that of R410A, so as to achieve the same system performance.

Pardo & Mondot (2018) used an air-to-water reversible heat pump, an air-to-water heat pump water heater (HPWH) and a water-to-air heat pump to experimentally investigate low-GWP alternatives for R410A, R407C, and R134a. Refrigerants HPR2A, R447A, R454B, R459A, and R32 were evaluated as the alternatives to R410A in the 10 kW air-to-water reversible heat pump in heating and cooling mode (the type of heat exchangers in the unit were not mentioned). System performance was found to be almost indentical amongst all these fluids. Additionally, it was found that the system charge with these alternative refrigerants could be reduced by 15-24% when compared to R410A.

Heredia-Aricapa *et. al.,* (2020a) did a review to analyze low-GWP replacements for R134a. R404A

and R410A. It was found that R32, R466A, R447A, R447B, R452B, R454B, R457A, R459A, and ARM20B are the most promising alternatives to R410A in AC and heat pump equipment. R466A has also been investigated by Devecioğlu & Oruç (2020) in a variable refrigerant flow (VRF) based air-source heat pump. The COP with R466A was higher than R410A by 5-15% and 4% in cooling and heating mode, respectively. Like all other analysis of air-source equipment, the evaporator and condenser in this analysis were also fin-and-tube heat exchangers.

Li *et. al.,* (2021) did a study that simultaneously optimized low-GWP refrigerant mixture compositions and heat exchanger circuitry, using an experimentally validated 11 ton R410A rooftop RTU. Their simultaneous optimization lead to a 6% improvement in cycle efficiency and 49% reduction in flammability, at a GWP of 268. The study showed that zeotropic refrigerant mixtures with large temperature glide have a greater sensitivity to refrigerant circuitry, in comparison to pure refrigerants.

Sieres *et. al.,* (2021) performed drop-in tests on an R410A liquid-to-water heat pump with R454B and R452B. The heat pump for the experiments comprised of brazed plate heat exchangers as the desuperheater, condenser, and evaporator, and it was used for production of domestic hot water and space heating. Experiments were done for the three fluids with dffeerent charge amounts. The authors found that the optimum charge that provided the maximum system COP was lower for the alternatives in comparison to R410A. Additionally, R452B consumed lesser compressor electric power when compared to R410A, but had a lower system COP. R454B had similar COP to R410A, but heating capacities and compressor electric power inputs were upto 8% lower.

The previous studies almost exclusively featured air-source equipment with limited studies of drop-in performance of low-GWP refrigerants in WSHPs. Additionally, of the previous studies that

featured WSHPs, none of the the studies included coaxial heat exchangers as the refrigerant-to-water heat exchanger. The present work aims to qauntify the the performance of new low-GWP zeotropic refrigerant mixtures as drop-in replacements for R410A in a WSHP operating in heating mode. A thermodynamic model of a commercial WSHP with a coaxial heat exchanger is developed and initially validated using R410A performance data available from the manufacturer. The model is then exersized by simulating the use of "drop-in" refrigerant alternatives, R454B and R452B, and the results are compared to those obtained with R410A.

4.3 Methods

4.3.1. Refrigerant selection

R410A was selected as a baseline refrigerant, since it is widely used in water-source and air-source heat pump equipment not only in the United States, but also in Europe and other developed countries. Additionally, sufficient data pertaining to this popular refrigerant is available in open literature and from manufacturers to aid in validating the initial simulation model.

Although R410A gained popularity due to it being an HFC and not having chlorine that can destroy the ozone layer, it's very high GWP (2088 over a period of 100 years) has identified a need to phase out this fluid to accommodate regulatory changes (Calm, 2008). This change has generated a list of potential candidates with similar thermodynamic properties including zeotropic mixtures that have a lower GWP. For comparison purposes in this study, R452B and R454B were chosen. Both these refrigerants are becoming a popular replacement for R410A recently (ECACool, 2019 and COOLING POST, 2019) in various kinds of HVAC systems. Additionally, R452B has repeatedly appeared in literature as a replacement for R410A (Heredia-Aricapa *et. al.,* 2020). Table 4.1 lists

high-level information on the refrigerants used in this analysis. It must be noted here that both R454B and R452B have similar magnitudes of temperature glide; this will help to identify if temperature glide alone contributes to an improvement in performance when using these refrigerants as "drop-in" replacements (for R410A). R410A comprises of equal parts HFCs R32, and R125, R454B comprises of 68.9% R32 and 31.1% HFO R1234yf, and R452B comprises of 67% R32, 7% R125 and 26% R1234yf. Chemical structures of the pure fluids that make up the blends listed in Table 4.1, are shown in Table 4.2.
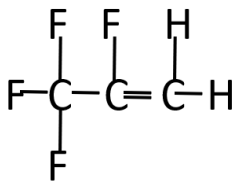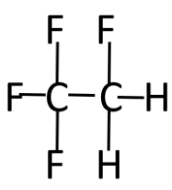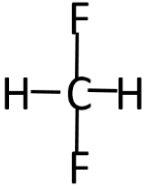
Table 4.1. Important characteristics of refrigerants chosen for the analysis

	R410A	**R454B**	**R452B**
Type	HFC/HFC blend	HFO/HFC blend	HFO/HFC blend
Global Warming Potential (GWP)	2088	467	676
Composition	R32/R125	R32/R1234yf	R32/R125/R1234yf
Mass fraction (%)	50/50	69/31	67/7/26
Ozone Depleting Potential (ODP)	0	0	0
Critical temperature	72.8°C (163°F)	77.0°C (171°F)	75.1°C (167°F)
Critical Pressure	4900 kPa (711 psi)	5041 kPa (731 psi)	4010 kPa (581 psi)
ASHRAE safety classification	A1	A2L	A2L
Glide	0.1 K (0.2 R)	1.5 K (2.7 R)[1]	1.0 K (1.8 R)[2]

---

[1] The Chemours Company (2014)
[2] The Chemours Company (2016)

Table 4.2. Chemical details of pure fluids that constitute the blends listed in Table 4.1

Refrigerant	R1234yf	R125	R32
Chemical name	3-tetraflouropropene	Pentafluoroethane	Difluoromethane
Chemical formula	CH_2CFCF_3	CF_3CHF_2	CH_2F_2
Chemical structure			

4.3.2. Thermodynamic model development and validation

The thermodynamic heat pump model was based on the basic vapor compression cycle, and it includes a moving boundary condenser model, lumped evaporator model and a fixed efficiency compressor model. The model is based on a commercially available 3-ton WSHP. A schematic of the WSHP of interest, operating in heating mode, is shown diagrammatically in Figure 4.1. This unit includes a hermetic scroll compressor and coaxial refrigerant-to-water heat exchangers for the condenser and evaporators.

The model was developed in Engineering Equation Solver (EES) (Klein, 2019). It uses a control volume analysis for each of the four model components as described in the following sections, which are then coupled together to form a system model. The fundamental assumptions for each of the model components are listed in Table 4.3.
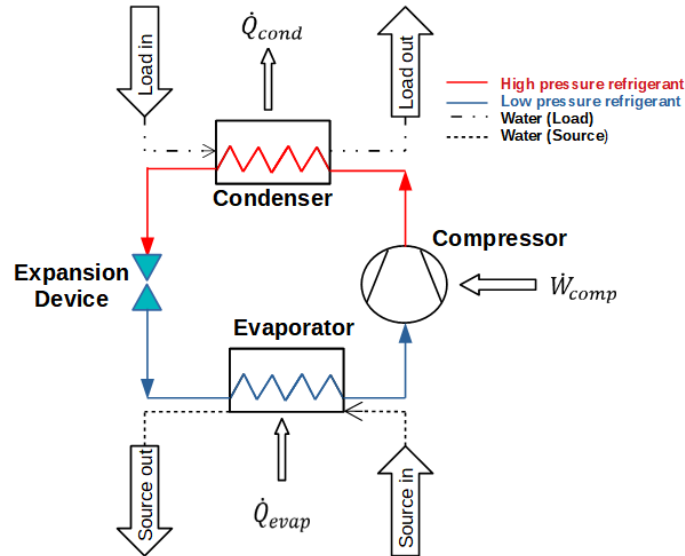
Figure 4.1. Schematic of the WSHP cycle operating in heating mode

Table 4.3. Major assumptions for all the components in the thermodynamic heat pump model

Component	Assumption
Compressor	Fixed isentropic and volumetric efficiency
Evaporator	No pressure drops on water or refrigerant side
	No circulation of oil with refrigerant
Condenser	No pressure drops on water or refrigerant side
	No circulation of oil with refrigerant
Expansion device	No heat gains during expansion process

Additionally, it is assumed that: (1) pressure of water on the load and source side of system is equal to atmospheric pressure, (2) thermodynamic and transport properties of water along the heat exchangers are assumed constant, and (3) axial tube conduction is negligible.

For modelling heat exchangers, there are a total of four main appraoches based on the control-

volume treatment, lumped element, moving boundary (or moving interface), tube-by-tube and segment-by-segment (or discretized). The overall model fidelity and time for computation generally increases while moving from lumped to segment-by-segment approach. From the literature studied, recent efforts at heat exchanger modelling to analyze the effects of dropping-in zeotropic refrigerant mixtures into exisiting HVAC equipment have mainly gone the route of using a segment-by-segment model (Zühlsdorf *et. al.,* 2018), while some of them even went with the lumped appraoch (Sethi & Motta, 2016). Additionally, Huang *et. al.,* (2014) developed a segment-by-segment refrigerant-to-water heat exchanger model and concluded (by numerical studies) that a total of five segments is optimum for the lowest amount of computational effort but the best accuracy. This result indicates that it is not necessary to include large number of segments in the moving boundary model for refrigerant to water heat exchangers. These results, collectively, suggest the moving boundary approach will allow independent tracking of the refrigerant phases, tracking of mixture temperature through the heat exchanger and accuracy that is sufficient for this study. However, this complexity is only considered critical on the load-side of the device. Therefore, a moving boundary model will be utilized on the condenser and a simpler, lumped, approach will be utilized on the evaporator.

4.3.2.1 Evaporator model

The evaporator model is developed using the Effectiveness-NTU method and applying a lumped element approach for the entire heat exchanger. Figure 4.2 shows the evaporator as a control volume, highlighting the flow of water and refrigerant into it. At the evaporator inlet, thermodynamic properties of water are calculated at a pressure of 241 kPa (35 psi) and temperature of 10°C (50°F).

Figure 4.2. Control volume representation of water-to-refrigerant evaporator modelled using the lumped approach

For the evaporator, the heat transfer between the refrigerant and water is calculated using,

$$\dot{Q}_{evap} = \varepsilon_{evap} \cdot \dot{m}_{water,evap} \cdot c_{p,water,evap} \cdot \left(T_{evap,water,in} - T_{ref,evap,sat}\right),$$ (4.1)

where the effectiveness is calculated by,

$$\varepsilon_{evap} = 1 - \exp(-NTU_{evap}),$$ (4.2)

And,

$$NTU_{evap} = \frac{U_{evap} \cdot A_{evap}}{\dot{m}_{water,evap} \cdot c_{p,water,evap}},$$ (4.3)

where the area is 3 m^2 and the global heat transfer coefficient of 560 W/m^2-K is assumed as a representative value for water-to-brine heat exchangers (Cengel and Ghajar, 2015). The exiting water temperature from the evaporator can be calculated using,

$$T_{evap,water,out} = T_{evap,water,in} - \frac{\dot{Q}_{evap}}{\dot{m}_{water,evap} \cdot c_{p,water,evap}}.$$ (4.4)

4.3.2.2 Condenser model

Additional fidelity was given to the condenser to better capture the influence of temperature glide

in heating mode. Similar to the evaporator model, the condenser is solved by the Effectiveness-NTU method but additionally includes a moving boundary analysis to capture the contributions of subcooled, two-phase, and superheated regions in the condenser. This is best illustrated by a control volume representation of the condenser shown in Figure 4.3.
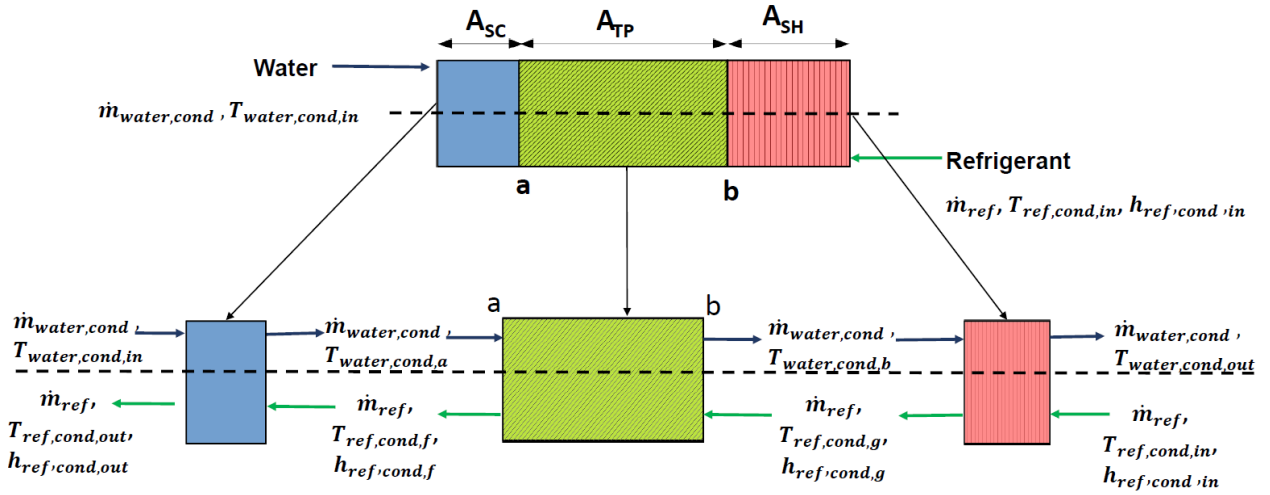
Figure 4.3. Control volume representation of water-to-refrigerant condenser modelled using the moving boundary approach. Point 'a' represents the transition point between subcooled (SC) and two phase (TP) region, while point 'b' represents the transition point between TP and superheated (SH) region

Equations (4.5) to (4.7) show the energy balances between the refrigerant and water in each of the three sections of the heat exchanger.

$$\dot{Q}_{cond_{SH}} = \varepsilon_{SH,cond} \cdot C_{min,SH} \cdot (T_{ref,cond,in} - T_{ref,cond,b}) \tag{4.5}$$

$$\dot{Q}_{cond_{TP}} = \varepsilon_{TP,cond} \cdot \dot{m}_{water,cond} \cdot c_{p,water,cond} \cdot (T_{ref,cond,g} - T_{water,cond,a}) \tag{4.6}$$

$$\dot{Q}_{cond_{SC}} = \varepsilon_{SC,cond} \cdot C_{min,SC} \cdot (T_{ref,cond,f} - T_{water,cond,in}) \tag{4.7}$$

Where the effectiveness relationships are,

$$\varepsilon_{cond,SH} = 1 - \exp(-NTU_{cond,SH}) \tag{4.8}$$

$$\varepsilon_{cond,TP} = 1 - \exp(-NTU_{cond,TP}) \tag{4.9}$$

$$\varepsilon_{cond,SC} = 1 - \exp(-NTU_{cond,SC}) \tag{4.10}$$

And the NTU relationships are,

$$NTU_{cond,SH} = U_{cond,SH} \cdot A_{cond,SH}/C_{min,SH} \tag{4.11}$$

$$NTU_{cond,TP} = U_{cond,TP} \cdot A_{cond,TP}/(\dot{m}_{water} \cdot c_{p,water,cond}) \tag{4.12}$$

$$NTU_{cond,SC} = U_{cond,SC} * A_{cond,SC}/C_{min,SC} \tag{4.13}$$

The global heat transfer correlations are calculated by,

$$\frac{1}{U_{cond,SH} \cdot A_{cond,SH}} = \frac{1}{\alpha_{water} \cdot A_{cond,SH}} + \frac{1}{\alpha_{ref,SH} \cdot A_{cond,SH}} \tag{4.14}$$

$$\frac{1}{U_{cond,TP} \cdot A_{cond,TP}} = \frac{1}{\alpha_{water} \cdot A_{cond,TP}} + \frac{1}{\alpha_{ref,TP} \cdot A_{cond,TP}} \tag{4.15}$$

$$\frac{1}{U_{cond,SC} \cdot A_{cond,SC}} = \frac{1}{\alpha_{water} \cdot A_{cond,SC}} + \frac{1}{\alpha_{ref,SC} \cdot A_{cond,SC}} \tag{4.16}$$

Where the heat transfer coefficients are calculated using the correlations listed in Table 4.4. The overall condenser capacity is then given by,

$$\dot{Q}_{cond} = \dot{Q}_{cond\,SH} + \dot{Q}_{cond\,TP} + \dot{Q}_{cond\,SC}. \tag{4.14}$$

Table 4.4. Refrigerant and water side convective heat transfer correlations used in condenser model

Fluid	Region	Correlation
Refrigerant	Single phase (superheated & subcooled)	Gnielinski (1975)
	Two phase	Shah (2013)
Water	Entire heat exchanger	Gnielinski (1975)

4.3.2.3 Compressor model

The compressor was modelled by specifying a fixed volumetric efficiency (98.5%) and isentropic efficiency (72.1%), along with the required parameters (displaced volume and rotational speed), as listed by the manufacturer. These values were determined using a minimization of error analysis between the compressor manufacturer data sheet and the error associated with the model.

The refrigerant mass flow rate, compressor work input and actual enthalpy of refrigerant exiting the compressor are given by Equations (4.15), (4.16), and (4.17) respectively.

$$\dot{m}_{ref} = \eta_{vol} \cdot \rho_{suc} \cdot V_{disp} \cdot \omega \tag{4.15}$$

$$\dot{W}_{comp} = \dot{m}_{ref} \cdot (h_{2s} - h_1)/\eta_{iso} \tag{4.16}$$

$$h_2 = h_1 + \left(1 - f_Q\right) \cdot \dot{W}_{comp}/\eta_{iso} \tag{4.17}$$

The value of the heat loss factor in Equation (4.17) for the compressor in all analysis is assumed to be 0.2, which is a value generally applicable for small to medium size hermetic compressors (Rasmussen & Jakobsen, 2000).

4.3.2.4 Expansion valve model

The expansion device for this heat pump is a balanced port thermostatic expansion valve (TXV).

The process in it is assumed isenthalpic and hence,

$$h_3 = h_4 \tag{4.18}$$

4.3.2.5 Integration of component models into 4 component heat pump model

Initially, all component models were developed independently and then coupled together. Figure 4.4 shows how all the various components communicate with each other in order to solve the model in a successive substitution fashion.
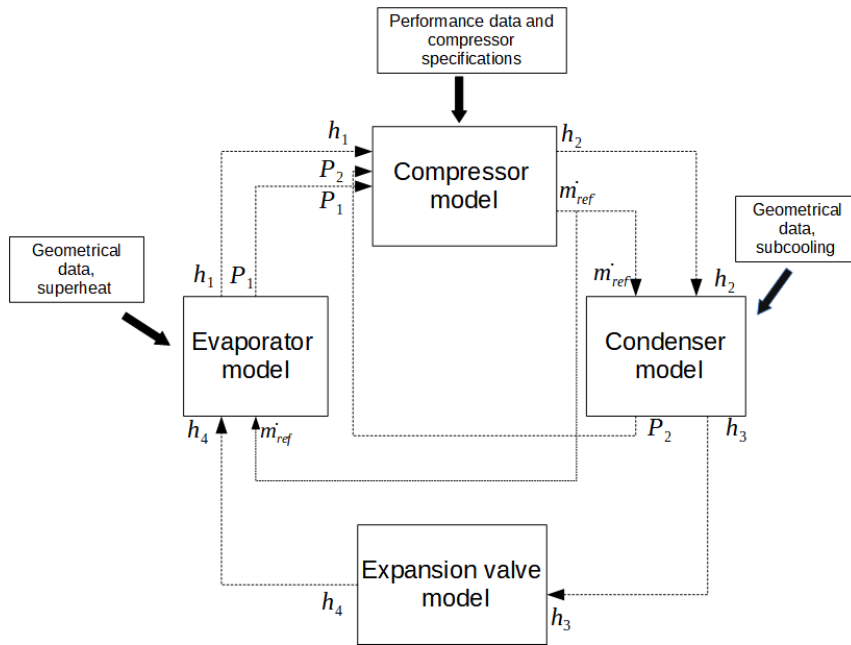
Figure 4.4. Flow of information in the heat pump simulation model

Finally, the system COP is calculated by,

$$COP = \frac{\dot{Q}_{cond}}{\dot{W}_{comp}} \tag{4.19}$$

4.3.3. Base model tuning and validation

The model was validated by comparing its predictions against the datasheet published by the manufacturer. The specifications of the heat pump are shown in Table 4.5, while specifications of the scroll compressor inside the unit are shown in Table 4.6. All values in Table 4.5 are based on load and source water flow rates of 0.567 kg/s. The heat pump was rated based on the criteria set by ANSI/AHRI/ASHRAE ISO 13256-2 (2012), with an uncertainty no more than 10% in the COP (Ertesvåg, 2011). It is therefore expected that the results from the datasheet obtained will fall within these parameters.

Table 4.5. Specifications and Performance data of the WSHP used for model validation as per AHRI/ASHRAE/ISO 13256-2

Cooling mode (Indoor 12°C (54 °F) and outdoor 30°C (86 °F))	Capacity	9.47 kW (2.7 tons)
	EER	4.28 W/W
Heating mode (Indoor 40°C (104°F) and outdoor 20°C (68°F))	Capacity	12.64 kW (3.6 tons)
	COP	4.90

Table 4.7 shows the range of the input variables the model was simulated for using R410A as the refrigerant, using three load flow rates of 0.284 kg/s (4.5 GPM), 0.428 kg/s (6.8 GPM) and 0.567 kg/s (9.0 GPM). A superheating and subcooling of 10°C (18 R) were provided as inputs to the model and were kept constant in all simulations. A total of 81 data points from the manufacturer were used to compare to the model predictions.

Table 4.6. Specifications and performance data of compressor in the WSHP unit

Mechanical data	Electrical data	1-phase, 208/230 V, 60 Hz	
	Displacement	6.19 m³/hour	
	Rotational speed	3600 RPM	
Performance data	Evaporating temperature /Condensing temperature	7.2°C /54.4°C (45.0°F /130°F)	10.0°C /37.8°C (50.0°F /100°F)
	Suction line temperature/Liquid line temperature	18.3°C /46.1°C (64.9°F /115°F)	21.1°C/29.4°C (70.0°F /84.9°F)
	Power	3070 W	2020 W
	EER	3.0 W/W	6.2 W/W
	Mass flow	0.0578 kg/s (459 lbs./hr.)	0.0661 kg/s (525 lbs./hr.)

The surface area on the refrigerant and water-side of the heat exchangers are critical inputs for model accuracy. The coaxial heat exchangers in the WSHP included unknown tube enhancements that increased the refrigerant and water-side surface areas. An estimation of the lower limit of the surface area was calculated assuming the heat exchanger was a simple tube-in-tube coaxial heat exchanger with smooth tubes. The total length of the heat exchangers is known so the total surface area was corrected by estimating an area density (area/length) that was used to tune the model results. This is represented by,

$$A_{cond} = A_{evap} = A_{density} \cdot L \tag{4.20}$$

And the coil length of the heat exchanger is calculated using,

$$L = \pi \cdot N_{coax} \cdot D_{coax} \tag{4.21}$$

Table 4.7. Range of input variables the initial model was simulated for, for three load flow rates

Source (evaporator) side inputs		Load (condenser) side inputs	
Entering Water Temperature (T_{ewi}), °C (°F)	**Water flow rate** $(\dot{m}_{ew})$, **kg/s (GPM)**	**Entering Water Temperature** (T_{cwi}), °C (°F)	**Water flow rate** $(\dot{m}_{cw})$, **kg/s (GPM)**
-6.67 (20.0)[1]	0.567 (9.0)	15.6, 26.7, 37.8 (60.1, 80.1, 100)	0.284, 0.428, 0.567 (4.5, 6.8, 9.0)
4.44 (40.0)	0.284 (4.5)	15.6, 26.7, 37.8 (60.1, 80.1, 100)	0.284, 0.428, 0.567 (4.5, 6.8, 9.0)
	0.428 (6.8)	15.6, 26.7, 37.8 (60.1, 80.1, 100)	0.284, 0.428, 0.567 (4.5, 6.8, 9.0)
	0.567 (9.0)	15.6, 26.7, 37.8 (60.1, 80.1, 100)	0.284, 0.428, 0.567 (4.5, 6.8, 9.0)
15.6 (60.1)	0.284 (4.5)	15.6, 26.7, 37.8 (60.1, 80.1, 100)	0.284, 0.428, 0.567 (4.5, 6.8, 9.0)
	0.428 (6.8)	15.6, 26.7, 37.8 (60.1, 80.1, 100)	0.284, 0.428, 0.567 (4.5, 6.8, 9.0)
	0.567 (9.0)	15.6, 26.7, 37.8 (60.1, 80.1, 100)	0.284, 0.428, 0.567 (4.5, 6.8, 9.0)
26.7 (80.1)	0.284 (4.5)	15.6, 26.7, 37.8 (60.1, 80.1, 100)	0.284, 0.428, 0.567 (4.5, 6.8, 9.0)
	0.428 (6.8)	15.6, 26.7, 37.8 (60.1, 80.1, 100)	0.284, 0.428, 0.567 (4.5, 6.8, 9.0)
	0.567 (9.0)	15.6, 26.7, 37.8 (60.1, 80.1, 100)	0.284, 0.428, 0.567 (4.5, 6.8, 9.0)

[1] The operational data provided by manufacturer for this EWT (below freezing point of water) is based upon a 15% methanol antifreeze solution

The heat exchanger had an outer diameter of 0.35 m and a total of 2 rounds so the length was calculated as 2.1 m. A correction factor is also introduced as a constant value to adjust the refrigerant-to-water convective heat transfer coefficients of the evaporator and condenser, shown by Equations (4.22) and (4.23) respectively.

$$UA_{evap,corrected} = UA_{evap} * CF \qquad (4.22)$$

$$UA_{cond,corrected} = UA_{cond} * CF \qquad (4.23)$$

The simulation model was tuned to the actual heat pump performance (from the performance data) by iterating on the heat exchanger area density ($A_{density}$) and on a correction factor (CF) until the Mean Absolute Percentage Error (MAPE) for the heating (condenser) capacity and compressor power were no more than 3% and 10% respectively.

After undergoing this process, $A_{density}$ was found to be 1.36 m^2/m^2, while the value of CF is 0.7. Table 4.8 presents the complete results of the model comparison listed as the percentage of the maximum, minimum and absolute errors obtained between the model predictions and datasheet values of condenser capacity and compressor power input, by running the mode for the range of input variables shown in Table 4.7.

The compressor model was independently compared against the compressor datasheet, the MAPE for which came out to be only 3.9%, whereas it was a high as 9.1% (Table 4.8) when validating the heat pump model against the compressor power in the heat pump`s datasheet. This indicated that part, but not all, of the error in the compressor power predictions in the heat pump model was due

to assuming fixed isentropic and volumetric efficiencies, as mentioned Section 4.3.2.3.

Table 4.8. Comparison of simulated and actual (datasheet) values of condenser capacity and compressor input power

Parameter	Load water flow rate ($\dot{m}_{cw}$), kg/s (GPM)	MAPE (%)
Condenser capacity ($\dot{Q}_{cond}$)	0.284 (4.5)	2.8%
	0.428 (6.8)	2.3%
	0.567 (9.0)	2.3%
Compressor input power ($\dot{W}_{comp}$)	0.284 (4.5)	7.4%
	0.428 (6.8)	8.1%
	0.567 (9.0)	9.1%

The simulated and actual heat pump COP were also compared, and it was found that the overall MAPE between the results was 7.1%, 8.4% and 9.3% for load flow rates of 0.284 kg/s (4.5 GPM), 0.428 kg/s (6.8 GPM) and, 0.567 kg/s (9.0 GPM), respectively. Thus, an average MAPE of 8.3% in COP prediction and the overall MAPE trends between simulated and actual (datasheet) suggest that the model will have sufficient accuracy for comparing performance for various refrigerants and look for trends in the results.

4.4 "Drop-in" simulation results

After validating the heat pump model, trends were explored for three refrigerants, R410A, R452B and R454B. The source (evaporator) side inlet water temperature and flow rate were kept constant, while on the load (condenser) side, the EWT was varied for three water flow rates, as shown in Table 4.9. For each simulation, the model simultaneously solved to obtain the refrigerant mass flow

rate, compressor input power, condenser capacity, evaporator capacity, and system COP, when given fixed superheat and subcooling, along with the variables shown in Table 4.9.

Table 4.9. Range of inlet variables for comparison of simulations for the different refrigerants

Source EWT (T_{ewi}), °C (°F)	4.44 (40.0)
Source flow rate, kg/s (GPM)	0.567 (9.0)
Load EWT (T_{cwi}), °C (°F)	10.0-32.2 (50.0-90.0)
Load flow rate, kg/s (GPM)	0.284, 0.42, 0.567 (4.5, 6.8, 9.0)

Condenser capacity, compressor power and the system COP were used as the main performance parameters. Figure 4.5, 4.6, and 4.7 show how the predicted condenser capacity, compressor work input and system COP varied for the three refrigerants respectively, as a function of load side entering water temperature for three different load flow rates.
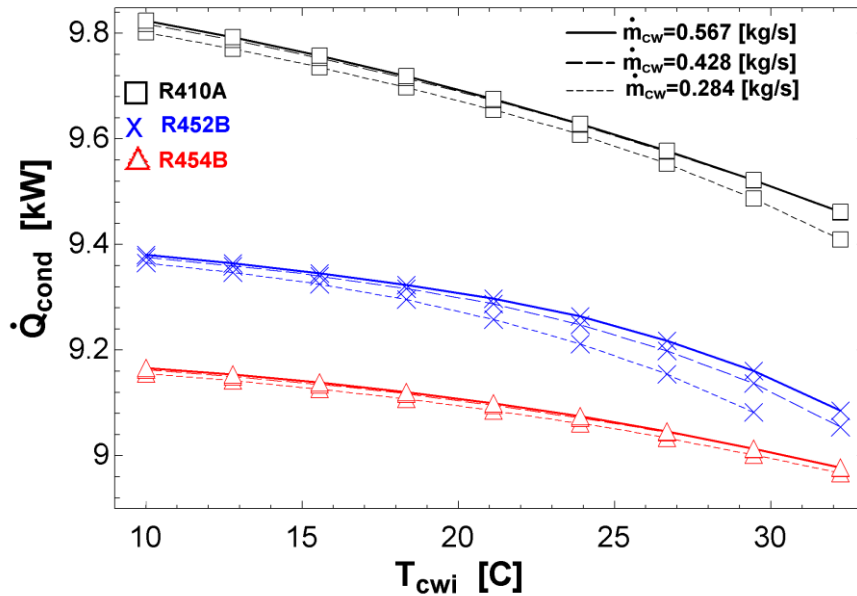
Figure 4.5. Comparison of simulated condenser capacity for varying entering water temperature and three flow rates

90
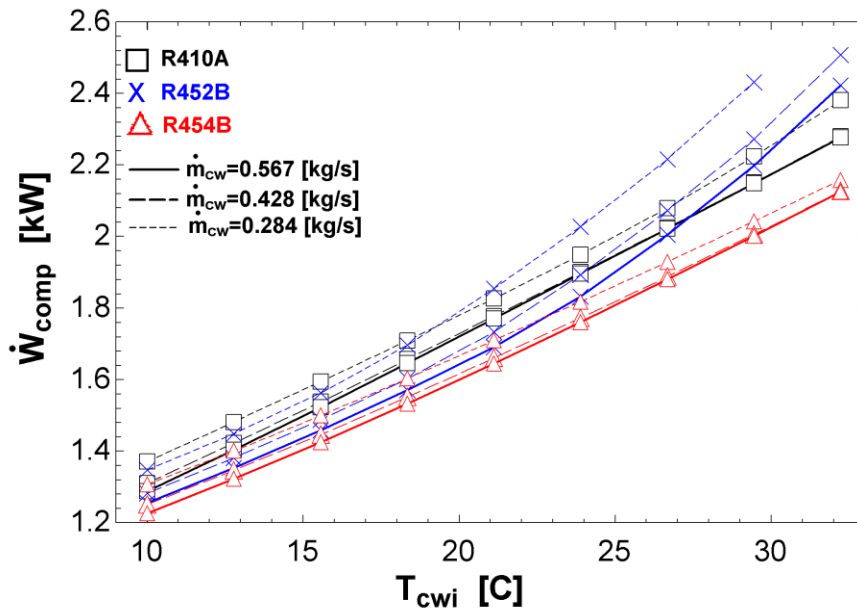
Figure 4.6. Comparison of simulated compressor power input for varying entering water temperature and three flow rates
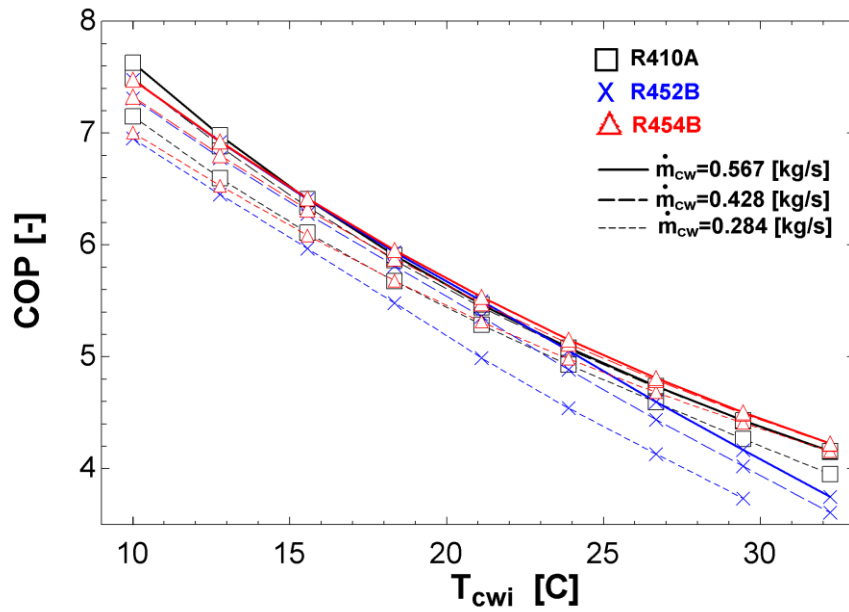
Figure 4.7. Comparison of simulated system COP for varying entering water temperature and three flow rates

91

From Figure 4.5, it can be seen that the condenser capacity is highest for R410A, followed by R452B and R454B. R452B presents with roughly 4% less capacity compared with R410A and R454B roughly 6% less capacity compared with R410A. These trends are similar to those obtained from the analysis done on an air-source heat pump by Devecioğlu (2017) who showed that in heating mode, the capacities of R452B and R454B were found to be 3-5 % lower than R410A.

Figure 4.6 shows that in general R454B requires the smallest compressor work input, at all load flow rates, when compared to R410A and R452B. An odd phenomenon is observed in the trends of R410A and R452B; initially the former has a higher compressor work input than the latter, but beyond an EWT of 19°C (66.2°F) when the load flow rate is 0.284 kg/s (4.5 GPM), the trends reverse. For the load flow rates of 0.428 kg/s (6.8 GPM), and 0.567 kg/s (9.0 GPM), this occurs at EWTs of 24°C (75.2°F) and 27°C (80.6°F), respectively. Overall, the differences between the compressor power consumptions for each of the three refrigerants is low, with the maximum difference occurring of 16%, i.e., 0.4 kW, between R452B and R454B at load flow rate of 0.284 kg/s, when the EWT in condenser is 29°C (85°F). The results in Figure 4.6 also agree with the results of Devecioğlu (2017), since he found that the electrical power consumption of the compressor was similar for R410A, R452B and R454B. They also agree with the analysis done by Sieres *et. al.,* (2021), where the system COP for R452B was lower than that of R410A for the same operating conditions.

Figure 4.7 shows that for the lower condenser entering water temperatures, i.e., < 19°C (66.2°F), R410A has the highest COP, followed by R454B and finally by R452B. However, for higher entering water temperatures, R454B has the highest COP and that of R410A drops to 2nd in line.

In order to investigate the reasoning behind the trends in Figure 4.5- 4.7, trends in several other variables were observed as a function of increasing entering water temperature to condenser at the three load flow rates: (1) refrigerant flow rate, (2) enthalpy change across condenser, and (3) enthalpy change across compressor. For brevity, the afore mentioned variables were plotted for a single load flow rate of 0.284 kg/s (4.5 GPM) and are shown in Figures 4.8 to 4.10. Additionally, the pinch point temperature difference (PPTD) between the three refrigerants and water were plotted against the source EWT, also for a load flow rate of 0.284 kg/s (4.5 GPM), and are shown in Figure 4.11. The PPTD is defined as the minimum temperature difference between the hot (refrigerant side) and cold (water side) streams in the heat exchanger.
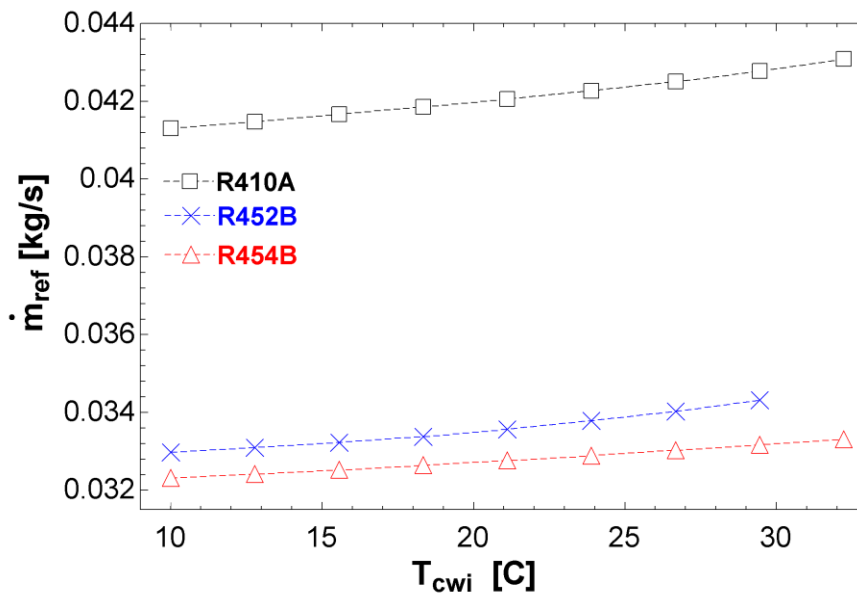
Figure 4.8. Comparison of simulated refrigerant flow rate for varying entering water temperature and load flow rate of 0.284 kg/s
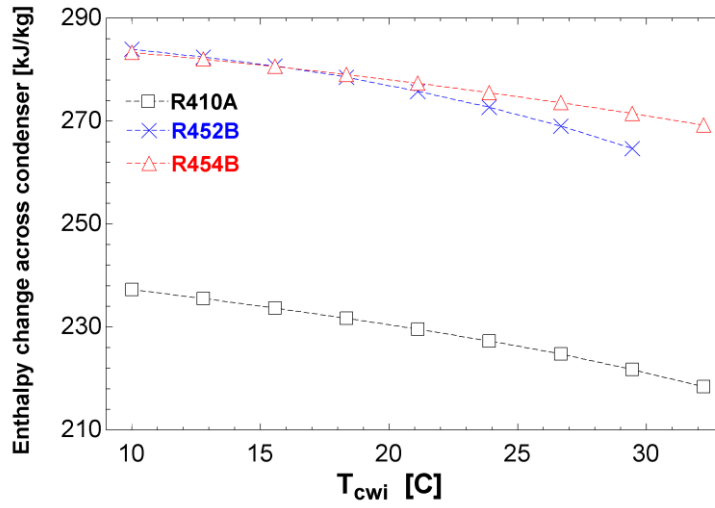
Figure 4.9. Comparison of simulated enthalpy change across condenser for varying entering water temperature with and load flow rate of 0.284 kg/s
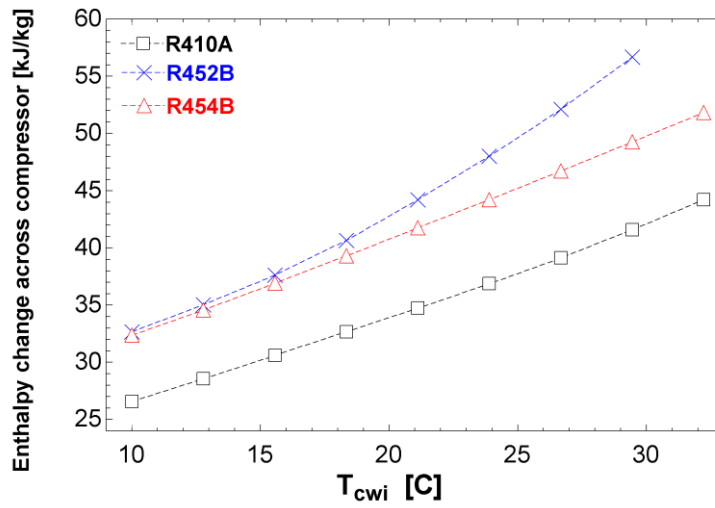
Figure 4.10. Comparison of simulated enthalpy change across compressor for varying entering water temperature and load flow rate of 0.284 kg/s
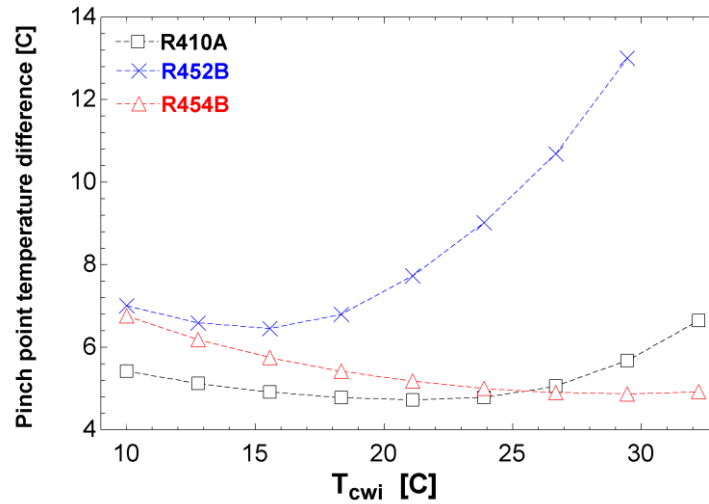
Figure 4.11. Comparison of simulated pinch point temperature difference across condenser for varying entering water temperature and load flow rate of 0.284kg/s

The results show that across the test entire simulation matrix (see Table 4.9), R452B had an average 20% lower refrigerant flow rate than R410A, while R454B had an average 22% lower refrigerant flow rate. On the other hand, enthalpy change in the condenser for R452B and R454B on average is greater by 19% and 21% respectively when compared to R410A. By referring back to Figure 4.5, it is evident that combined effect of the above two factors caused the condenser capacities for R452B and R454B to be lower by 4% and 6% respectively when compared to that for R410A.

The results in Figure 4.10 additionally show that the enthalpy change across compressor is lowest for R410A. This factor, combined with its relatively higher flow rate, helps to explain why it has a compressor work input that is in between that of R452B and R454B. It is also observed in Figure 4.10 that the trend in compressor enthalpy change for R410A and R454B is fairly linear, but for R4542B, the rate of this change increases beyond EWT of 19°C (66.2°F). Hence, this explains the trend in Figure 4.6, where the compressor work input for R452B exceeds that of R410A when EWT

>19°C (66.2°F). Additionally, it is important to mention here that the pressure ratio was lowest for R454B, followed by R410A, with R452B being the highest. The PPTD shows an overall trend of initial decrease and then increase for all three fluids. In case of R454B, it did not increase within the range of entering water temperatures in the test matrix, thus causing it to have the lowest PPTD beyond EWT of 25.5°C (77.9°F), followed by R410A and then R452B, as seen in Figure 4.11. R454B presents with roughly 1.5°C (2.7°F) lower PPTD compared with R410 (at EWT of 32°C (89.6°F)), whereas R452B has as high as 7°C (12.6 °F) higher PPTD (at EWT of 29.4°C (84.9°F)). The fluid with the lowest PPTD has the lowest amount of thermodynamic irreversibilities. Figure 4.7 confirms this by presenting the overall system COP, which correlates strongly with the inverse of PPTD. For R454B, the results suggest that the existing heat exchanger provides lower irreversibilities compared with R410A under some conditions, e.g., at load EWT greater than 25.5°C (77.9°F) for load flow rate of 0.284 kg/s (4.5 GPM), it could therefore have its area reduced without significant reduction in COP as a potential cost savings.

It can be observed that the alternative zeotropic refrigerants simulated in this study did not lead to an improved system performance when simply used as "drop-in" replacements in a system designed for R410A. Thus, design modifications would be necessary to fully leverage these zeotropic mixtures. One proposed modfication, as per the results in Figure 4.11 can be to reduce the effective surface area of an R410A heat exchanger when using R454B as the"drop-in" refrigerant, so as to match the heating capacity originally provided by R410A. To investigate another possible modification, a small parametric study was done for R454B for a single set of inlet conditions. By increasing the compressor displacement by 8.9%, the condenser capacity (shown in Figure 4.5) increased by 7%, *i.e.,* from 9.2 kW (2.62 tons) to 9.8 kW (2.79 tons), to match that of R410A at the same inlet conditions.

4.5 Conclusions

In this paper, a comparative study has been performed to explore the influence of using the zeotropic refrigerant mixtures, R452B and R454B as "drop-in" replacements for a 3 ton WSHP designed for R410A. This was accomplished by means of a moving boundary condenser model, and coupling it with a fixed efficiency compressor model and a lumped evaporator model developed in EES. The model has been validated using R410A performance data available from the manufacturer of a commercial water-to-water heat pump that features a fixed speed scroll compressor, coaxial heat exchangers and a TXV.

Overall, the analysis showed that simply using "drop-in" low-GWP replacements in existing WSHP may produce modest improvements or reductions in efficiency. It was found that, with high load-side water flow rates, the COP increased by as much as 5% with R454B when compared to using R410A. R452B had a lower COP when compared to R410A during all the simulations.

Both the drop-in alternatives result in lower heating capacity compared with R410A in all simulations; R454B has the lowest capacity degradation (6%) despite having the highest COP with R452B having a 4% reduction in heating capacity. The reduction in capacity of both fluids would require an increase in compressor displacement for applications where heating capacity is critical. The heat exchange efficiency of the two fluids also presented with modest differences. The pinch point temperatures of R454B were always higher than that of R410A where there were some operating conditions where R454B showed as much as a 1.5 °C (2.7°F) reduction in pinch point temperature. This suggests that heat exchange surface should be added to a R452B system where R454B systems may allow a reduction in coil surface area to save cost.

CHAPTER V

PERFORMANCE ASSESSMENT OF R1234ZE(E) AS A LOW-GWP SUBSTITUTE TO R410A IN FIN-AND-TUBE HEAT EXCHANGERS

ABSTRACT

Several energy efficiency regulations worldwide are forcing air conditioning and heat pump manufacturers to replace the halogenated refrigerants currently used in these systems, such as R410A, with more climate friendly alternatives that have a lower Global Warming Potential (GWP). This study explores how the performance of R1234ze(E) compares for an R410A based fin-and-tube evaporator coil. A total of 36 data points for both fluids were collected from a high-fidelity experimental facility to validate a segment-by-segment heat exchanger model. For R410A, the mean absolute percent error between the experimental and simulated capacity was found to be 0.9%, and it was 1.4% for R1234ze(E). Simulations were then carried out with R1234ze(E), where the fin density and refrigerant circuitry of the original heat exchanger were altered independently. By increasing the fin density from 15 to 20 fins per inch (FPI), the capacity increased by 4.9%, and refrigerant side pressure drop decreased by 4.5%. For the refrigerant circuitry optimizations, a maximum increase in capacity of 5.6% was observed when compared to the baseline, but at the expense of 7.5 times higher pressure drop. Alternatively, a separate circuitry resulted in a 38% pressure drop reduction and 2.5% reduction in capacity. The results demonstrated the relative

sensitivity of capacity and refrigerant side pressure drop for R1234ze(E) on the only two heat exchanger geometrical parameters. This sensitivity suggests potential for additional optimizations to heat exchanger designs for low-GWP refrigerants by performing further parametric analysis on heat exchanger geometry.

This chapter, with the exception of Table 5.7, is a paper under review for publication in the International Journal of Refrigeration (Saleem *et. al.,* 2021a).

5.1 Introduction and motivation

According to the US Energy Information Administration (EIA), electricity use for space cooling in US residential and commercial sector was about 392 billion kWh, which accounts for 10% of the total consumption of electricity in USA in 2020 (US EIA, 2020). The environment is not only affected by greenhouse gas emissions (GHGs) from the electricity generated that is used in these systems, but also because of leakage of refrigerants from these systems, such as R134a, R404A, and R410A. R410A is one of the most commonly used refrigerants in residential and light commercial Heating, Ventilation, Air Conditioning & Refrigeration (HVAC&R) systems. Unlike chlorofluorocarbons (CFCs), it does not harm the ozone layer but has a Global Warming Potential (GWP) of 2088, close to its applications predecessor (R22), and therefore needs to be phased out. Several regulatory measures worldwide, such as the F-gas Regulations (Schulz & Kourkoulas, 2014), the Kigali amendment to Montreal Protocol (UNEP, 2016), and most recently, a rule proposed by the US Environmental Protection Agency (EPA) under the American Innovation and Manufacturing Act rule (AIM, 2021), have called for gradual phase out of hydrofluorocarbons

(HFCs), such as R410A. Thus, R410A needs to be replaced by suitable lower GWP substitutes, ensuring that system performance metrics such as Coefficient of Performance (COP) and heating/cooling capacity, are not compromised in the process.

Several R410A alternatives have been investigated for AC and HP systems. For short-term replacement, many of the fluids being considered are refrigerant blends. Many include hydrofluoroolefins (HFOs) as a component, combined with HFCs. Some of the most common short-term alternatives are, in order of increasing GWP, are R457A, R459A, R454B, R446A, R447A, R452B, R32, R466A, and R447B (Mota-Babiloni *et. al.,* 2015, Haikawa *et. al.*, 2016, and Yu *et. al.,* 2021).

Some fundamental criteria that replacement refrigerants ideally should satisfy apart from their reduced GWP is similar or higher volumetric cooling capacity, similar or improved energy efficiency, and reduced flammability. All of these alternatives to R410A, except R466A, are mildly flammable, i.e. ASHRAE safety classification of A2L (ASHRAE Standard 34, 2019). Additionally, R466A has a relatively high GWP value. This shows that as of present, there are no long term low-GWP replacements of R410A that fulfill most of the fundamental criteria listed above.

A review completed by Bobbo *et. al.,* (2018) included publicly available experimental data of 16 HFO refrigerants. They concluded that thermodynamic and transport properties have only been investigated to a great extent for R1234yf and R1234ze(E). Since R1234ze(E) is an HFO, it exhibits a smaller volumetric capacity and latent heat when compared to R410A. R1234ze(E) has been mostly shown to be drop-in or light retrofit replacement for R134a. It has exhibited major benefits in modified vapor compression systems. Lee *et. al.,* (2013) developed a theoretical model for various multi-stage cycles with two-phase refrigeration injection, in which R1234ze(E) showed

better performance than R134a, R22, R410A, ammonia, R290, R600a, and low-GWP blends of R32 with other fluids. R1234ze(E) is also advantageous in HVAC applications, where energy consumption is a critical factor, such as high temperature heat pumps. Additionally, although R1234ze(E) is classified as a mildly flammable A2L refrigerant, it does not form flammable mixtures above 30°C. At ambient temperatures above 30°C, R1234ze(E) has flammability lower than other A2Ls such as R1234yf. Thus, with a GWP of 7, and for all the afore mentioned reasons, it can be an effective long-term low-GWP refrigerant for AC and HP systems.

Several system level studies investigated blends of different fluids with R1234ze(E) as drop-in replacements to R410A in vapor compression systems. Yu *et. al.*, (2021) performed a screening study to evaluate mixtures with no more than five components, their selection pool consisted of three HFOs, three HFCs and hydrocarbons CO_2 and R1311. Their optimization aimed to lower flammability, lower GWP, maximize system COP and achieve a similar volumetric efficiency as R410A. The screening results managed to fulfill the set criteria, but the authors concluded that further experimental study would be needed to validate their findings. Li *et. al.,* (2021) simultaneously optimized low-GWP refrigerant mixture compositions and heat exchanger circuitry, using an experimentally validated 11-ton R410A rooftop unit (RTU). The optimizations were done using the DOE/ORNL Heat Pump Design Model (HPDM). Their simultaneous optimization led to a 6% improvement in cycle efficiency and 49% reduction in flammability, at a refrigerant GWP of 268.

To improve the airside heat transfer in a fin-and-tube heat exchanger, several geometrical parameters may be modified, such as the tube diameter, tube wall thickness, fin thickness, and fin density. The effect of fin density for heat exchangers with wavy fins has been previously studied

by various researchers experimentally and by means of Computational Fluid Dynamics (CFD),e.g., Aliabadi *et. al.*, (2014), Chu *et. al.*, (2020), Okbaz *et. al.,* (2020), etc. However, those studies were mostly agnostic of the refrigerant used, indicating an opportunity to perform simulations to see how fin density correlates with heat exchanger performance, i.e., capacity, and refrigerant side pressure drop, for low-GWP fluids.

Another parameter that strongly affects heat exchanger performance is refrigerant circuitry. Circuitry modifications are a cost effective method for improving performance (Tosun *et. al.*, 2021). Such modifications are limited to tube connections (hairpins and return bends) without modifying the overall structure of the heat exchanger, such as the fin density, fin size, or number of tubes. Shen *et. al.*, (2018) simulated the performance of an R410A RTU with different evaporator and condenser circuitries, with five low-GWP replacements to R410A as the working fluids. They concluded that circuitry modification leads to a better system performance with the replacement refrigerants, when compared to R410A.

Very little literature exists that demonstrates performance comparison at only a heat exchanger (evaporator or condenser) level, as opposed to system level comparisons. Although finding the optimum blend of low-GWP alternatives that satisfy the criteria stated in the previous studies (reduced flammability, reduced GWP etc.) provides a long-term insight, the process of approval and marketing of a new blend can be a long and strenuous process. For example, in North America, approval is provided by EPA (2011) after a rigorous process. Moreover, the cost of the new blend compared to existing fluids can also be a hindrance in its market adoption. It is thus more practical to conduct comparison studies, either experimentally, numerically, or using a combination of both, using already available fluids. After that, optimization or parametric studies of modified heat

exchanger geometry and refrigerant circuitry for the low-GWP alternatives can allow determining optimum or near optimum performance.

This paper aims to generate an improved understanding of how low-GWP fluids affect the performance of fin-and-tube heat exchangers originally designed for R410A. Experiments are performed over a wide range of refrigerant and air side inlet conditions using R410A and R1234ze(E), on a four-circuit fin-and-tube heat exchanger. The experimental data is compared against an advanced segment-by-segment fin-and-tube heat exchanger model called cross-fin (Xfin), which has been extensively validated against R410A (Sarfraz *et. al.,* 2020 and by Saleem *et. al.,* 2021a, in Chapter 3). Parametric simulations are then carried out with R1234ze(E) as the working fluid, where the fin density and heat exchanger circuitry are modified independently to evaluate their effect on the heat exchanger capacity, superheat, and refrigerant side pressure drop.

5.2 Experimental approach

5.2.1 Experimental setup and test coil

The test facility utilized here has been similarly utilized and presented in several previous works (Sarfraz *et al.,* 2020 and Chapter 3). The facility consists of,

- A pumped refrigerant loop to control refrigerant conditions at test heat exchanger coil inlet,

- A coil test duct to allow conditioned air to flow over the test coil, and

- A psychrometric test facility to provide precise control of air dry-bulb (DB) temperature and relative humidity at coil inlet as well as measurement and control of air flowrate (Cremaschi & Lee, 2008).

The pumped refrigerant loop was developed to test a variety of refrigerants. It was sized to test heat exchanger coils up to a capacity of 17.5 kW (5 tons) with refrigerant R410A at a saturation suction temperature (SST) of 7.2°C (45°F). A schematic diagram of the refrigerant loop is shown in Figure 5.1 with a detailed description presented in Chapter 2. Major components of the loop are:

- A variable speed diaphragm pump for controlling and maintaining the refrigerant flow in the system,

- Two modified water-to-refrigerant heat pumps with a combined cooling capacity of 21.1 kW (6 tons) at SST of 7.2°C (45°F) to condense the superheated refrigerant when testing evaporator coils,

- Trim heating loop with a heating capacity of 18 kW that is controlled by a Silicon Controlled Rectifier (SCR) to set the desired liquid line refrigerant temperature for the test coil, and

- Electronic expansion valves (EXV) at inlet to each circuit to expand the refrigerant for ensuring uniform refrigerant mass flow rate distribution across all circuits.
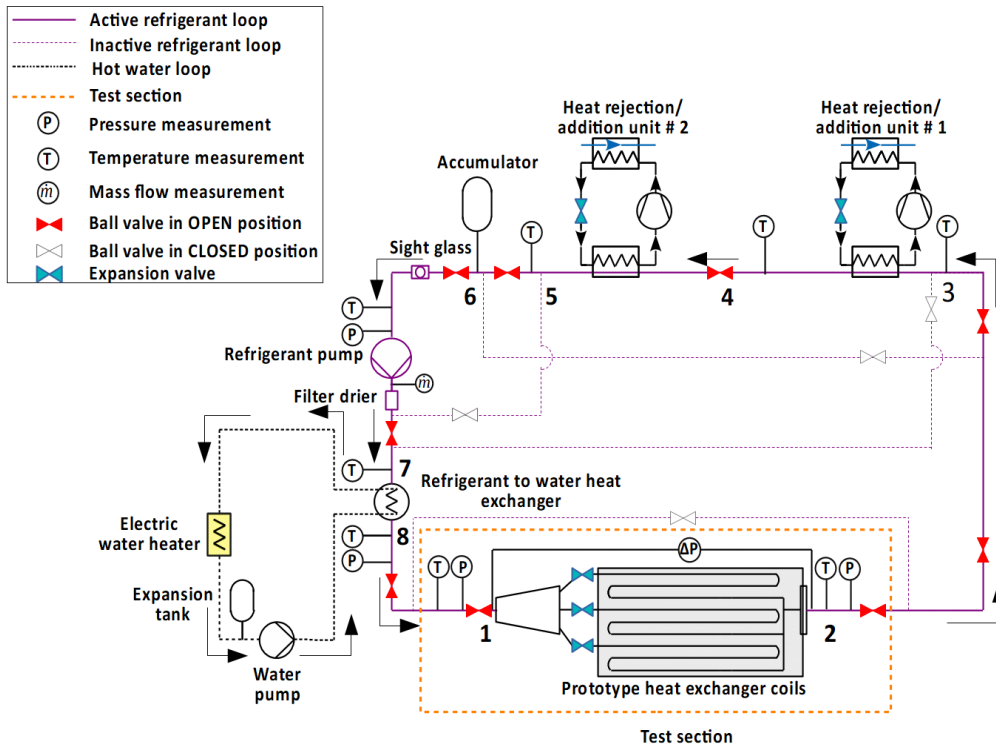
Figure 5.1. Schematic diagram of pumped refrigerant loop (operating in evaporator testing mode) and trim heating loop (modified from Chapter 2)

The coil test duct is constructed from sheet metal and insulated using rigid closed cell insulation with an R-value of 1.76°C m^2/W to ensure minimum heat leakage through duct walls during operation. It has an internal cross-sectional area of 0.45 m by 0.41 m (17.5 in. by 16 in.), and consists of:

- Sampling devices to measure inlet and outlet average air DB and wet-bulb (WB) temperatures,

- Flow straighteners to achieve uniform velocity for compliance of duct with ASHRAE Standard 33 (2016), and

- 5 wide by 3 tall thermocouple grid to verify compliance with ASHRAE Standard 33 (2016).

The test duct was found to be compliant with ASHRAE Standard 33 (2016) for entering air DB temperature uniformity and air face velocity uniformity, and with ASHRAE Standard 37 (2016) for air leakage (in Chapter 3) . A detailed description of a similar test duct used for testing a different heat exchanger coil on this experimental setup previously has been presented in Sarfraz *et. al.,* (2020).

The tested coil was designed as an indoor evaporator coil for R410A, having a capacity of 5.5 kW (1.6 ton), at 10°C (50°F) SST, 7.2 K (13 R) superheat, and 0.032 kg/s (250 lbs./hr.) mass flow rate. Figure 5.2 and Table 5.1 show the circuitry and, geometric parameters of the tested coil, respectively.
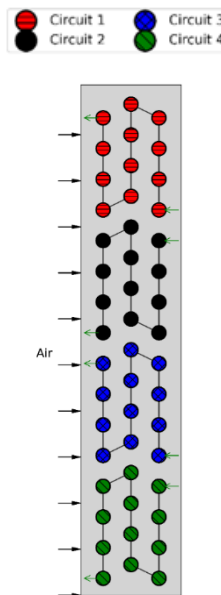
Figure 5.2. Tested heat exchanger coil with four circuits and seventy-two tubes

Table 5.1. Geometrical parameters of tested heat exchanger coil

No. of circuits	4
No. of rows	3
No. of tubes per row	16
No. of tubes per circuit	12
Tube type	Smooth
Tube material	Copper
Tube wall thickness	$0.51 \cdot 10^{-3}$ m
Tube outer diameter	$9.53 \cdot 10^{-3}$ m
Tube longitudinal spacing	$2.19 \cdot 10^{-2}$ m
Tube traverse spacing	$2.54 \cdot 10^{-2}$ m
Tube length	0.593 m
Fin type	Wavy
Fin thickness	$1.14 \cdot 10^{-4}$ m
Fins spacing	$1.57 \cdot 10^{-3}$ m
Half wavelength of fin wave	$5.51 \cdot 10^{-3}$ m
Wave amplitude	$2.1 \cdot 10^{-3}$ m

5.2.2 Test matrix

A full factorial design of experiments approach was used to develop the experimental test plan, as described in Chapter 2. Refrigerant side capacity is the critical experimental outcome, and the following three parameters were chosen as design factors:

- Refrigerant SST,

- Overall refrigerant superheat (SH), and

- Air inlet velocity ($V_{a,i}$),

resulting in the final test matrix shown in Table 5.2. All tests listed in Table 5.2 are tested with a dry and wet coil operation with air inlet DB temperature and WB temperature corresponding to each mode shown in Table 5.3.

Table 5.2. Test matrix for each refrigerant; see Table 5.3 for air inlet temperatures

Refrigerant	Testing mode	Saturated suction temperature (SST)	Air inlet velocity $(V_{a,i})$	Test Superheat (SH)	# of tests
R410A (baseline)	Evaporator dry Evaporator wet	7.2°C (45°F) 10°C (50°F) 12.8°C (55°F)	1.2 m/s (240 fpm) 1.5 m/s (300 fpm) 2 m/s (400 fpm)	11.1 K (20 R)	18
R1234ze(E)					18
				Total # of experiments:	**36**

Table 5.3. Air inlet temperatures for testing

Mode	Dry bulb temperature	Wet-bulb temperature
Evaporator dry	26.67°C (80°F)	14.44°C (58°F)
Evaporator wet	26.67°C (80°F)	19.44°C (67°F)

5.2.3 Data reduction

In addition to the overall refrigerant side capacity, $\dot{Q}_{ref}$, and air side capacity, $\dot{Q}_{air}$, bulk superheat, $T_{sup,bulk}$, and overall average superheat, $T_{sup,avg}$, are given as

$$T_{sup,bulk} = T_{r,out,bulk} - SST \text{, and} \tag{5.1}$$

$$T_{sup,avg} = \frac{\sum_{i=1}^{N} T_{r,out,i}}{N} - SST, \tag{5.2}$$

Where $T_{r,out,bulk}$ is the refrigerant temperature at coil outlet, N is the number of active circuits, and $T_{r,out,i}$ is the refrigerant temperature at the exit of circuit number i.

For refrigerant side capacity, the enthalpy is calculated using REFPROP 9 (Lemmon *et. al.,* 2018), from measured temperatures and pressures at the coil inlet and outlet. To calculate the air side capacity, the enthalpy at inlet and outlet of the coil are required, along with the air mass flow rate. These enthalpies are calculated using CoolProp (Bell *et. al.,* 2014), from the measured air DB and WB temperatures. Details on the type, measurement range, and accuracy of all instrumentation required measure all the required parameters during the experiment are presented in detail in Chapter 2.

For every experiment, data is recorded at a sampling rate of 0.5 Hertz for of 20 minutes, once the following conditions are satisfied:

- The instantaneous refrigerant flow rate is within ±2% of the average flow rate, as per ASHRAE Standard 33 (2016),

- The average refrigerant and air side capacities are within ±5% of average of each other, to comply with the limits set in ASHRAE Standard 33 (2016), and

- The individual superheat of each active circuit is within ±1.5 K of the overall average superheat, and the overall average superheat is within ±0.5 K of bulk superheat.

The average of the refrigerant ($\dot{Q}_{ref}$) and air side ($\dot{Q}_{air}$) capacity is

$$\dot{Q}_{avg} = \frac{\dot{Q}_{ref} + \dot{Q}_{air}}{2}. \tag{5.3}$$

An example set of results is shown in Figure 5.3, and Figure 5.4 which show the time series data recorded for an experiment with R1234ze(E), for which the refrigerant and air side operational parameters are listed in Table 5.4.

Table 5.4. Operational parameters for a sample experiment shown in figures 5.3, and 5.4

Parameters	Target from Test Matrix	Results
Refrigerant SST	50°F (10°C)	49.2°F (9.6°C)
Refrigerant inlet pressure	Floating variables to allow control of superheat	49.5 psia (341.3 kPa)
Refrigerant mass flowrate		143 lbs./hr. (0.018 kg/s)
Air inlet DB temperature	80°F (26.7°C)	80°F (26.7°C)
Air inlet relative humidity	67°F (19.4°C)	67.1°F (19.5°C)
Air volumetric flow rate	463 CFM (0.219 m^3/s)	460 CFM (0.217 m^3/s)
Air inlet pressure	Uncontrolled variable	98,000 kPa
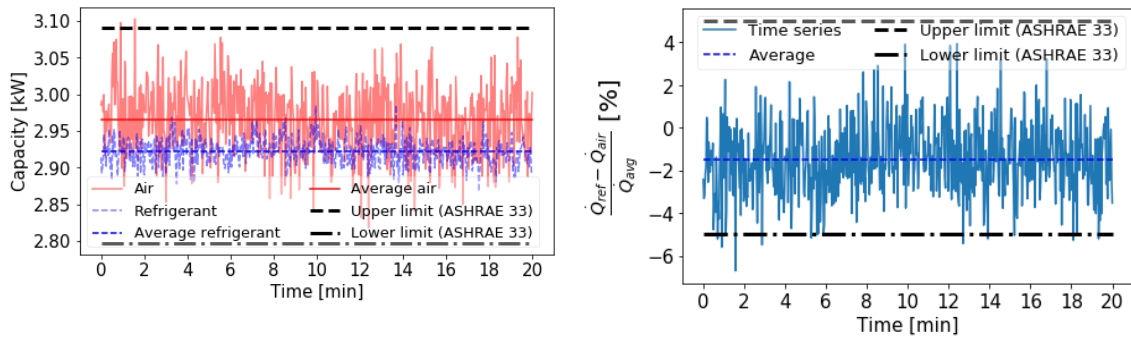
Figure 5.3. Energy balance on refrigerant and air side for an experiment with R1234ze(E), (1) Refrigerant and air side capacities, (2) Difference between air and refrigerant capacity expressed as a ratio to the average
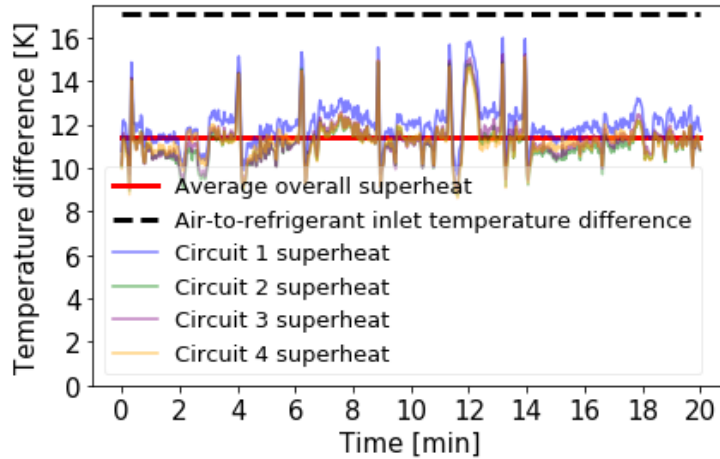
Figure 5.4. Individual circuit and overall average superheat results for an experiment

5.2 Results and discussion

5.3.1. Cross-fin (Xfin) heat exchanger model

The Xfin heat exchanger model (Sarfraz *et. al.,* 2019) was utilized to predict refrigerant capacity, then compared against experimental refrigerant capacities, collected using processes explained in Section 5.2. The model is a detailed segment-by-segment fin-and-tube heat exchanger model that not only accounts for refrigerant and moist air phase transitions, but also considers detailed input of the simulated heat exchanger's geometry, including circuitry information. In each segment, the refrigerant and air side heat transfers are evaluated by applying a lumped analysis using the ε-NTU method.

The Xfin model has the capability to evaluate how cross-fin conduction, or tube-to-tube conduction, impacts the capacity, of multi circuit fin-and-tube heat exchangers. Cross-fin conduction is

111

prevalent in heat exchangers with non-uniform tube wall temperatures. An extreme example of this is part load operation of commercial equipment heat exchangers, where refrigerant flows in some circuits only. The model allows the user to run simulations with cross-fin conduction enabled or disabled, to assess its effect on the model's capacity predictions.

The Xfin model features and capabilities can be leveraged to perform parametric studies, by modifying heat exchanger geometry and refrigerant circuitry, and observing how the coil performance changes at the same inlet refrigerant and airside conditions. Thus, the Xfin model is used as the primary modeling tool for this study. It has been thoroughly validated previously using R410A experimental data obtained from three distinct test heat exchangers in a previous work (Chapter 3), and is validated against R1234ze(E) in this analysis.

5.3.2. Model validation

All of the information in Table 5.1-5.3 was provided as inputs to the model, which then calculates outlet refrigerant superheat, refrigerant side pressure drop, and coil capacity. The model's correlations on refrigerant and air side are presented in Table 5.5. Since the majority of the heat transfer in the tested heat exchanger coil takes place in the two-phase region, it was critical to identify which correlations available in literature best predicted the behavior of the two fluids in this study. For this reason, different two-phase pressure drop correlations for R410A and R1234ze(E) were used for the simulations. As a point of reference, some major thermodynamic and transport properties of R410A, and R1234ze(E) calculated at 10°C using REFPROP 9 (Lemmon *et. al.,* 2018) are listed in Table 5.6. R410A is a blend made of equal parts of R32 and R125. The chemical name, formula, and structure of R32 and R125 are shown in Table 4.2, and for

R1234ze(E) are shown in Table 5.7.

Table 5.5. Correlations on refrigerant and air side used in Xfin model simulations

R410A & R1234ze(E) (Single-phase)	Heat transfer	Dittus Boelter equation (Winterton, 1998)
	Pressure drop	Blasius equation (Blasius, 1913)
R410A (Two-phase)	Heat transfer	Shah (1982)
	Pressure drop	Lockhart and Martinelli (1949)
R1234ze(E) (Two-phase)	Heat transfer	Shah (1982)
	Pressure drop	Friedel (1979)
Air	Heat transfer & pressure drop	Correlation for wavy fins (Wang *et. al.,* 1997)

Table 5.6. Key thermodynamic and transport properties of fluids in this analysis, at 10°C

Fluid	P_{sat} (kPa)	ρ_l (kg/m³)	ρ_v (kg/m³)	h_{fg} (kJ/kg)	μ_l (µPas)	μ_v (µPas)
R410A	1088.4	1128.5	41.9	208.6	142.8	12.8
R1234ze(E)	308.4	1210.4	16.5	177.6	238.2	11.6

Table 5.7. Chemical details of R1234ze(E)

Chemical name	3-tetrafluoropropene
Chemical formula	CF_3CHCHF
Chemical structure	

Figure 5.5 shows a parity plot comparing experimental and model predicted capacities for all experiments. A comparison of the experimental and model predicted refrigerant superheat is shown in Figure 5.6. The agreement between experimental and simulated capacity is quantified by the MAPE,

$$MAPE = \frac{|\dot{Q}_{evap,exp} - \dot{Q}_{evap,sim}|}{\dot{Q}_{evap,exp}} \cdot 100\%, \qquad\qquad (5.4)$$

where $\dot{Q}_{evap,exp}$, and $\dot{Q}_{evap,sim}$ are the experimental and model predicted refrigerant side capacities, respectively. For quantifying the agreement between the experimental and simulated superheat, the Mean Absolute Error (MAE) is used, given by,

$$MAE = |T_{sup,exp} - T_{sup,sim}|, \qquad\qquad (5.5)$$

where $T_{sup,exp}$, and $T_{sup,sim}$ are the experimental and model predicted refrigerant superheat, respectively.
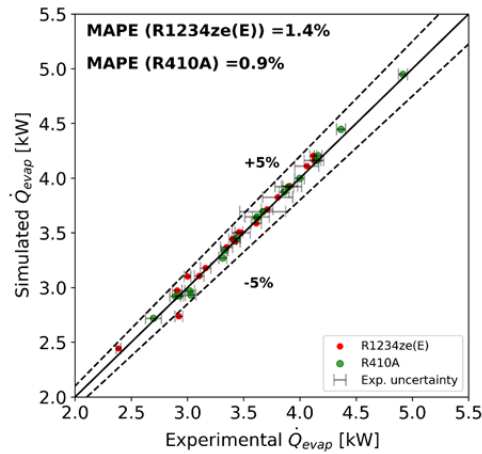
Figure 5.5. Experimental evaporator capacities versus model simulations

114
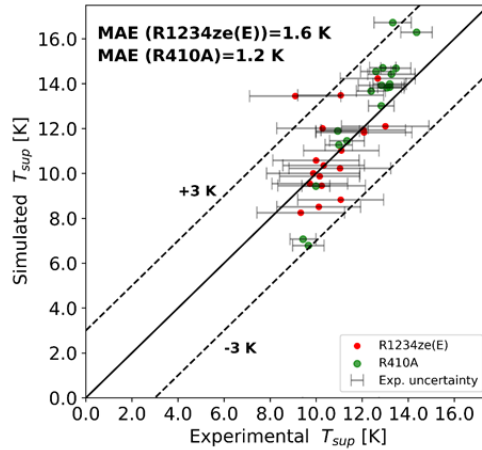
Figure 5.6. Experimental refrigerant superheat versus model simulations

The MAPE between experimental and model predicted coil capacity is 1.4% for R1234ze(E), while the MAE between experimental and model predicted superheat is 1.6 K. The above validation results provide confidence that any parametric simulation studies done with the Xfin model will have reasonable accuracy with both R410A and R1234ze(E). Another observation from the results, specifically from Figure 5.6, is that the experimental uncertainty for superheats with R1234ze(E) is higher than that of R410A. This is a result of the calculation of experimental superheat which is dependent on the refrigerant SST (see Equation(5.1). The SST is calculated by measuring the refrigerant saturation pressure by a pressure transducer with a fixed uncertainty of ±2.9 kPa and is therefore higher for the lower pressure R1234ze(E) compared with R410A. For the identical range of SSTs for R410A and R1234ze(E), the saturation pressures were in the range of 1002-1180 kPa, and 282-340 kPa respectively for both fluids.

5.3.3. Superheat iterative solver

To compare the performance of R1234ze(E) with R410A, an external iteration loop was written, that iterated on the inlet refrigerant mass flow rate until the outlet superheat converged to a set point from the user (within a tolerance of ±1 K). Refrigerant flow rate was the only variable iterated on to achieve the superheat set point, while keeping refrigerant SST and inlet pressure constant. Table 5.8 shows the computational test matrix for these simulations. Results of the simulations are shown in Figure 5.7.

Table 5.8. Computational test matrix for superheat iterative solver

Fluid	Simulation mode	Saturated suction temperature (SST)	Air inlet velocity ($V_{a,i}$)	Target Superheat (SH)	# of simulations
R410A	Evap. dry Evap. wet	7.2°C (45°F) 12.8°C (55°F)	1 m/s (200 fpm) 1.5 m/s (300 fpm) 2 m/s (400 fpm)	11.1 ±1 K (20 ±1.8 R)	12
R1234ze(E)					12
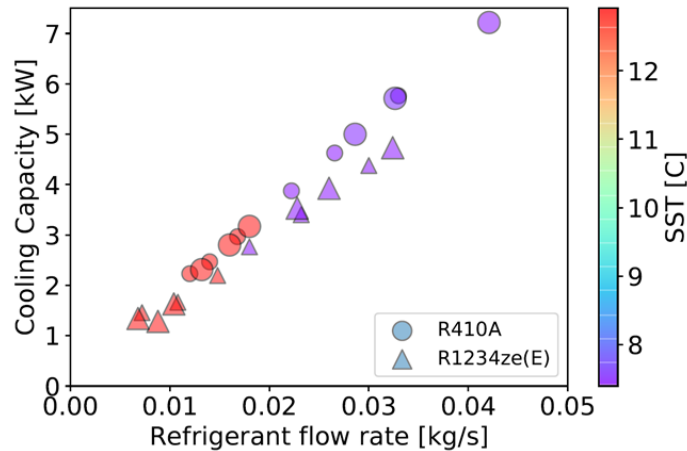
Figure 5.7. Variation of refrigerant flow rate and capacity to achieve constant superheat at constant SST

The latent heat of R1234ze(E) is lower than for R410A (Li *et. al.,* 2021). This study found that on average, to maintain the same superheat in this coil, the refrigerant flow rate required for R1234ze(E) was 26% lower than R410A, but also resulted in coil capacities that were lower by 34%. Additionally, it was found that the pressure drop for R1234ze(E), even with lower refrigerant flow rates, was 15 times that of R410A. This was expected, since the refrigerant side pressure drop is directly proportional to the liquid density and viscosity, which is higher for R1234ze(E), as seen in Table 5.6.

5.3.4 Fin density parametric study

The tested heat exchanger coil had a fin density of 15 FPI (see Table 5.1). Using feedback from industrial center members, a common upper limit of indoor evaporator coils fin density is 20 FPI. Thus, a parametric simulation study was performed by setting the fin density to 15 FPI, 18FPI, and 20 FPI, for the test conditions shown in Table 5.9.

Figure 5.8 shows how the fin density effects the heat exchanger coil capacity, at three different refrigerant flow rates. It also exhibits the relative difference between simulations done in dry (relative humidity of 25%) and wet (relative humidity 50%). To have a single metric that encapsulates the performance of the simulated heat exchanger, the term $\dot{Q}/\Delta P$ was defined, which is a ratio of predicted coil capacity ($\dot{Q}$) to refrigerant side pressure drop (ΔP). Table 5.10 shows the average capacity, superheat, refrigerant side pressure drop, and $\dot{Q}/\Delta P$ for the afore mentioned parametric fin density study.

Table 5.9. Computational test matrix for fin density parametric analysis

Fluid	Simulation mode	Saturated suction temperature (SST)	Air inlet velocity ($V_{a,i}$)	Fin density	# of simulations
R1234ze(E)	Evap. dry Evap. wet	7.22°C (45°F)	1 m/s (200 fpm)	15 FPI	6
			1.5 m/s (300 fpm)	18 FPI	6
			2 m/s (400 fpm)	20 FPI	6
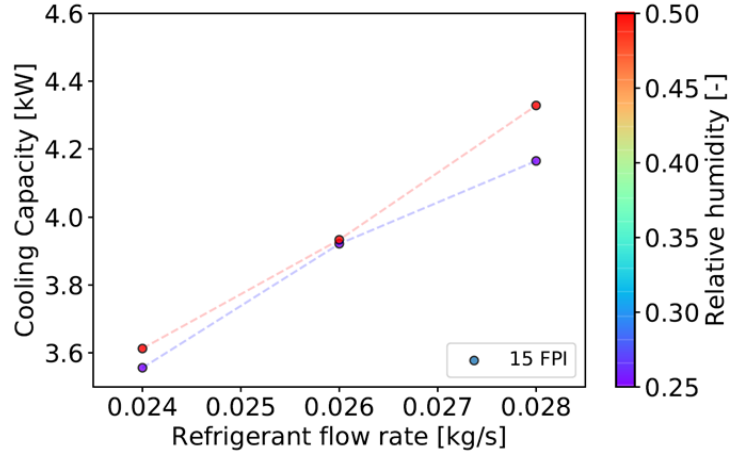
a) Variation of capacity with fin density of 15 FPI
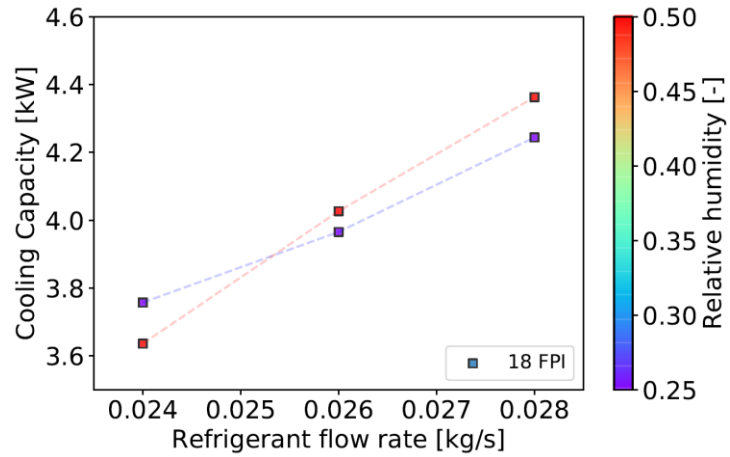
b) Variation of capacity with fin density of 18 FPI

118
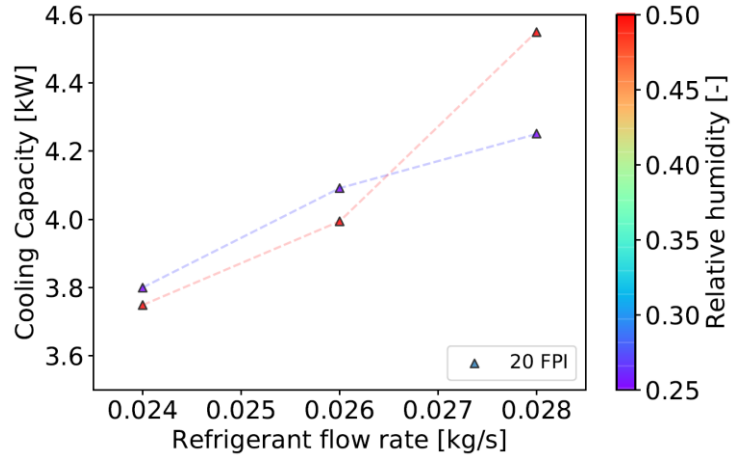
c) Variation of capacity with fin density of 20 FPI

Figure 5.8. Simulated R1234ze(E) heat exchanger capacity as a function of refrigerant flow rate for fin densities of a) 15 FPI, b) 18 FPI, and c) 20 FPI

Table 5.10. Average values of simulated heat exchanger performance as a function of fin density with R1234ze(E)

	15 FPI (baseline)	18 FPI	20 FPI
Capacity ($\dot{Q}$, kW)	3.9	4.0	4.1
Superheat (K)	10.0	9.9	9.5
Refrigerant pressure drop ($\varDelta P$, kPa)	8.9	8.6	8.5
$\dot{Q}/\varDelta P$, kW/kPa	0.44	0.47	0.48

From Figure 5.8, it is evident that with increasing fin density, the heat exchanger capacity increases with the increase being more pronounced at higher refrigerant flow rates. Additionally, Table 5.10 shows that on average, the refrigerant side pressure drop goes down with increasing fin density, resulting in an increase in the value of $\dot{Q}/P$. Thus, it can be concluded that increasing fin density for a block circuited heat exchanger coil would increase performance and can be hence employed to get optimum or near optimum performance with low-GWP replacements, while keeping all operational parameters identical.

5.3.5 Refrigerant circuitry optimization

To make an informed decision about evaluating refrigerant circuitries that would give the best heat exchanger performance, the Xfin model was used in conjunction with the Intelligent System for Heat Exchanger Design (ISHED) module. ISHED comes bundled with EVAP-COND (Domanski *et. al.,* 2016), a tube-by-tube fin-and-tube heat exchanger model, available in the public domain. For any given set of inlet conditions, ISHED optimizes the refrigerant circuitry to achieve the maximum possible capacity. Table 5.11 shows the operating conditions which were provided as input to ISHED. The goal was to see how it would optimize the original 4 block circuits of the test heat exchanger coil into a minimum of 2 and maximum of 6 circuits, to achieve maximum capacity. Table 5.12 shows the major input control parameters and constraints provided to ISHED for the optimization runs, for the operational parameters shown in Table 5.11.

Table 5.11. Operational parameters for circuitry optimization in ISHED

Refrigerant	R1234ze(E)
Refrigerant SST	7.2°C (45°F)
Refrigerant inlet pressure	282 kPa (40.9 psia)
Refrigerant inlet quality	0.305
Refrigerant mass flowrate	0.037 kg/s (294 lbs./hr.)
Air inlet DB temperature	26.7°C (80°F)
Air inlet relative humidity	0.25
Air volumetric flow rate	0.36 m^3/s (766 CFM)
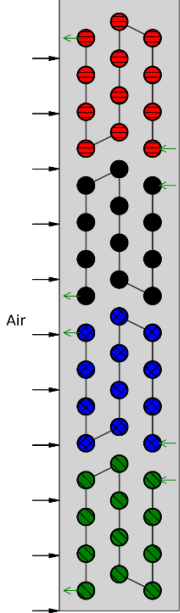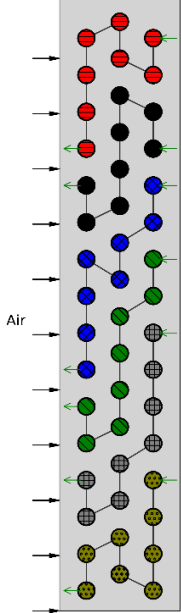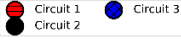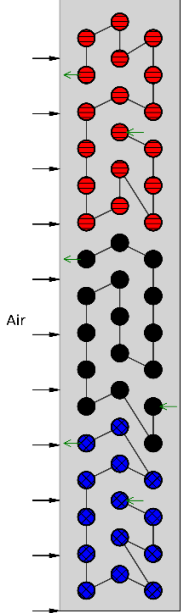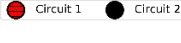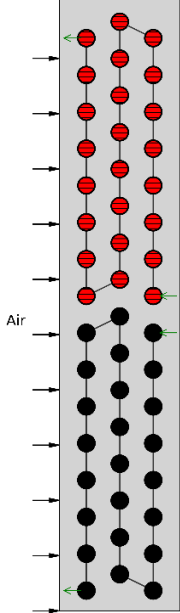
Table 5.12. Key design rules and constraints provided to ISHED for circuitry optimization

Minimum number of inlets	2
Maximum number of inlets	6
Maximum number of tubes fed from single tube*	1
Connections to all inlet tubes and from all exit tubes must be on same side of heat exchanger	Yes

*To ensure that there is no splitting of circuits

The optimization in ISHED produced several circuitries from which the best two were chosen, and were input to the Xfin model, in addition to a 2-circuit design with block circuitry. The 2-circuit design was made part of the test matrix to observe how an un-optimized design would affect the heat exchanger performance. Table 5.13 shows the results of the Xfin simulations, when run with the operational parameters in Table 5.11, for each circuitry design.

Table 5.13. Simulated heat exchanger performance in Xfin model with original and optimized refrigerant circuitries; see Table 5.10 for operational parameters

Circuitry	Baseline	ISHED #1	ISHED #2	Manual input
Capacity ($\dot{Q}$, kW)	5.57	5.43	5.52	5.88
Superheat (K)	13.9	10.3	11.7	16.8
Refrigerant pressure drop (ΔP, kPa)	15.6	5.9	33.8	116
$\dot{Q}/\Delta P$, kW/kPa	0.36	0.91	0.16	0.05

The 6-circuit optimized design has a 2.5% lower capacity, and 3.6 K lower superheat, in comparison to the original design, but also has significantly lower pressure drop. This is because even though the amount of heat transfer area is the same, the refrigerant flow per circuit is lower for 6 circuits compared to 4 circuits, and therefore the pressure drop is lower. The lower pressure drop can also be accounted to the circuitry pattern, which is made in a way that majority of the tubes have an equal number of first order, i.e., directly adjacent neighboring tubes that have single phase, and two-phase refrigerant in them. For this design, the $\dot{Q}/\Delta P$ came out to be 0.91, which is more than 2.5 times that of the original (baseline) circuitry of the tested heat exchanger.

For the 3-circuit design, it was observed that the capacity and superheat are lower than the original design. This is because the inlet for 2 out of 3 circuits is in the middle row of the heat exchanger, a location where the air temperature exiting the tube is not the coldest, and hence the refrigerant capacity in those locations is not utilized to its fullest. However, it appears that this circuitry design is a compromise to achieve a balance between optimum refrigerant side capacity, and pressure drop. The $\dot{Q}/\Delta P$ was calculated to be 0.16, 56% lower than the baseline circuitry.

Finally, the un-optimized circuitry design led to an increase in capacity of 5.6% more than the original design, but at the expense of pressure drop that was more than 7 times of the original. Despite this high pressure drop causing a drop in refrigerant saturation temperature, this circuitry showed the highest superheat, which is owing to the larger number of passes per circuit, and higher heat transfer area per circuit, when compared to all other circuitry designs. However, the $\dot{Q}/\Delta P$ was only 0.05, making it the poorest design amongst all others. Thus, this illustrates that for refrigerant circuitry modifications, some intuition and artistry may still be required.

5.4 Conclusions

This paper presents the influence of fin density and refrigerant circuitry on coil capacity and refrigerant side pressure drop, of a fin-and-tube heat exchanger with R1234ze(E) as the refrigerant. A four-circuit heat exchanger coil was tested with R410A and R1234ze(E) in evaporator mode. A total of 36 experiments were done with the two fluids, covering a wide range of inlet refrigerant and air side conditions.

Experimental results were compared against capacities predicted by a discretized fin-and-tube heat exchanger model, called cross-fin (Xfin). For R410A, the MAPE between experimental and simulated coil capacity was 0.9%, and the MAE between experimental and simulated superheat was 1.2 K. For R1234ze(E), the MAPE between experimental and simulated coil capacity was 1.4%, and the MAE between experimental and simulated superheat was 1.6 K. Simulations were then done with R410A and R1234ze(E), with a fixed superheat as input to the model, where the fin density of the coil was varied from 15 to 20 FPI. Additionally, R1234ze(E) was simulated for a fixed set of operational parameters with several optimized, and one un-optimized refrigerant circuit design.

Key results obtained in this study are:

- The Xfin model can predict coil performance with reasonable accuracy with R410A, and R1234ze(E),

- For identical superheat and refrigerant SST, the refrigerant flow rate required for R1234ze(E) was 26% lower than R410A, resulting in 34% lower coil capacities, and 15 times higher refrigerant pressure drop,

- An increase in fin density of 33.3% lead to an increase in capacity of 5.1%, and a reduction in pressure drop of 4.5%,

- For the circuitry which gave a 5.6% increase in capacity compared to the baseline, the refrigerant side pressure drop increased by 7.5 times, whereas the circuitry which gave a 2.5% decrease in capacity (compared to baseline), gave a pressure drop that was 38% lower than the baseline

5.5 Future Work

This work was limited to only one indoor evaporator coil size to maintain compatibility with existing equipment cabinet designs. The only varied parameter was fin density and refrigerant circuitry. Future work will focus on modifying several other parameters, including, but not limited to, type of fin, tube length, and tube diameter, and other coil sizes will be simulated as well, along with a wider variety of refrigerant circuitries.

In addition to geometry, only a single low-GWP working fluid was studied in this work. Future work will focus on simulating other fluids, namely R1234yf, R454A, R454B, and R454C. Analysis of the results of parametric simulations with various designs, refrigerant circuitries, and refrigerants, will be conducted with the objective of developing a set of guidelines for fin-and-tube heat exchanger manufacturers for pseudo-optimal redesign of their future equipment, so that low-GWP fluids can achieve performance similar to or better than the R410A baseline.

CHAPTER VI

DEVELOPMENT OF GUIDELINES FOR THE DESIGN OF FIN-AND-TUBE HEAT EXCHANGERS WITH LOW-GWP REFRIGERANTS

ABSTRACT

Regulatory changes worldwide, aimed at combating climate change, are requiring air conditioning (AC) and heat pump (HP) equipment manufacturers to switch refrigerants to alternatives with reduced global warming potential (GWP). The design of Fin-and-tube Heat Exchangers (FTHX) is critical to the overall performance of this equipment and is not currently well understood with low-GWP working fluids. This paper presents a simulation study exploring the impact of design changes for a FTHX used in an indoor residential evaporator originally designed for R410A. HFO refrigerants R1234yf and R1234ze(E) were considered as the ultra-low-GWP replacements, evaluated using the cooling capacity, refrigerant-side pressure drop, and the ratio of the two. When evaluated at the same operational conditions, with a fixed refrigerant outlet superheat, it was found that for a fixed slab size, the FTHX was most sensitive to the number of circuits, followed by the tube diameter, number of tubes in the FTHX, and the fin density. For the low-GWP HFOs, modification of circuitries led to a maximum increase in FTHX capacity of 20%, and a maximum decrease in refrigerant side pressure drop of 88.6%. Based on the simulation results, two

customized FTHX designs were suggested, with different changes to the FTHX slab size. One design prioritized increased FTHX capacity, and the other prioritized reduction in refrigerant pressure drop. These designs demonstrated that, with HFO's, it will be challenging to achieve both the same capacity and pressure drop characteristics as R410A without modifications to FTHX size.

This chapter is a paper submitted for publication in the International Journal of Refrigeration.

6.1 Introduction and Objectives

A rise in living standards globally has resulted in an increased use of space cooling systems, which has caused an increase in emissions from these systems that contribute to climate change, due to the greenhouse gas (GHG) emissions from these systems. The total CO_2 equivalent emissions produced by the Heating, Ventilation, Air Conditioning and Refrigeration (HVAC&R) accounts for 7.8% of global GHG emissions (Cuolomb *et. al.,* 2017). These emissions can be categorized into:

- Direct Emissions that are generated due to leakage or uncontrolled disposal of refrigerants from refrigeration systems, primarily chlorofluorocarbons (CFCs), hydrofluorocarbons (HCFCs), and hydrofluorocarbons (HFCs), and

- Indirect Emissions from GHGs produced when energy is generated that is used to manufacture, operate, dispose and recycle these systems

Regulatory measures worldwide are supporting the transition of fluorinated refrigerants to alternatives with lower global warming potential (GWP) such as the F-gas Regulations (Schulz & Kourkoulas, 2014), the Kigali amendment to the Montreal Protocol (UNEP, 2016), and recently,

a rule proposed by the US American Innovation and Manufacturing Act (AIM, 2021). As an example, the F-gas regulations (Schulz & Kourkoulas, 2014) have set a GWP limit of 750 for single split AC systems in the European Union (EU). R410A has a GWP of 2088 (Intergovernmental Panel on Climate Change, 2014), exceeding the F-gas regulation limits. It is currently one of the most common HFCs used in residential and light commercial systems, and its phase out will require substantial redesign efforts.

Some core criteria that long term low-GWP alternative refrigerants have to fulfil are equivalent or higher volumetric cooling capacity, similar or improved energy efficiency, and lower flammability. Additionally, although a GWP of 750 is the limit set for split systems in the EU, automotive ACs already have an upper GWP limit of 150 (Schulz & Kourkoulas, 2014). The authors anticipate that GWP restrictions for current R410A based systems may fall at or below a GWP limit of 150. Substantial research effort has been expended to find short term low-GWP alternatives to R410A (Sethi & Motta, 2016, Devecioğlu, 2017, Pardo & Mondot, 2018,, Sieres *et. al.,* 2021), but none of the alternatives fulfill majority of the outlined criteria above, implying that there is a need to investigate viable, long term low-GWP alternatives.

Over the past few years, HFOs have emerged as a popular replacement option for current HFCs. Some of the most popular HFOs are R1234yf, and R1234ze(E) (see e.g. Mota-Babiloni *et. al.,* 2014, Sánchez *et. al.*, 2017, Bobbo *et. al.,* 2018). Since both these HFOs have smaller volumetric capacities and latent heats compared to R410A, they were considered as "drop-in" replacements mostly for R134a based systems (see e.g. Mota-Babiloni *et. al.,* 2014, Fukuda *et. al.* 2014, Rajendran *et. al.,* 2019). There are several reasons why R1234yf and R1234ze(E) should be considered as long-term low-GWP replacements in all residential and light commercial

applications, including:

- R1234ze(E) does not form flammable mixtures under 30°C (Mota-Babiloni *et. al.,* 2016), and can be thus considered non-flammable for storage and handling purposes in many climates. Additionally, R1234ze(E) and R1234yf have substantially lower flammability than hydrocarbons used in domestic refrigerants such as R290 and R600a, but with similar GWPs, implying that they can be easily used in systems with low refrigerant charge,

- Both refrigerants have demonstrated good miscibility characteristics with commonly used Polyolester (POE) compressor oils (Jia, *et. al.,* 2020), which are compatible with conventional HFCs like R134a, and R410A, and

- R1234yf and R1234ze(E) have ultra-low-GWPs of 4 and 7 respectively (Intergovernmental Panel on Climate Change, 2014), supporting ambitious goals of reductions in GWP emissions.

To have optimum heat exchanger performance with R1234ze(E) and R1234yf, it is critical that current FTHX designs will have to be modified to accommodate them effectively. Some major FTHX geometrical parameters that can be modified to achieve enhanced performance are the circuitry, fin density, and tube diameter. Li *et. al.* (2021) simultaneously optimized heat exchanger circuitry and refrigerant composition of mixtures consisting of R32, R125, and R1234yf to maximize Energy Efficiency Ratio (EER) and minimum flammability. The rationale for these three particular components was R32's high latent heat, R125`s common use to suppress flammability, and R1234yf's low-GWP. Circuitry optimization included selection of counterflow, mixed flow, and a parallel flow pattern with the goal of minimizing FTHX cost. The optimization refrigerant

mixture had a GWP of 286, with the optimized FTHX design's cycle efficiency improved by 5.9%, and a reduction in flammability of 48.6%. Sadeghianjahromi & Wang (2021) found that changes in fin density are known to improve heat transfer in heat exchangers with wavy fins, but at the expense of increased air side pressure drop. Finally, Xie *et. al.,* (2009) showed using simulations that out of the various fin-and-tube heat exchanger FTHX geometrical parameters such as tube diameter, number of tube rows, longitudinal fin pitch, and transversal tube pitch, the influence of change in tube diameter on the heat transfer and pressure drop in the FTHXs is greater than that of tube pitch.

For air source equipment, performance comparisons in literature for HFOs R1234yf, and R1234ze(E), or HFO/HFC blends have mostly been at system level and not at the heat exchanger level (e.g. Devecioğlu, 2017, Li *et. al.*, 2021b, Yu *et. al.*, 2021). System level studies tend to prioritize gains in system efficiency, such as Energy Efficiency Ratio (EER), and COP, rather than investigating in detail how the performance of the heat exchanger FTHX, such as capacity and refrigerant side pressured drop, may be improved.

A segment-by-segment heat exchanger model (Xfin) was originally developed by Sarfraz, *et. al.* (2019), and was previously validated with R410A by Sarfraz *et. al.,* (2020) and, Saleem *et. al.* (2021a) (Chapter 3). Saleem *et. al.* (2021b), in Chapter 5, validated Xfin, with R1234ze(E) as the working fluid in a multi circuit evaporator FTHX with 4 circuits, using a custom heat exchanger facility (detailed in Chapter 2). Simulations were completed with R1234ze(E) in evaporator mode and with dry as well as wet air inlet conditions, by altering the fin density to see the impact of these parameters on the heat exchanger performance, primarily the capacity, and refrigerant side pressure drop. Across the computational test matrix, it was found that increasing the fin density from 15 fins per inch (FPI) to 20 FPI increased capacity by 5.1% and decreased refrigerant side pressure drop by 4.5%.

Additional simulations were completed by altering the refrigerant circuitry. It was found that increasing capacity for the same inlet refrigerant and airside conditions simultaneously increases refrigerant side pressure drop. Consequently, a circuitry that gave a reduced refrigerant side pressure drop resulted in reduced FTHX capacity. The previous study was limited to R1234ze(E) as the low-GWP fluid, and only altered the circuitry and fin density of the simulated FTHX. Additionally, the parametric studies with altered geometries were using identical mass flow rates for R410A and R1234ze(E), opposed to maintaining the same refrigerant exit superheat.

This paper continues the work from Chapter 5 and compares the performance of R1234yf and R1234ze(E) for a fin-and-tube heat exchanger that was developed or R410A using Xfin. Fin density, circuitry, tube diameter, number of tubes, number of tube rows, and tube length were independently modified as part of a parametric analysis of this heat exchanger. The simulations aim to find a FTHX design for pure A2L Ultra-low-GWP HFOs as refrigerants that provides a capacity that is the same or greater than R410A for the baseline FTHX and has acceptable refrigerant side pressure drop.

6.2 Methodology

6.2.1 Heat exchanger model

Numerical simulations in this work are executed using the validated Xfin model (Sarfraz, *et. al.* 2019, Sarfraz *et. al.,* 2020 and, Saleem *et. al.* 2021a in Chapter 3). The model takes into consideration not only refrigerant and moist air phase transitions, but also detailed input of the simulated heat exchanger's geometry, including circuitry details. The refrigerant and air side heat transfers are calculated in each segment using the ε-NTU approach. Xfin has been validated with

single-phase, as well as two-phase refrigerant data, using multi-circuit fin-and-tube heat exchanger FTHXs of different sizes, number of tubes, circuitry arrangement and full and part-load operation. Table 6.1 summarizes these validation efforts for experiments that were carried out at full load. The Mean Absolute Percent Error (MAPE) between the model predicted capacities and experiments are listed. Note that the heat exchanger tested with R1234ze(E) in Saleem *et. al.* (2021b) (Chapter 5) had previously been tested with R410A in Saleem *et. al.* (2021a) (Chapter 4). The MAPE values suggest that the Xfin model is a reliable modelling tool for evaluating the effect of heat exchanger geometry changes onto performance.

Table 6.1. Summary of Xfin model validation in cooling mode operating at full load

Fluid	Mode	Citation	Number of heat exchanger(s) tested	MAPE between experimental and model-predicted capacities	Number of experiments
Water	Single-phase	Sarfraz, *et. al.* (2019)	1	2.1%	3
R410A	Two-phase	Sarfraz *et. al.,* (2020)	1	0.7%	3
R410A	Two-phase	Saleem *et. al.* (2021a)	3	1.0%, 2.4%, & 0.9%*	66
R1234ze(E)	Two-phase	Saleem *et. al.* (2021b)	1	1.4%	18

The values are for the three tested FTHXs, which had two distinct sizes, and three distinct refrigerant circuitries

6.2.2 Simulated heat exchanger details

The FTHX used as the baseline design was originally designed as an indoor evaporator FTHX with R410A. It has a R410A capacity of approximately 5.5 kW (1.6 ton) at saturated suction temperature (SST) of 10°C (50°F), superheat of 7.2 K (13 R), and refrigerant mass flow rate of 0.032 kg/s (250

lbs./hr.). It was tested with R410A and R1234ze(E) for validating the Xfin model, with MAPE between experimental and simulated capacities being 0.9%, and 1.4% respectively (in Chapter 5). The schematic and specifications of the baseline FTHX are shown in Figure 6.1 and Table 6.2, respectively.
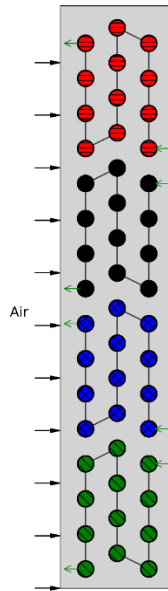
Figure 6.1. Schematic of baseline simulated heat exchanger with four circuits

Table 6.2. Geometrical parameters of baseline simulated heat exchanger

No. of circuits	4
No. of rows	3
No. of tubes per row	16
No. of passes per circuit	12
Tube type	Smooth
Tube material	Copper
Tube wall thickness	$0.51 \cdot 10^{-3}$ m
Tube outer diameter	$9.53 \cdot 10^{-3}$ m
Tube traverse spacing	$2.54 \cdot 10^{-2}$ m
Tube longitudinal spacing	$2.19 \cdot 10^{-2}$ m
Tube length	0.495 m
Fin type	Wavy
Fin thickness	$1.14 \cdot 10^{-4}$ m
Fin spacing	$1.57 \cdot 10^{-3}$ m
Half wavelength of fin wave	$5.51 \cdot 10^{-3}$ m
Wave amplitude	$2.1 \cdot 10^{-3}$ m

6.2.3 Working fluid selection

As stated in Section 6.1, R1234yf and R1234ze(E) were chosen as the low-GWP alternatives for simulation in this analysis. Their key properties are listed in Table 6.3, along with that of R410A as the baseline. All thermodynamic and transport properties shown in Table 6.3 were calculated at a saturation temperature of 7.2°C (45°F) with REFPROP 9 (Lemmon *et. al.*, 2018).

Table 6.3. Some properties of fluids in this analysis, evaluated at 7.2°C (45°F)

Fluid	GWP	P_{sat} (kPa)	ρ_l (kg/m^3)	ρ_v (kg/m^3)	h_{fg} (kJ/kg)	μ_l (μPas)	μ_v (μPas)
R1234yf	4	400.6	1154	22.3	158.5	188.6	10.6
R1234ze(E)	7	282.2	1219	15.3	179.4	239.2	11.2
R410A	2088	1002	1140	38.5	212.3	151.9	11.8

In the later sections, refrigerants R1234yf and R1234ze(E) will be collectively addressed as HFOs in the context of simulations, unless otherwise stated.

6.2.4 Computational test matrix

For all analysis, the air side inlet conditions were kept constant and refrigerant saturated suction temperature and superheat of 5 K ±1 K. A tolerance is required because Xfin is formulated with refrigerant mass flow rate as an input with superheat as an output (Sarfraz, *et. al.,* 2019). This work introduced a root finding algorithm to allow the user to select a refrigerant exit superheat by varying the refrigerant flow rate. The basis for a fixed superheat is to be able to identify design changes for a FTHX in a vapor compression system where the compressor suction superheat must be 5 K, regardless if the fluid is R410A, or one of the HFOs.

Refrigerant and air side operational parameters for the simulations are shown in Table 6.4. The inlet refrigerant pressures for each fluid are the corresponding saturation pressures in Table 6.3, since the refrigerant enters the simulated FTHX as two-phase.

Table 6.4. Refrigerant and air side operational parameters for all parametric simulations for the different fluids

Parameters	Value for each fluid		
	R410A	R1234yf	R1234ze(E)
Refrigerant inlet SST	7.2°C (45°F)		
Refrigerant inlet quality	20%		
Refrigerant mass flowrate	Floats to achieve target superheat		
Refrigerant subcooling before EXV	10 K (18 R)		
Refrigerant liquid line temperature before EXV	37.8°C (100°F)		
Target refrigerant superheat	(5 ± 1) K $[(9\pm1.8)$ R]		
Air inlet DB temperature	26.7°C (80°F)		
Air inlet WB temperature	19.4°C (67°F)		
Air volumetric flow rate	0.36 m^3/s (763 CFM)		
Air inlet pressure	98 kPa (14.2 psia)		

The correlations for each fluid used in the Xfin model are shown in Table 6.5. Because the two-phase region accounts for the majority of heat transfer in the simulated FTHX, it was critical to determine which correlations in literature best predicted the behavior of all the fluids in the study. As a result, for the simulations, different two-phase pressure drop correlations are used for each of the fluids.

Table 6.5. List of refrigerant and airside correlations used in the simulation model

Fluid	Correlation type	Reference
R410A, R1234ze(E) & R1234yf (Single-phase)	Heat transfer	Dittus Boelter equation (Winterton, 1998)
	Pressure drop	Blasius equation (Blasius, 1913)
R410A (Two-phase)	Heat transfer	Shah (1982)
	Pressure drop	Lockhart and Martinelli (1949)
R1234yf (Two-phase)	Heat transfer	Wattelet (1994)
	Pressure drop	Friedel (1979)
R1234ze(E) (Two-phase)	Heat transfer	Shah (1982)
	Pressure drop	Friedel (1979)
Air	Heat transfer & pressure drop	Correlation for wavy fins (Wang *et. al.,* 1997)

The goal of the simulation parametric study is to develop a heat exchanger FTHX design that:

- Provides a FTHX capacity with HFOs that is similar to that of R410A, and

- Exhibits a refrigerant side saturation temperature drop that is the same as R410A.

In order to calculate the optimum refrigerant pressure drop for the HFOs, refrigerant pressure drop data for R410A was collected from our industrial collaborators, and was converted into an equivalent drop in SST. This SST drop was then used to calculate the corresponding refrigerant side pressure drop for the HFOs, shown in Table 6.6.

Table 6.6. Acceptable refrigerant pressure drops for fluids simulated in this analysis, along with the corresponding drop in SST

Fluid	R410A	R1234yf	R1234ze(E)
SST drop	(0.9$\pm$0.3) K		
Refrigerant pressure drop	(31.0$\pm$8.6) kPa	(11.8$\pm$3.7) kPa	(9.0$\pm$2.8) kPa

6.2.5 Geometrical parameters adjusted

For evaluating the effect of heat exchanger geometry, the following parameters are initially varied:

- Fin density,

- Refrigerant circuitry, and

- Tube diameter.

The above parameters were specifically chosen because their modification does not involve changing the size of the evaporator FTHX's fin sheet, together with retaining the same face area. Based on simulation results, changes in FTHX slab will be recommended, to achieve increased capacity, and/or reduced refrigerant side pressure drop.

The baseline FTHX configuration has a fin density of 15 FPI; the parametric study additionally included 18 FPI and 20. The maximum fin density value of 20 FPI for indoor evaporator FTHXs was informed by our industrial collaborators as a typical upper limit to minimize air-side pressure drop. Simulations for the different fin densities considered R410A, as well as R1234yf and R1234ze(E). For the circuitry modifications, it was decided to change only the number of total circuits in the FTHX, without altering the overall refrigerant path significantly. The original baseline FTHX design, shown in Figure 6.1, has four circuits in a block configuration. Hence, for the parametric study, the same type of block configuration was used with three, six, and eight circuits.

Figure 6.2 shows the schematics of the simulated circuities, including the baseline configuration.
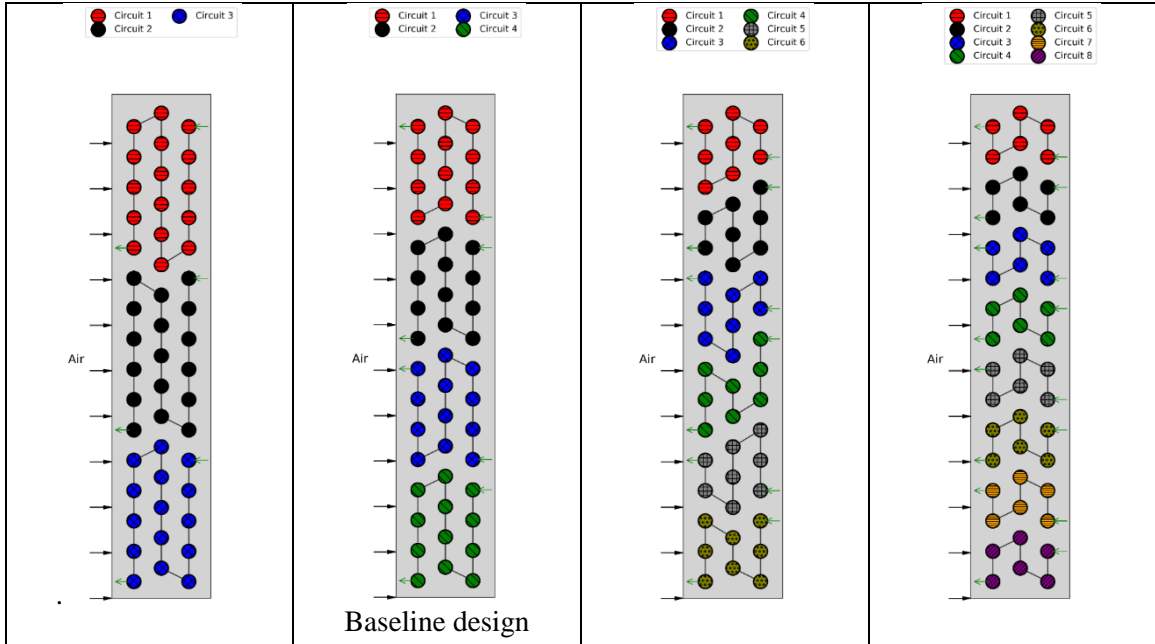
Figure 6.2. Block circuitry designs for simulated fin tube heat exchanger

The approach utilized for the parametric study of tube diameters was to add to the number of circuits, tube rows, and tubes in the FTHX while simultaneously reducing the tube diameter. This approach then maintains similar inlet velocity at each circuit, for identical refrigerant flow rates. Table 6.7 shows the circuitry of the FTHXs simulated with different tube diameters, along with the corresponding number of tubes and circuits. Transversal and longitudinal tube pitches were modified to ensure that the FTHX designs with the modified tube diameters would be accommodated in the existing slab size. Table 6.8 illustrates that for the different FTHX designs with the different tube diameters, the inlet refrigerant velocities did not vary more than 3.3% from each other, for an identical refrigerant mass flow rate.

Table 6.7. Circuitry and tube count for the FTHXs simulated with various tube diameters
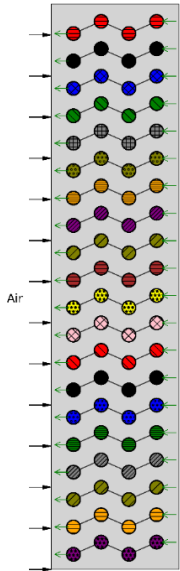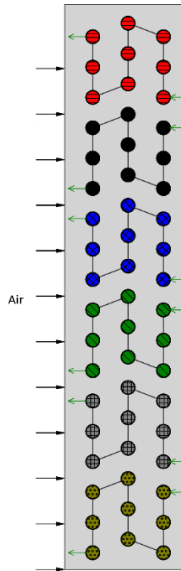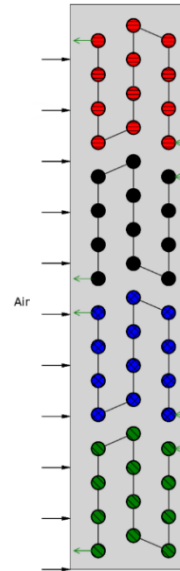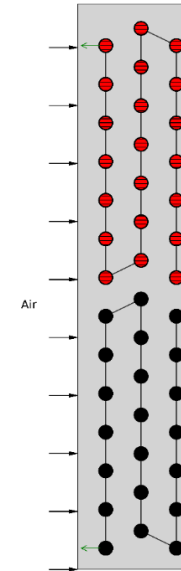
Circuitry design				
Tube outer diameter	4.76 mm	7.94 mm	9.53 mm (baseline)	12.7 mm
Total # of tubes	80	54	48	42
# of circuits	20	6	4	2

Table 6.8. Calculation of refrigerant velocity at inlet for various FTHX designs simulated for an example refrigerant flow rate

Tube outer diameter	# of circuits	# of passes per circuit	Fluid	Total refrigerant mass flow rate (kg/s)	Refrigerant mass flow rate per circuit (kg/s)	Refrigerant inlet velocity per circuit (m/s)
9.53 mm (3/8")*	4	12	R410A		0.0116	1.17
4.76 mm (3/16")	20	4			0.00235	1.28
7.94 mm (5/16")	6	9			0.00783	1.27
9.53 mm (3/8")	4	12	R1234yf		0.0116	1.26
12.7 mm (1/2")	2	21		0.0465	0.0233	1.32
4.76 mm (3/16")	20	4			0.00235	2.83
7.94 mm (5/16")	6	9			0.00783	2.76
9.53 mm (3/8")	4	12	R1234ze(E)		0.0116	2.74
12.7 mm (1/2")	2	21			0.0233	2.86

*baseline design

6.3 Results and Discussions

6.3.1 Effects of changes in nominal fin density

Figure 6.3 shows the simulated heat exchanger FTHX capacity, and refrigerant SST drop as a function of fin density. The term, QP, was defined was defined as a metric that encapsulates the performance of the simulated heat exchanger FTHX, and is given as,

$$QP = \dot{Q}_{evap} / \Delta P_{ref} \tag{6.1}$$

Where $\dot{Q}_{evap}$ is the simulated FTHX capacity, and ΔP_{ref} is the simulated refrigerant side pressure drop. Figure 6.3 additionally shows simulated capacity, SST drop and QP at each fin density normalized against the respective value for each refrigerant at the baseline (15 FPI).
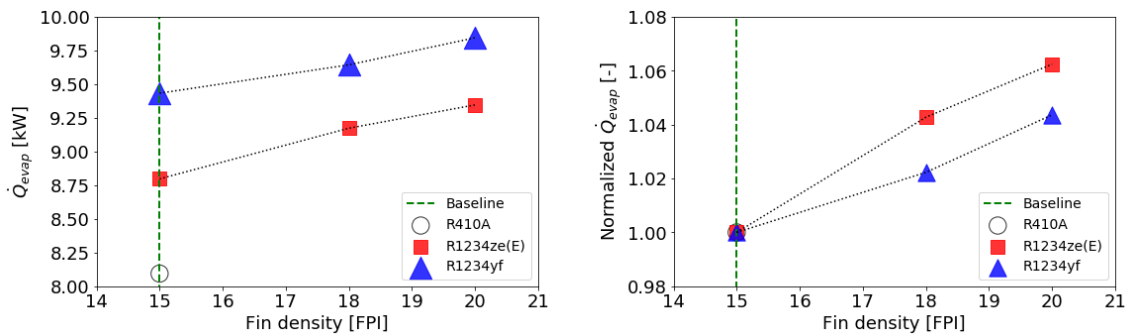
(a) FTHX capacities, and normalized FTHX capacities against baseline values for each fluid, as a function of fin density

141
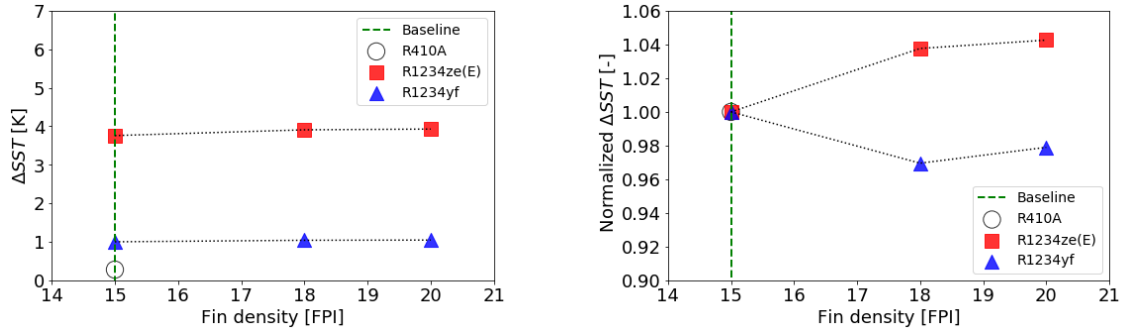
(b) Refrigerant SST drop, and normalized refrigerant SST drop against baseline values for each fluid, as a function of fin density
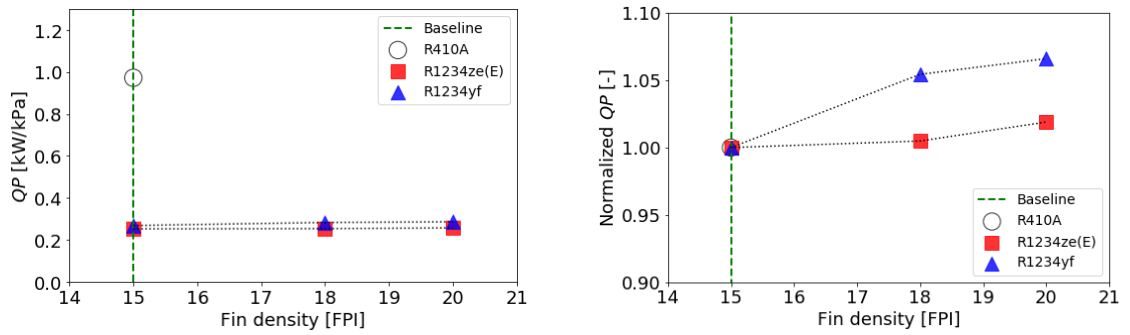
(c) QP, and normalized QP against baseline values for each fluid, as a function of fin density

Figure 6.3. Influence of fin density on simulated FTHX performance

Increasing fin density results in an increase in FTHX capacity for both HFOs, as shown in Figure 6.3. However, with increasing fin density, the SST drop increases for R1234ze(E) but decreases for R1234yf. Interestingly, from Figure 6.3 d), and e), it can be seen that the value of QP increases for both HFOs at higher fin densities. This implied that for R1234ze(E), the increase in FTHX capacity is more pronounced than the increase in refrigerant pressure drop. Based on these results, we recommended to increase the fin density of the baseline FTHX, in order to have improved FTHX performance with HFOs.

6.3.2 Effects of number of passes of refrigerant circuitry

Figure 6.4 shows the influence of the number of circuits on the FTHX's capacity, refrigerant SST drop, and the ratio *QP*.
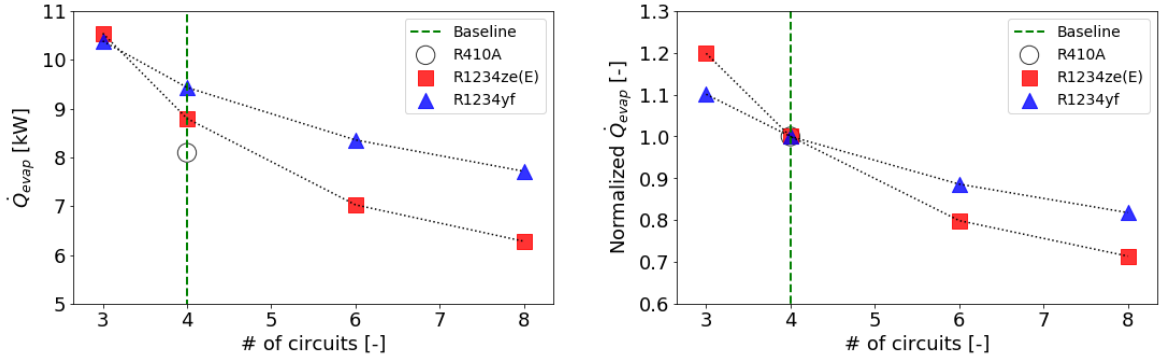
(a) FTHX capacities, and normalized FTHX capacities against baseline values for each fluid, as a function of number of circuits
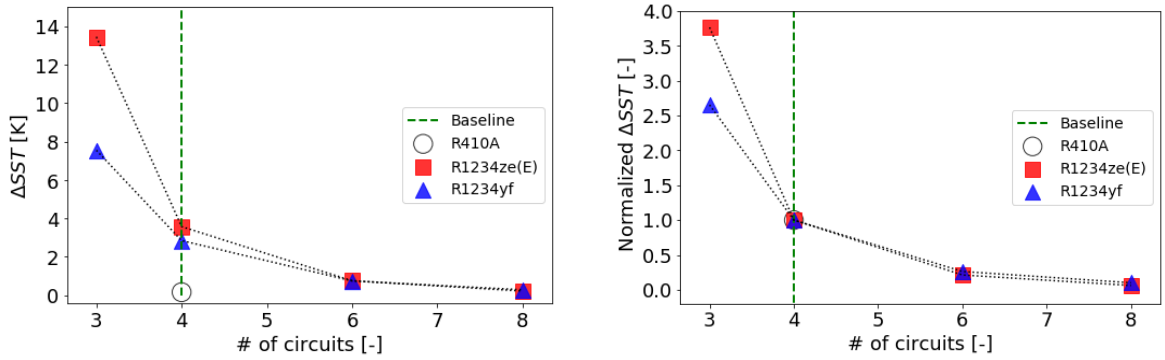
(b) Refrigerant SST drop, and normalized refrigerant SST drop against baseline values for each fluid, as a function of number of circuits
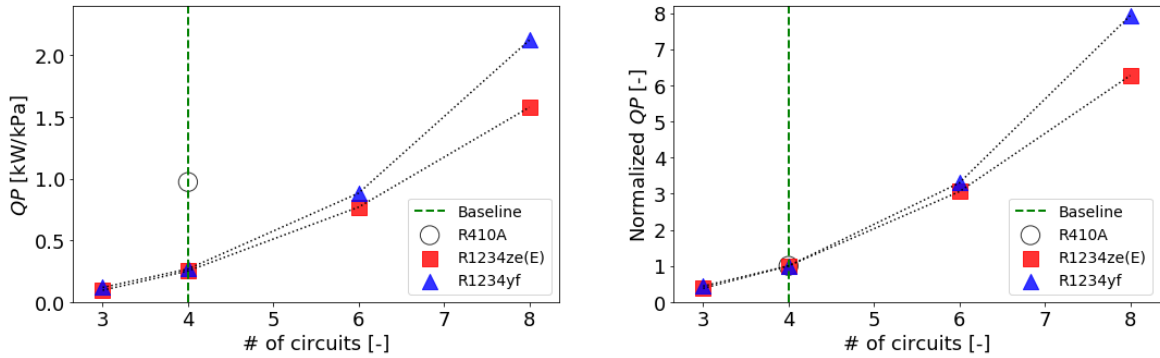
(c) QP, and normalized QP against baseline values for each fluid, as a function of number of circuits

Figure 6.4. Influence of number of circuits on simulated FTHX performance

Figure 6.4 (a) shows a decrease in FTHX capacity with increasing number of circuits. With increasing number of circuits, the overall refrigerant flow decreases to achieve the same superheat. This causes the convective heat transfer coefficient to decrease, thus resulting in decreased capacity. Additionally, the decrease in refrigerant flow (with increasing number of circuits), leads to a significant decrease in SST drop, and hence refrigerant pressure drop, for the simulated FTHX with highest number of circuits, as shown in Figure 6.4 (b). As an example, for R1234ze(E), an increase in capacity of 20% in the FTHX with three circuits relative to the 4-circuit baseline, also resulted in a more than 3-fold increase in refrigerant pressure. Figure 6.4 (c), more generally, shows that the decrease in refrigerant pressure drop is much more significant than the decrease in FTHX capacity, the FTHX with eight circuits was most favorable, to achieve the highest value of QP. Thus, we recommended to increase the number of circuits to reduce refrigerant pressure drop for HFOs to acceptable limits (see Table 6.6).

6.3.3 Effects of refrigerant tube diameter

Figure 6.5 shows the effect of tube diameters on the simulated FTHX capacity, refrigerant pressure drop, and the ratio *QP*.
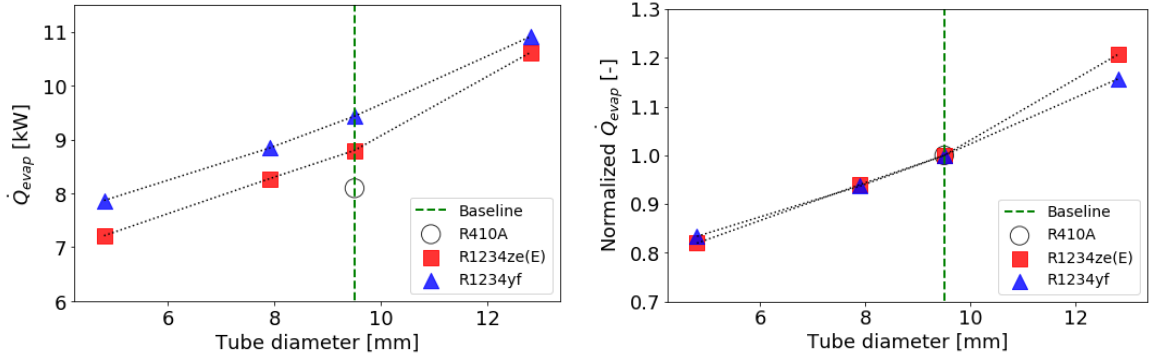
(a) FTHX capacities, and normalized FTHX capacities against baseline values for each fluid, as a function of tube diameter
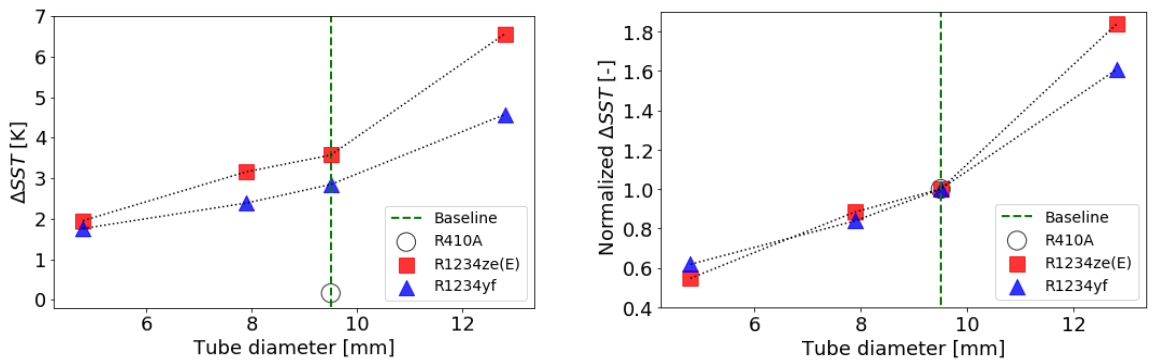
(b) Refrigerant SST drop, and normalized refrigerant SST drop against baseline values for each fluid, as a function of tube diameter
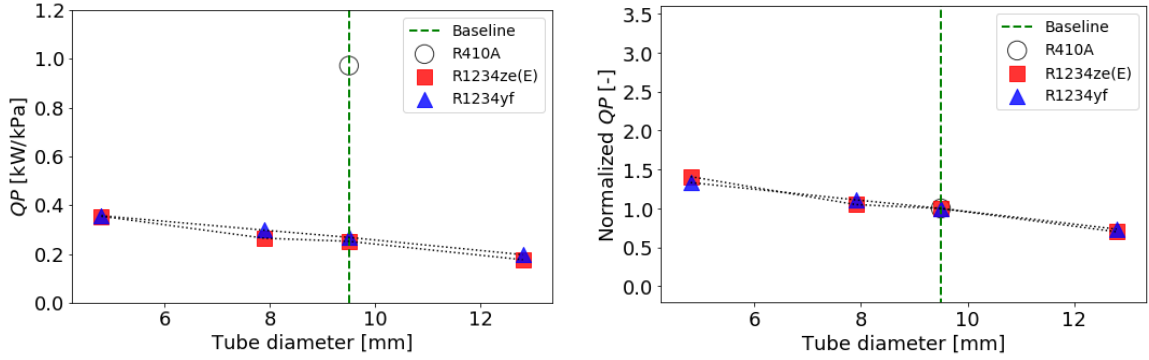
(c) QP, and normalized QP against baseline values for each fluid, as a function of tube diameter

Figure 6.5. Influence of tube diameter on simulated FTHX performance
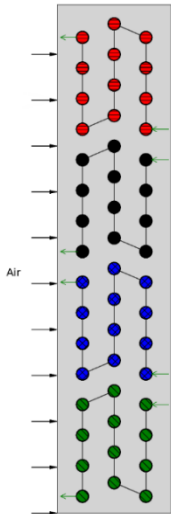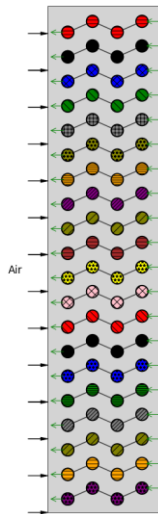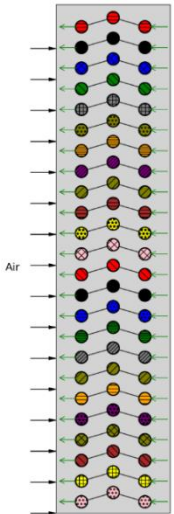
With an increase in tube diameter, the number of circuits in the FTHX is decreasing, resulting in more passes per circuit for the refrigerant, resulting in availability of more heat transfer area. Additionally, the overall refrigerant flow rate required to achieve the same superheat also increases with increasing tube diameter. Figure 6.5 (a) shows a combination of both these factors, indicating an increase in capacity with increasing tube diameter. Refrigerant pressure drop per unit length is approximately proportional to the square of the velocity; in addition, it increases with the length of a circuit. As a result of a combination of these two factors, Figure 6.5 (b) shows an increase in SST drop, which implies increase in pressure drop, with increasing tube diameter. Finally, Figure 6.5 (c) shows that with increasing tube diameter, the increase in refrigerant pressure drop is more pronounced than capacity increase, resulting in decreasing QP. Thus, we recommend considering a decrease in tube diameters in order to improve overall FTHX performance with HFOs.

6.3.4 Effects of multiple parameter changes

Based on the results from the previous sections and some additional trial and error experiments, it

became evident that FTHX slab size will require more face area, *i.e.,* either increase in tube length, or increasing the FTHX height to fit an additional row, in order to have a FTHX design that provided increased FTHX capacity, and acceptable refrigerant pressure drop with HFOs. Table 6.9 shows key parameters of the baseline FTHX design, along with those for two custom designs. Figure 6.6 compares the simulated FTHX capacity, refrigerant SST drop, and the ratio *QP*, of the custom configurations with the baseline FTHX design.

Table 6.9. Key geometrical parameters of baseline FTHX modified for the customized configurations, along with their circuitry designs

FTHX name	Baseline	Custom 1	Custom 2
of circuits	4	20	24
# of tubes	48	80	72
# of tube banks	3	4	3
Fin density	15 FPI	20 FPI	
Tube length	0.495 m	0.545 m	0.495 m
Tube diameter	9.53 mm	4.76 mm	
FTHX dimensions	17" x 4" x 19"	17" x 4" x 21"	17.04" x 4" x 19"
Circuitry			
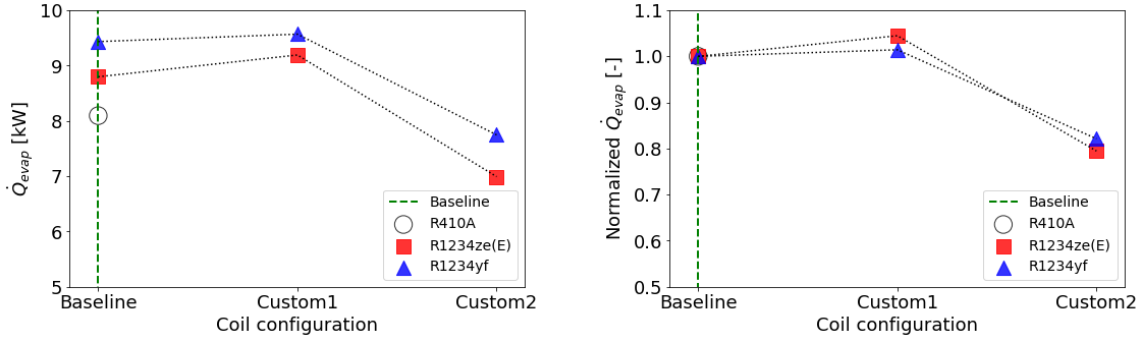
147

(a) FTHX capacities, and normalized FTHX capacities against baseline values for each fluid, for the custom designs
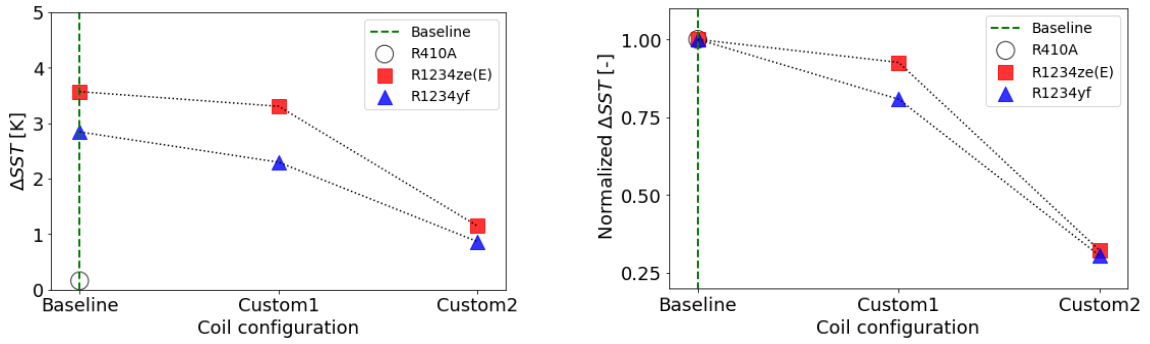
(b) Refrigerant SST drop, and normalized refrigerant SST drop against baseline values for each fluid, for the custom designs
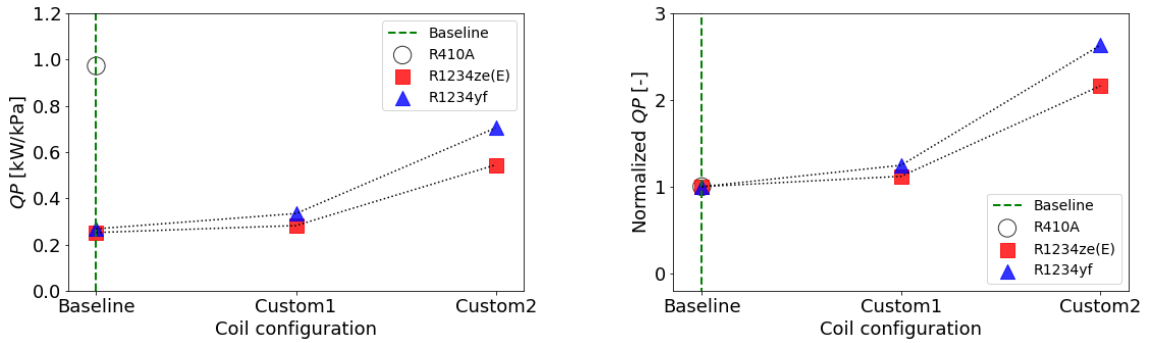
(c) QP, and normalized QP against baseline values for each fluid, for the custom designs

Figure 6.6. Comparison of FTHX performance for custom designs compared against baseline

It can be seen from Figure 6.6 (a) that "custom 1" leads to only a marginal increase in capacity, i.e., 1.4% and 4.5% for R1234yf and, R1234ze(E) respectively. The refrigerant side SST drop also

drops down for this configuration, by 19% and 6.7% for R1234yf, and R1234ze(E) respectively. The corresponding change in QP comes out to be 25% and 12% for R1234yf, and R1234ze(E) respectively. However, the "custom 2" configuration leads to the refrigerant side pressure drop for both HFOs dropping to acceptable values, as per Table 6.6, at the expense of capacity reduction of 18% and 21% for R1234yf and R1234ze(E) respectively.

By comparison of all the parametric simulation studies, including those from Sections 6.3.1 to 6.3.3 with baseline slab sizes, the custom 2 configuration gave the best compromise between reduction in refrigerant pressure drop, and FTHX capacity. Based on these results, depending on the design goal, which may either be increase in FTHX capacity, or reduction in refrigerant pressure drop, the geometric parameters that need to be modified are listed in Table 6.10. These modifications can be used as a basis for fin-and-tube heat exchanger manufacturers, so they can smoothly make the transition from high GWP HFCs in their current products, to next generation low-GWP HFOs, to have products that are cost effective, energy efficient, and environment friendly.

Table 6.10. Assessment of heat exchanger geometrical parameters that need to be modified, depending on the design goal when using ultra-low-GWP HFOs

	Design goal	
	Increase in FTHX capacity	Decrease in refrigerant side pressure drop
FTHX height	No change	Increase
FTHX width	No change	
Number of tubes	Increase	
Number of circuits	Increase	
Fin density	Increase	
Tube length	Increase	No change
Tube diameter	Decrease	

149

6.4 Conclusions

This paper presents a simulation study for modifying the design of an R410A based fin-and-tube heat exchanger FTHX, to observe how FTHX capacity and refrigerant pressure drop, would be affected if R410A was substituted with two ultra-low-GWP HFOs: R1234yf, and R1234ze(E). The original FTHX had four circuits, sixteen tube rows, three tube banks, 48 tubes, fin density of 15 FPI, and tubes with outer diameter of 9.53mm. The aim was to have a FTHX design with increased FTHX capacity compared to the baseline design, and/or a refrigerant pressure drop with HFOs within an acceptable range. To encapsulate the overall FTHX performance, the term QP was defined as the ratio of FTHX capacity to the refrigerant side pressure drop and investigated as well.

It was found that, regardless of the specific desired design goals for the FTHX, the following changes will always lead to improved performance:

- Increase in fin density of FTHX,

- Increase in number of circuits,

- Decrease in tube diameter,

- Increase in number of tubes in the FTHX,

The major outcomes of this work are summarized below:

- By increasing the fin density from 15 FPI to 18 FPI, the QP increased by 6.6% and 1.9% for R1234yf, and R1234ze(E), respectively

- By increasing the number of circuits from 4 to 8, the QP increased by 7.9 times and 6.3 times for R1234yf, and R1234ze(E), respectively

- By decreasing the tube diameter from 9.53mm to 4.76 mm, increasing number of circuits from 4 to 20, and increasing number of tubes from 48 to 80, the QP increased by 33% and 41% for R1234yf, and R1234ze(E), respectively

Based on the above results, two custom FTHX designs were simulated; the 1st design prioritized increase in FTHX capacity, and the 2nd design prioritized reduction in refrigerant pressure drop to acceptable limits. In addition to all the aforementioned design changes, the custom design for increasing capacity had a longer tube length, and while the design for the reduced refrigerant pressure drop had an additional tube bank of tubes, implying that the FTHX slab size has to change to either improve FTHX performance with HFOs or to match the capacity and pressure drop characteristics of an R410A FTHX.

In the future, the work in this research will be expanded to include a techno economic analysis, where costs of modifying the FTHX geometry will be accounted for and compared to how much improvement they provide in FTHX performance with low-GWP fluids. Additionally, work will be done to experimentally measure the amount of low-GWP charge dynamically in residential and commercial FTHXs, which will provide data that is crucial for adoption of low-GWP A2L fluids.

CHAPTER VII

CONCLUSIONS & FUTURE WORK

7.1 Summary

This research led to an improved understanding of the behavior of low-GWP refrigerants in of fin-and-tube heat exchangers (FTHXs) in residential and commercial applications. A set of guidelines were developed for pseudo-optimal design of FTHXs to accommodate the next (fourth) generation of low-GWP refrigerants, with a goal to obtain near optimal performance under current manufacturing constraints. Chapter 1 explained how the introduction of fourth generation low-GWP refrigerants is compelling manufacturers of FTHXs to transition to these new fluids, since HFCs such as R410A will be phased out due to their high GWP. Transition to these low-GWP fluids will ensure that the next generation AC and heat pump equipment is cost effective, energy efficient and environment friendly. A review of literature showed that majority of the experimental and simulations efforts to replace existing high-GWP HFCs for air source equipment focused on the entire vapor compression system, rather than looking only at the heat exchanger.

Chapter 1 outlined the research objectives for this dissertation. In Chapter 2, a novel experimental facility was developed for the purpose of testing air-to-refrigerant FTHXs, so that high-fidelity experimental data obtained from the facility could be used for advanced heat exchanger model

validations. A preliminary experiment showed that the experimental facility confirmed to the 5% energy balance limit on refrigerant and airside set by ASHRAE Standard 33 (2016). Chapter 3 detailed how the cross-fin (Xfin) segment-by-segment FTHX model was thoroughly validated, after three custom designed heat exchangers with distinct refrigerant circuitries, and two different sizes, were tested with refrigerant R410A on the experimental facility developed in Chapter 2. The mean absolute percentage error (MAPE) between the experimental, and model predicted capacities was found to be 1.0%, 2.4%, and 0.9%, for the interleaved, vertical, and block circuited coils, respectively, when cross-fin conduction was accounted for in the model. These results established the Xfin model as a reliable tool to predict FTHX performance for different circuitries. Chapter 4 showed a preliminary simulation study to investigate the change in system performance metrics of an R410A based water-to-water heat pump, if R454B and R452B were used as low-GWP "drop-in" alternatives. This was established by using performance data from the manufacturer of a commercial WSHP for validation of a simpler (moving boundary) refrigerant-to-water condenser model, coupled to fixed efficiency compressor, lumped evaporator, and isenthalpic expansion valve models. The study showed that some design changes may be necessary to existing equipment, in order to adapt them for near optimum performance, in case their existing refrigerants are substituted with next generation of low-GWP fluids. Chapter 5 continued from this work, by validating the Xfin model from experimental data obtained by running tests with R1234ze(E) on the block circuited FTHX from Chapter 3. The MAPE between the experimental and model predicted data for R1234ze(E) was found to be 1.4%. These validation results, in addition to those in Chapter 3, indicated that the Xfin model is a reliable modelling tool for parametric simulations with R410A and R1234ze(E). Simulations were carried out by altering the fin density and refrigerant circuitry of the original FTHX. An increase in fin density from 15 to 20 fins per inch (FPI) caused the capacity to increase by 4.9%, and the

refrigerant side pressure drop to decrease by 4.5%. For the refrigerant circuitry optimizations, a maximum increase in capacity of 5.6% was observed when compared to the baseline, but at the expense of 7.5 times higher pressure drop. Alternatively, a separate circuitry resulted in a 38% pressure drop reduction and 2.5% reduction in capacity. These results indicated that FTHX performance is sensitive to the geometry, implying that design changes could be made to existing FTHXs to enable better performance with low-GWP refrigerants. Finally, in Chapter 6, HFO refrigerants R1234yf and R1234ze(E) were considered as the ultra-low-GWP replacements for the R410A based block circuited FTHX. Simulations were carried out with the same operational conditions, and a fixed outlet refrigerant superheat for all fluids by modifying several FTHX geometrical parameters. It was found that the FTHX performance, for a fixed slab size, in terms of $\dot{Q}_{evap}/\Delta P_{ref}$, was the most sensitive to number of circuits, followed by the tube diameter, number of tubes in the heat exchanger, and the fin density. Based on the simulation results, two customized FTHX designs were suggested, with different changes to the FTHX slab size. One design prioritized increased FTHX capacity, and the other prioritized reduction in refrigerant pressure drop to acceptable limits.

7.2 Conclusions

The dissertation aimed to answer two research questions, namely,

> *"How is heat exchanger performance affected if fin-and-tube heat exchanger coils and coaxial heat exchangers designed for R410A are operated with low-GWP refrigerants?"*

and,

> *"How does heat exchanger designed need to be changed to obtain near-optimum performance for low-GWP refrigerants under current manufacturing constraints?"*

The major conclusions drawn from this work are summarized below.

To test refrigerants of different types on FTHXs, that exhibit different behavior, i.e., different operating pressures of R410A and R1234ze(E) for the same saturation temperature, a pumped refrigerant conditioning loop can allow easy switching of fluids, without making any changes to the components in the loop. Experiments performed on this setup using the same FTHX coil with R410A and R1234ze(E) helped in answering the first research question. For numerical modelling of multi circuit FTHX performance, taking into account cross-fin conduction will provide more accurate results. For part load operation (refrigerant in some circuits only), the impact of cross-fin conduction effecting the FTHX capacity is highly dependent on the circuitry arrangement, and also the proportion of active circuits.

Finally, to answer the second research question, some design changes were proposed to accommodate ultra-low-GWP fluids in R410A based FTHX equipment. These design changes were necessitated by the different thermodynamic and transport properties of R410A and the ultra-low-GWP fluids, such as HFOs R1234yf and R1234ze(E). To increase overall FTHX performance for a fixed slab size, in terms of the ratio $\dot{Q}_{evap}/\Delta P_{ref}$, the fin density, number of circuits, and number of tubes must be increased, while the tube diameter must be decreased. In order to prioritize increase in FTHX capacity, the tube length has to be increased, while for prioritizing reduction in refrigerant pressure drop to acceptable values, an additional bank of tubes has to be added to the FTHX. These designs demonstrated that, with HFO's, it will be challenging to achieve both the same capacity and pressure drop characteristics as R410A without modifications to FTHX size.

7.3 Future work

The work should be extended to have a techno economic analysis, where the added costs associated with modifying the FTHX geometry, *e.g.,* adding more aluminum to increase fin density, should be compared with the improvements in system performance. Additionally, costs of the new low-GWP fluids should also be considered, because at present some of them are more expensive than the high GWP fluids they are intended to replace. Additionally, the Total Equivalent Warming Impact (TEWI) of AC and heat pump systems with different refrigerants should be analyzed as well, to understand the lifecycle impact of these systems on the environment. TEWI does not only take into account the warming impact from leakage of high GWP refrigerants, but also that from CO_2 emissions produced when fossil fuels are burnt to generate electricity needed to run the equipment.

The Xfin model will be simulated with low-GWP HFC/HFO blends, such as R454B, R452B, etc., to evaluate how temperature glide occurring during evaporation will impact FTHX capacity and refrigerant pressure drop. Geometrical parameters will be modified for these two fluids, in order to compare how sensitive is their change in capacity and refrigerant pressure drop to the FTHX geometry. The Xfin model will be validated by testing FTHXs in condenser mode, with R410A, low-GWP HFOs and HFC/HFO blends, in order to observe the thermal performance of low-GWP fluids on FTHX condensers. Additionally, airside pressure drop data should be collected by testing FTHXs and validating against Xfin model predicted values. This will allow this work to extend towards system level, since air side pressure drop is an important FTHX parameter to be accounted for redesign of these systems for accommodating low-GWP refrigerants. Finally, to reduce the time

taken for Xfin model simulations, the model should be converted from the high level, non-compiled

scripting language (Python) it is currently written in, to a low level, compiled language such as C

#.

REFERENCES

ASHRAE (2010). *2010 ASHRAE Handbook: Refrigeration*. Atlanta, USA.

ASHRAE (2016a). *ASHRAE Standard 33 -Methods of testing for rating electrically driven unitary air conditioning and heat pump equipment*. Atlanta, USA.

ASHRAE (2016b). *ASHRAE Standard 51-16 (ANSI/AMCA Standard 210-16. Laboratory Methods Of Testing Fans For Certified Aerodynamic Performance Rating*. Atlanta, USA.

ANSI/AHRI/ASHRAE. (1998). *ISO Standard 13256-2: Water-source heat pumps — Testing and rating for performance — Part 1: Water-to-air and brine-to-air heat pumps* (Vol. 1998). Atlanta, USA.

ANSI/ASHRAE Standard 37-2009. (2009). *Methods of Testing for Rating Electrically Driven Unitary Air-Conditioning and Heat Pump Equipment*. Atlanta, USA: American Society of Heating, Refrigeration and Air-Conditioning Engineers.

ASHRAE (2019). Designation and safety classification of refrigerants. In *ANSI/ASHRAE Standard 34* (Vol. 2019). Atlanta,USA.

Aslan, O. (2010). *Sensors, Instrumentation and Process Control System Design of the OSU Psychrometric Chamber*. Master`s Thesis. Oklahoma State University.

ASME PTC 19.1 - 2013. (2013). *Test uncertainty - Performance Test Codes*. New York: American Society of Mechanical Engineers.

Bach, C. K. L. (2014). Refrigerant side compensation for air-side maldistribution of evaporators and its effects on system performance. PhD dissertation. Purdue University. Retrieved from https://search.proquest.com/docview/1647472827

Bach, C. K., Groll, E. A., Braun, J. E., & Horton, W. T. (2014). Mitigation of air flow maldistribution in evaporators. *Applied Thermal Engineering*, *73*(1), 879–887. https://doi.org/10.1016/j.applthermaleng.2014.08.010

Blecich, P. (2015). Experimental investigation of the effects of airflow nonuniformity on performance of a fin-and-tube heat exchanger. International Journal of Refrigeration, 59, 65–74. https://doi.org/10.1016/j.ijrefrig.2015.06.029

Bahman, A. M., & Groll, E. A. (2017). Application of interleaved circuitry to improve evaporator effectiveness and COP of a packaged AC system. *International Journal of Refrigeration*, *79*, 114–129. https://doi.org/10.1016/j.ijrefrig.2017.03.026

Blasius, H. (1913). *Das Ähnlichkeitsgesetz bei Reibungsvorgängen in Flüssigkeiten*.

Bobbo, S., Nicola, G. Di, Zilio, C., Brown, J. S., & Fedele, L. (2018). Low-GWP halocarbon refrigerants: A review of thermophysical properties. *International Journal of Refrigeration*, *90*, 181–201. https://doi.org/10.1016/j.ijrefrig.2018.03.027

Calm, J. M. (2008). The next generation of refrigerants - Historical review, considerations, and outlook. *International Journal of Refrigeration*, *31*(7), 1123–1133. https://doi.org/10.1016/j.ijrefrig.2008.01.013

Castro, J. B., Urchueguía, J. F., Corberán, J. M., & Gonzálvez, J. (2005). Optimized design of a heat exchanger for an air-to-water reversible heat pump working with propane (R290) as refrigerant: Modelling analysis and experimental observations. *Applied Thermal Engineering*, 25(14–15), 2450–2462. https://doi.org/10.1016/j.applthermaleng.2004.12.009

Chen, X., Yang, J., Liu, C., & Chen, J. (2018). Heating performance comparison of R410A and its substitutions in air-to-water heat pumps with vapor injection. *International Journal of Refrigeration*, *96*, 78–87. https://doi.org/10.1016/j.ijrefrig.2018.09.007

Chu, W. X., Sheu, W. J., Hsu, C. C., & Wang, C. C. (2020). Airside performance of sinusoidal wavy fin-and-tube heat exchangers subject to large-diameter tubes with round or oval configuration. *Applied Thermal Engineering*, *164*. https://doi.org/10.1016/j.applthermaleng.2019.114469

COOLING POST. (2019). Carrier picks R454B for ducted ac. Retrieved May 30th, 2019, from https://www.coolingpost.com/world-news/carrier-picks-r454b-for-ducted-ac/

Core Writing Team, Pachauri, R. K., & Meyer, L. A. (2014). *Climate Change 2014: Synthesis Report. Contribution of Working Groups I, II and III to the Fifth Assessment Report of the Intergovernmental Panel on Climate Change*. Geneva, Swtizerland.

Cremaschi, L., & Lee, E. (2008). Design and heat transfer analysis of a new psychrometric environmental chamber for heat pump and refrigeration systems testing. *ASHRAE Transactions*, *114*(2), 619–631.

Cremaschi, L., & Perez Paez, P. (2017). Experimental feasibility study of a new load-based method of testing for light commercial unitary heating, ventilation, and air conditioning (ASHRAE RP-1608). *Science and Technology for the Built Environment*, *23*(7), 1178–1188.

Cuolomb, D., Dupont, J., & Morlet, V. (2017). 35th Informatory Note on Refrigeration Technologies: The impact of the refrigeration sector on climate change. In *IIR Information*. Retrieved from http://www.iifiir.org/

Devecioğlu, Atilla G., & Oruç, V. (2020). Energetic performance analysis of R466A as an alternative to R410A in VRF systems. *Engineering Science and Technology, an International Journal*, *23*(6), 1425–1433. https://doi.org/10.1016/j.jestch.2020.04.003

Devecioğlu, Atilla Gencer. (2017a). Seasonal performance assessment of refrigerants with low-GWP as substitutes for R410A in heat pump air conditioning devices. *Applied Thermal Engineering*, *125*, 401–411. https://doi.org/10.1016/j.applthermaleng.2017.07.034

Devecioğlu, Atilla Gencer. (2017b). Seasonal performance assessment of refrigerants with low-GWP as substitutes for R410A in heat pump air conditioning devices. *Applied Thermal Engineering*, *125*, 401–411. https://doi.org/10.1016/j.applthermaleng.2017.07.034

Domanski, P. A., Choi, J. M., & Payne, W. V. (2007). Longitudinal heat conduction in finned-tube evaporators. *International Congress of Refrigeration*.

Domanski, P., Yashar, D., & Wojtusiak, J. (2016). EVAP-COND, Version 4.0; Simulation Models for Finned-Tube Heat Exchangers with Circuitry Optimization. *NIST/EL*. Retrieved from https://www.nist.gov/publications/evap-cond-version-40-simulation-models-finned-tube-heat-exchangers-circuitry

ECACool. (2019). R452B offered on Clint chillers. Retrieved October 10th, 2019, from https://www.ecacool.com/en/news/r452b_clint_chillers/

Environmental Protection Agency (EPA). (2021). *Phasedown of Hydrofluorocarbons: Establishing the Allowance Allocation and Trading Program Under the American Innovation and Manufacturing Act* (Vol. 86).

Ertesvåg, I. S. (2011). Uncertainties in heat-pump coefficient of performance (COP) and exergy efficiency based on standardized testing. *Energy and Buildings*, *43*(8), 1937–1946. https://doi.org/10.1016/j.enbuild.2011.03.039

Friedel, L. (1979). Improved Friction Pressure Drop Correlation for Horizontal and Vertical Two-Phase Pipe Flow. *European Two-Phase Flow Group Meeting, Paper E2*. Ispra.

Fukuda, S., Kondou, C., Takata, N., & Koyama, S. (2014). Low-GWP refrigerants R1234ze(E) and R1234ze(Z) for high temperature heat pumps. *International Journal of Refrigeration*, *40*, 161–173. https://doi.org/10.1016/J.IJREFRIG.2013.10.014

Gnielinski, V. (1975). New equations for heat and mass transfer in the turbulent flow in pipes and channels. *NASA STI/Recon Technical Report A*, *75*, 8–16. Retrieved from http://adsabs.harvard.edu/abs/1975STIA...7522028G

Grauso, S., Mastrullo, R., Mauro, A. W., Thome, J. R., & Vanoli, G. P. (2013). Flow pattern map, heat transfer and pressure drops during evaporation of R-1234ze(E) and R134a in a horizontal, circular smooth tube: Experiments and assessment of predictive methods. *International Journal of Refrigeration*, *36*(2), 478–491. https://doi.org/10.1016/j.ijrefrig.2012.07.016

H. Bell, I., Wronski, J., Quoilin, S., & Lemort, V. (2014). Pure and Pseudo-pure Fluid Thermophysical Property Evaluation and the Open-Source Thermophysical Property Library CoolProp. *Industrial Engineering Chemistry Research*, *53*(6), 2498–2508. https://doi.org/10.1021/ie4033999

Haikawa, T., Nuno, H., & Taira, S. (2016). Performance Evaluation of Heat pump System using R32 and HFO-mixed Refrigerant in High Ambient Temperature. *International Refrigeration and Air Conditioning Conference*. https://doi.org/10.18462/iir.icr.2015.0916

Heredia-Aricapa, Y., Belman-Flores, J. M., Mota-Babiloni, A., Serrano-Arellano, J., & García-Pabón, J. J. (2020a). Overview of low-GWP mixtures for the replacement of HFC refrigerants: R134a, R404A and R410A. *International Journal of Refrigeration*, Vol. 111, pp. 113–123. https://doi.org/10.1016/j.ijrefrig.2019.11.012

Heun, M. K., & Crawford, R. . (1994). Longitudinal fin conduction in multipass cross-counterflow finned-tube heat exchangers. *ASHRAE Transactions*, *100*, 382–389. Retrieved from https://www.techstreet.com/standards/3774-longitudinal-fin-conduction-in-multipass-cross-counterflow-finned-tube-heat-exchangers?product_id=1716645

Huang, L., Aute, V., & Radermacher, R. (2014). A finite volume coaxial heat exchanger model with moving boundaries and modifications to correlations for two-phase flow in fluted annuli. *International Journal of Refrigeration*, *40*, 11–23. https://doi.org/10.1016/j.ijrefrig.2013.11.012

Hughes, J., & Minor, B. H. (2018). Non-Flammable R-410A Alternative for Commercial Refrigeration and Air Conditioning. *International Refrigeration and Air Conditioning Conference*, Paper 1944. Purdue, USA.

Incropera, F. P., Dewitt, D. P., Bergman, T. L., & Lavine, A. S. (2011). *Fundamentals of Heat and Mass Transfer* (John Wiley & Sons, Ed.).

Jia, X., Wang, J., Wang, X., Hu, Y., & Sun, Y. (2020). Phase equilibrium of R1234yf and R1234ze(E) with POE lubricant and thermodynamic performance on the evaporator. *Fluid Phase Equilibria*, *514*, 112562. https://doi.org/10.1016/J.FLUID.2020.112562

Jiang, H., Aute, V., & Radermacher, R. (2006). CoilDesigner: a general-purpose simulation and design tool for air-to-refrigerant heat exchangers. *International Journal of Refrigeration*, *29*(4), 601–610. https://doi.org/10.1016/j.ijrefrig.2005.09.019

Kim, N. H. (2016). An experimental investigation on the airside performance of fin-and-tube heat exchangers having slit fins under wet condition. Journal of Thermal Science and Technology, 11(1), 5011–5019. https://doi.org/10.1299/jtst.2016jtst0005

Klein, S. A. (2019). *Engineering Equation Solver, Academic Professional V10.644-3D*. F-Chart Software.

Lee, J., Kwon, Y. C., & Kim, M. H. (2003). An improved method for analyzing a fin and tube evaporator containing a zeotropic mixture refrigerant with air mal-distribution. International Journal of Refrigeration, 26(6), 707–720. https://doi.org/10.1016/S0140-7007(03)00023-9

Lee, H., Hwang, Y., Radermacher, R., & Chun, H. H. (2013). Potential benefits of saturation cycle with two-phase refrigerant injection. *Applied Thermal Engineering*, *56*(1–2), 27–37. https://doi.org/10.1016/J.APPLTHERMALENG.2013.03.030

Lee, J. A., Bach, C. K., & Bradshaw, C. (2018). CFD Case Study : Heat Exchanger Inlet Air Velocity Distribution for Ducted Tests in a Psychrometric Chamber (ASHRAE RP-1785). *International Refrigeration and Air Conditioning Conference at Purdue*. Retrieved from https://docs.lib.purdue.edu/iracc/2068/

Lee, J. A., Bach, C. K., & Bradshaw, C. R. (2019). Study of Heat Exchanger Inlet Air Velocity Distribution for Ducted Tests in a Psychrometric Chamber (ASHRAE RP-1785). *ASHRAE Transactions*. Kansas City.

Lee, J., & Domanski, P. A. (n.d.). *Impact of Air and Refrigerant Maldistributions On the Performance of Finned-Tube Evaporators With R-22 and R-407C*. Retrieved from https://www.nist.gov/publications/impact-air-and-refrigerant-maldistributions-performance-finned-tube-evaporators-r-22

Lemmon, E. W., Bell, I. H., Huber, M. ., & McLinden, M. O. (2018). *NIST Standard Reference Database 23: Reference Fluid Thermodynamic and Transport Properties-REFPROP, Version 10.0*. https://doi.org/https://dx.doi.org/10.18434/T4JS3C

Li, Z., Shen, B., & Gluesenkamp, K. (2021a). Optimization of Refrigerant Compositions for Low-GWP Refrigerant Mixtures Using Segment-by-segment Heat Exchanger and Detailed System Models. *18th International Refrigeration and Air Conditioning Conference*, 1–10. Purdue, USA.

Li, Z., Shen, B., & Gluesenkamp, K. R. (2021b). Multi-objective optimization of low-GWP mixture composition and heat exchanger circuitry configuration for improved system performance and reduced refrigerant flammability. *International Journal of Refrigeration*, *126*, 133–142. https://doi.org/10.1016/J.IJREFRIG.2021.01.003

Liang, S. Y., Wong, T. N., & Nathan, G. K. (2001). Numerical and experimental studies of refrigerant circuitry of evaporator coils. International Journal of Refrigeration, 24(8), 823–833. https://doi.org/10.1016/S0140-7007(00)00050-5

Lifferth, S. O. (2009). *Design and Construction of a New Psychrometric Chamber*. Master's Thesis. Oklahoma State University.

Ma, X., Ding, G., Zhang, Y., & Wang, K. (2007). Airside heat transfer and friction characteristics for enhanced fin-and-tube heat exchanger with hydrophilic coating under wet conditions. International Journal of Refrigeration, 30(7), 1153–1167. https://doi.org/10.1016/j.ijrefrig.2007.03.001

Martínez, L. C. C., Parise, J. A. R., Motta, S. F. Y., & Becerra, E. de C. V. (2010). Plate-fin and Tube Heat Exchangers Refrigerant Circuiting Optimization in Vapor Compression Refrigeration Systems. *International Refrigeration and Air Conditioning Conference*, (1989), 1–8.

McLinden, M. O., & Huber, M. L. (2020). (R)Evolution of Refrigerants. *Journal of Chemical and Engineering Data*, 65(9), 4176–4193. https://doi.org/10.1021/acs.jced.0c00338

Mota-Babiloni, A., Navarro-Esbrí, J., Barragán, Á., Molés, F., & Peris, B. (2014). Drop-in energy performance evaluation of R1234yf and R1234ze(E) in a vapor compression system as R134a replacements. *Applied Thermal Engineering*, *71*(1), 259–265. https://doi.org/10.1016/J.APPLTHERMALENG.2014.06.056

Mota-Babiloni, A., Navarro-Esbrí, J., Barragán-Cervera, Á., Molés, F., & Peris, B. (2015). Analysis based on EU Regulation No 517/2014 of new HFC/HFO mixtures as alternatives of high GWP refrigerants in refrigeration and HVAC systems. *International Journal of Refrigeration*, *52*, 21–31. https://doi.org/10.1016/j.ijrefrig.2014.12.021

Mota-Babiloni, A., Navarro-Esbrí, J., Molés, F., Cervera, Á. B., Peris, B., & Verdú, G. (2016). A review of refrigerant R1234ze(E) recent investigations. *Applied Thermal Engineering*, Vol. 95, pp. 211–222. https://doi.org/10.1016/j.applthermaleng.2015.09.055

Myers, R. H., & Montgomery, D. C. (1995). *Response Surface Methodology: Process and Product Optimization Using Designed Experiments*. New York: John Wiley and Sons.

Nair, V. (2021). HFO refrigerants: A review of present status and future prospects. *International Journal of Refrigeration*, *122*, 156–170. https://doi.org/10.1016/j.ijrefrig.2020.10.039

Pardo, P., & Mondot, M. (2018). Experimental evaluation of R410A , R407C and R134a alternative refrigerants in residential heat pumps. *International Refrigeration and Air Conditioning Conference*, Paper 2498. Retrieved from https://docs.lib.purdue.edu/cgi/viewcontent.cgi?article=2990&context=iracc

Radermarcher, R. Hwang, Y. (2005). *Vapor compression heat pumps with refrigerant mixtures* (CRC Press, Ed.). https://doi.org/10.1201/9781420037579

Rajendran, P., Sidney, S., Ramakrishnan, I., & Dhasan, M. L. (2019). Experimental studies on the performance of mobile air conditioning system using environmental friendly HFO-1234yf as a refrigerant: *https://Doi.Org/10.1177/0954408919881236*, *235*(3), 731–742. https://doi.org/10.1177/0954408919881236

Rasmussen, B. D., & Jakobsen, A. (2000). Review of compressor models and performance characterizing variables. *International Compressor Engineering Conference*, 515–522. https://doi.org/Paper 1429

Saad Yatim, A., Shashikant Deokar, P., & Cremaschi, L. (2017). Oil retention in a microchannel type condenser and its effects on heat transfer rate performance and on the pressure drop. *Science and Technology for the Built Environment*, *23*(1), 166–180.

Sadeghianjahromi, A., & Wang, C. C. (2021). Heat transfer enhancement in fin-and-tube heat exchangers – A review on different mechanisms. *Renewable and Sustainable Energy Reviews*, *137*(January 2020). https://doi.org/10.1016/j.rser.2020.110470

Saleem, S., Sarfraz, O., Bradshaw, C. R., & Bach, C. K. (2020). Development of novel experimental infrastructure for collection of high-fidelity experimental data for refrigerant to air heat exchangers. *International Journal of Refrigeration*, *114*, 189–200. https://doi.org/10.1016/j.ijrefrig.2020.02.024

Saleem, S., Bradshaw, C. R., & Bach, C. K. (2021a). Validation of a multi-circuit heat exchanger model for evaluating the effect of refrigerant circuitry on cross-fin conduction in evaporator mode. *International Journal of Refrigeration*. https://doi.org/10.1016/J.IJREFRIG.2021.08.015

Saleem, S., Bradshaw, C. R., & Bach, C. K. (2021b). Performance assessment of R1234ze(E) as a low-GWP substitute to R410A in fin-and-tube heat exchangers. *Manuscipt accepted for publication in International Journal of Refrigeration*.

Sánchez, D., Cabello, R., Llopis, R., Arauzo, I., Catalán-Gil, J., & Torrella, E. (2017). Energy performance evaluation of R1234yf, R1234ze(E), R600a, R290 and R152a as low-GWP R134a alternatives. *International Journal of Refrigeration*, *74*, 269–282. https://doi.org/10.1016/J.IJREFRIG.2016.09.020

Sarfraz, O., Bach, C., & Bradshaw, C. (2018). A Literature Review of Numerical Modeling Techniques for Vapor Compression Systems with Focus on Heat Exchanger Modeling. *17th International Refrigeration and Air Conditioning Conference*, (July). Purdue, USA.

Sarfraz, O. (2019). *Development of an advanced fin-and-tube heat exchanger simulation tool for steady state conditions*. PhD dissertation. Oklahoma State University.

Sarfraz, O., Bach, C. K., & Bradshaw, C. (2019a). Discrete modeling of fin-and-tube heat exchangers with cross-fin conduction functionality. *International Journal of Refrigeration.* Retrieved from https://doi.org/10.1016/j.ijrefrig.2019.05.018

Sarfraz, O., Bach, C. K., & Bradshaw, C. (2019b). A novel technique for computationally efficient consideration of cross-fin conduction in fin-and-tube heat exchanger models. International Journal of Refrigeration., 107, 73–78.

Sarfraz, O., Bach, C. K., & Bradshaw, C. (2020). Validation of advanced fin-and-tube heat exchanger models with cross-fin conduction functionality. *International Journal of Refrigeration*, *116*, 70–81.

Schulz, M., & Kourkoulas, D. (2014). *Regulation (EU) No 517/2014 of The European Parliament and of the council of 16 April 2014 on fluorinated greenhouse gases and repealing Regulation (EC) No 842/2006*. Retrieved from https://eur-lex.europa.eu/legal-content/EN/TXT/PDF/?uri=CELEX:32014R0517&rid=1

Sethi, A., & Motta, S. F. Y. (2016). Low-GWP Refrigerants for Air-conditioning and Chiller Applications. *International Compressor Engineering, Refrigeration and Air Conditioning, and High Performance Buildings Conferences*, *2*(2013), 1–8.

Shah, M. M. (1982). Chart Correlation for Saturated Boiling Heat Transfer: Equations and Further Study. *ASHRAE Transactions*, Vol. 88, pp. 185–196.

Shah, Mirza Mohammed. (2013). General correlation for heat transfer during condensation in plain tubes: Further development and verification. *ASHRAE Transactions*, *119* (PART 2), 3–11.

Shen, B. (2006). *Heat pump simulation models at off-design conditions*. PhD dissertation. Purdue University.

Shen, B., Abdelaziz, O., Shrestha, S., & Elatar, A. (2018). Model-based optimizations of packaged rooftop air conditioners using low global warming potential refrigerants. *International Journal of Refrigeration*, *87*, 106–117. https://doi.org/10.1016/j.ijrefrig.2017.10.028

Sieres, J., Ortega, I., Cerdeira, F., & Álvarez, E. (2021). Drop-in performance of the low-GWP alternative refrigerants R452B and R454B in an R410A liquid-to-water heat pump. *Applied Thermal Engineering*, *182*, 116049. https://doi.org/10.1016/J.APPLTHERMALENG.2020.116049

Singh, V., Aute, V., & Radermacher, R. (2008). Numerical approach for modeling air-to-refrigerant fin-and-tube heat exchanger with tube-to-tube heat transfer. *International Journal of Refrigeration*, *31*(8), 1414–1425. https://doi.org/10.1016/j.ijrefrig.2008.03.013

Song, X., Huang, D., Liu, X., & Chen, Q. (2012). Effect of non-uniform air velocity distribution on evaporator performance and its improvement on a residential air conditioner. *Applied Thermal Engineering*, *40*, 284–293. https://doi.org/10.1016/j.applthermaleng.2012.02.024

Tosun, T., Ozturk, M. M., Doğan, B., & Erbay, L. B. (2021). The effect of refrigerant circuitry on the performance of a freezer with a tube-on-sheet evaporator. *Science and Technology for the Built Environment*. https://doi.org/10.1080/23744731.2020.1868193

U.S. Environmental Protection Agency. (2011). *Instructions for the Significant New Alternatives Policy (SNAP)Program Information Notice and TSCA/SNAP Addendum*. Retrieved from https://19january2017snapshot.epa.gov/sites/production/files/2017-01/documents/snapinformationnoticeinstructions2011.pdf

UNEP. (2016). Amendment to the Montreal Protocol on Substances that Deplete the Ozone Layer, Kigali, 15 October 2016. Retrieved May 22, 2021, from https://ozone.unep.org/treaties/montreal-protocol/amendments/kigali-amendment-2016-amendment-montreal-protocol-agreed

US EIA. (2016). Commercial Buildings Energy Consumption Survey (CBECS) - Table C13. Total electricity consumption and expenditures, 2012. Release date: May 2016. Retrieved from Table C13. Total electricity consumption and expenditures,2012 website: https://www.eia.gov/consumption/commercial/data/2012/

US EIA. (2020). Frequently Asked Questions (FAQs) -How much electricity is used for cooling in the United States? Retrieved May 22, 2021, from Annual Energy Outlook 2021 website: https://www.eia.gov/tools/faqs/faq.php?id=1174&t=1

Wang, S. P., & Chato, J. C. (1995). Review of recent research on heat transfer with mixtures - part I: condensation. *ASHRAE Transactions*, *61801*(1), 1376–1386.

Wang, C. C., Fu, W. L., & Chang, C. T. (1997). Heat transfer and friction characteristics of fin-and-tube heat exchangers. *Experimental Thermal and Fluid Science*, *14*(2), 174–186. https://doi.org/10.1016/S0017-9310(99)00229-X

Wang, D., Liu, C., Yu, D., & Chen, J. (2016). Influence factors of flow distribution and a feeder tube compensation method in multi-circuit evaporators. *International Journal of Refrigeration*, *73*, 11–23. https://doi.org/10.1016/j.ijrefrig.2016.09.011

Wattelet, J. P., Chato, J. C., Christoffersen, B. R., & Gaibel, J. A. (1994). *Heat Transfer Flow Regimes of Refrigerants in a Horizontal-Tube Evaporator* (Vol. 61801). Urbana, USA.

Winterton, R. H. S. (1998). Where Did the Dittus and Boelter Equation Come From? *International Journal of Heat and Mass Transfer*, (41), 809.

Xie, G., Wang, Q., & Sunden, B. (2009). Parametric study and multiple correlations on air-side heat transfer and friction characteristics of fin-and-tube heat exchangers with large number of large-diameter tube rows. *Applied Thermal Engineering*, *29*(1), 1–16. https://doi.org/10.1016/J.APPLTHERMALENG.2008.01.014

Yu, B., Ouyang, H., SHI, J., LIU, W., & CHEN, J. (2021). Evaluation of low-GWP and mildly flammable mixtures as new alternatives for R410A in air-conditioning and heat pump system. *International Journal of Refrigeration*, *121*, 95–104. https://doi.org/10.1016/j.ijrefrig.2020.09.018

Zühlsdorf, B., Jensen, J. K., Cignitti, S., Madsen, C., & Elmegaard, B. (2018). Analysis of temperature glide matching of heat pumps with zeotropic working fluid mixtures for different temperature glides. *Energy*, *153*, 650–660. https://doi.org/10.1016/j.energy.2018.04.048d.

APPENDIX A

PHOTOGRAPHS OF EXPERIMENTAL FACILITY

This section shows various photographs of the novel experimental facility to test fin-and-tube heat exchangers that has been detailed in chapter 2. Figure A.1 shows a photograph of the pumped refrigerant loop, indicating some of the key components that are used to condition the refrigerant loop before it enters the test section.
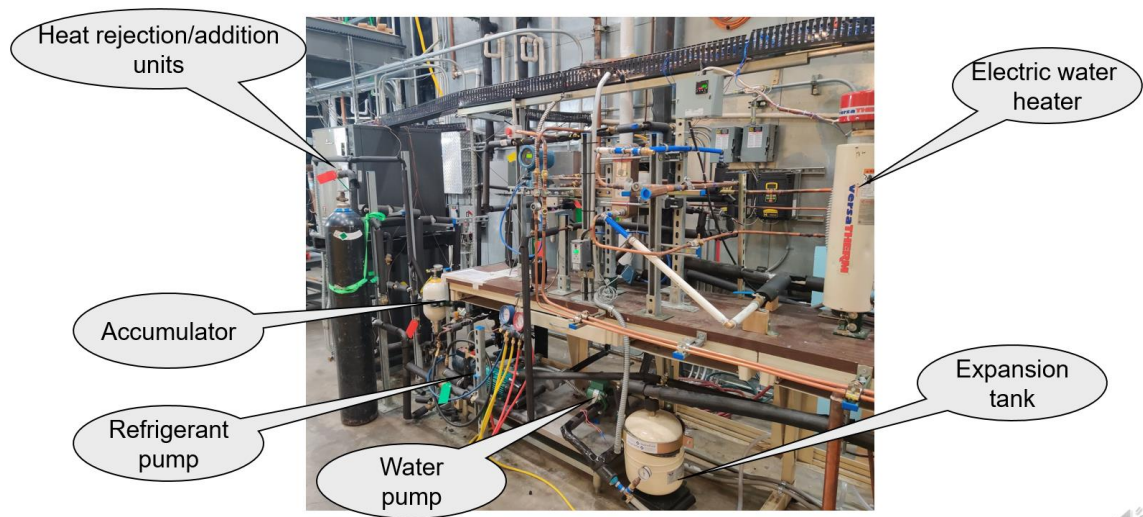

Figure A.1. Photograph highlighting the key components of the pumped refrigerant loop

Figure A.2 shows the test section of the experimental setup in the psychrometric chamber, namely duct B, which is used for testing coil #3. Details of test duct B, and coil #3 are in Table 3.1, and Table 3.3, respectively.
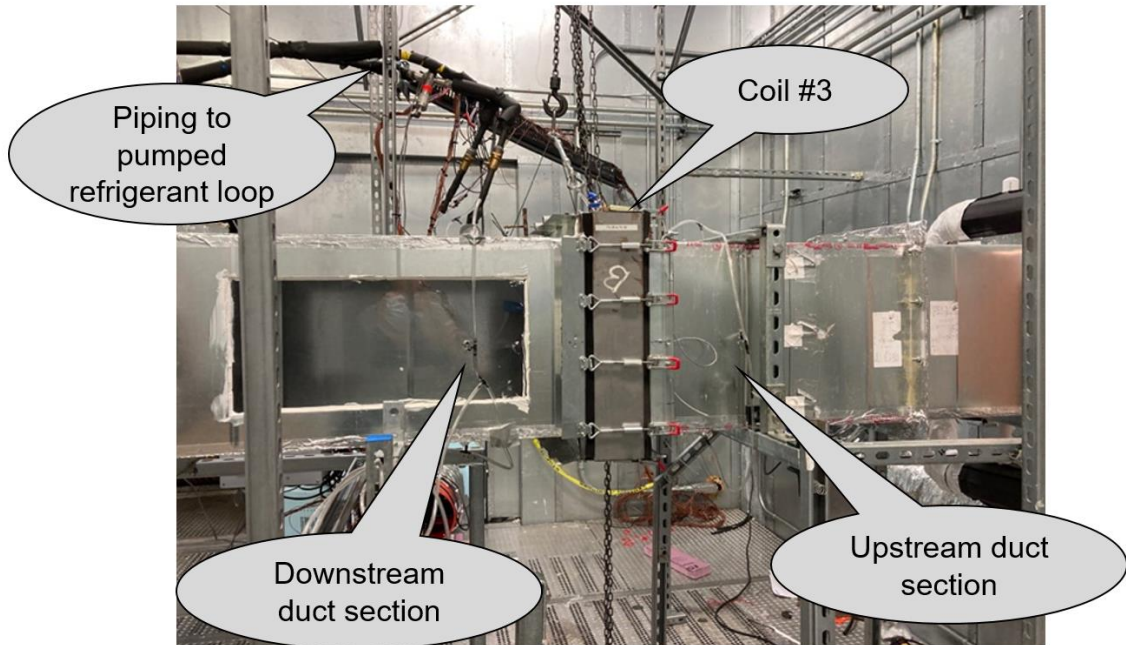
Figure A.2. Photograph of test duct B, housing coil#3

APPENDIX B

REFRIGERANT INLET PRESSURE SETTING ALGORITHM

This section outlines the development of a new feature added to the cross-fin (Xfin) model, which is basically an iterator that ensures that the correct inlet refrigerant pressure is provided to the model simulations.

B.1 Motivation

For the Xfin model, in addition to the refrigerant circuitry and geometrical details of the simulated test coils, several air and refrigerant side parameters are provided as inputs. These inputs are shown in Table B.1.

Table B.1. Air and refrigerant side operational parameters provided to Xfin model for simulations

Fluid	Parameter
Refrigerant	Mass flow rate (kg/s)
	Liquid line pressure (kPa)
	Inlet pressure (kPa)
	Liquid line temperature (K)
Air	Volumetric flow rate (m^3/s)
	Relative humidity ($\leq$ 1)
	Inlet pressure (Pa)

The refrigerant liquid line pressure is measured by a pressure sensor mounted on the setup that is upstream of the Electronic Expansion Valves (EXVs), as shown in Figure 2.3 in chapter 2.

However, for the first two test coils, namely coils#1 and #2, that were tested in duct A (see Table 3.1 in chapter 3) the experimental setup lacked a pressure downstream of the EXVs, in order to measure the pressure of the two-phase refrigerant entering the test coil.

B.2 Flowchart of inlet refrigerant pressure iterator

In order to address the issue explained above, an iterating algorithm was developed, as shown in Figure B.1 which used the outlet refrigerant pressure as a starting guess value for the Xfin model simulation. The simulated outlet refrigerant pressure would then be compared to the experimental outlet refrigerant pressure, and the iterator would increase the inlet pressure until simulated and experimental refrigerant pressures matched within a certain tolerance.

Start

Inputs (geometrical params, air and ref. flow rates etc.)

$P_{ref,in,init} = P_{ref,exit,exp.}$

Solve coil using **Xfin** model

$P_{ref,in,upd} = P_{ref,in,init} + \Delta P$

No

$(P_{ref,exit,sim} - P_{ref,exit,exp.}) \leq \epsilon$

Yes

End

$P_{ref,exit,exp.}$	Experimental outlet refrigerant pressure
$P_{ref,in,init}$	Initial inlet refrigerant pressure
$P_{ref,exit,exp.}$	Simulated outlet refrigerant pressure
$P_{ref,in,upd}$	Updated inlet refrigerant pressure
ΔP	Difference between $P_{ref,in,init}$ and $P_{ref,exit,sim}$

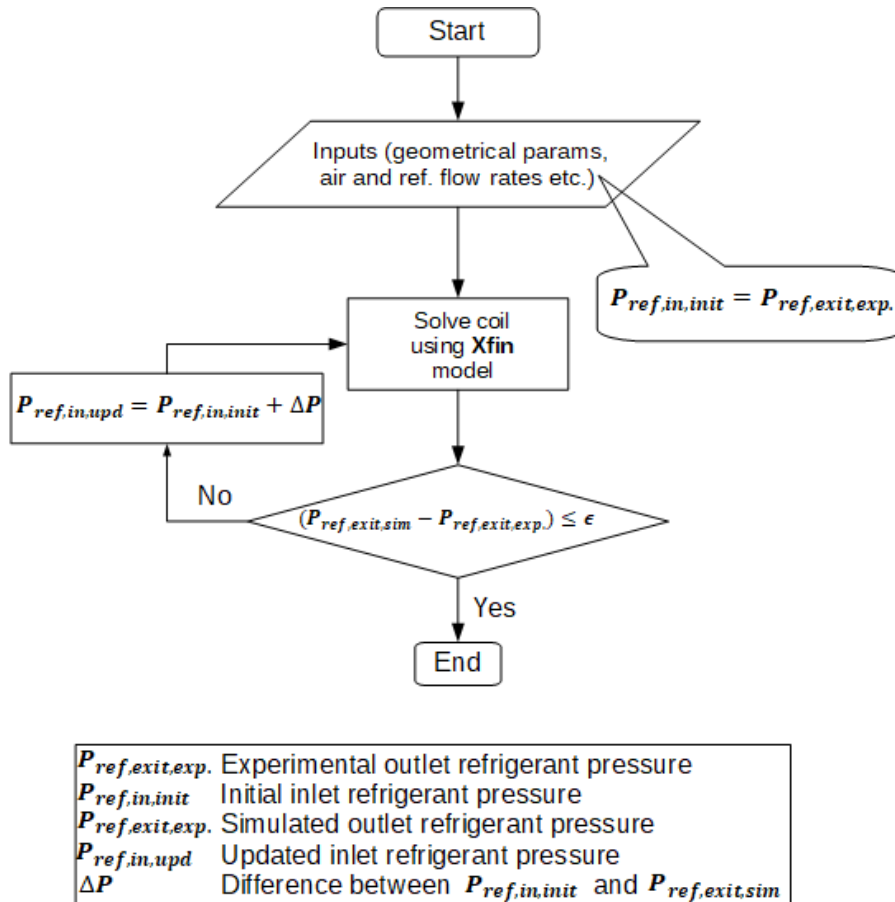Figure B.1. Flowchart showing the inlet refrigerant setting iterator

APPENDIX C

TWO PHASE REFRIGERANT HEAT TRANSFER AND PRESSURE DROP CORRELATIONS FOR R1234ZE(E)

When the cross-fin (Xfin) model was initially developed, the heat transfer and pressure drop correlations implemented were mainly to prioritize simulations with R410A, as detailed in Sarfraz (2019). However, these correlations were revisited when R1234ze(E) was implemented in the model. A literature survey was done to identify which commonly available correlations best predicted the behavior of R1234ze(E) in the two-phase regime. Experimental data was then extracted from the research articles, and compared to the in-house predictive implementation of the correlation in Python.

C.1. Two phase heat transfer correlation verification

Grauso *et. al.* (2013) did several experiments with R1234ze(E) and R134a in a smooth circular tube to observe how correlations available in open literature compared with their results of local heat transfer coefficients and frictional pressure gradients. They concluded that Shah (1982) had the best statistical agreement with their experimental data. Equation (C.1) provides the chart correlation in Shah (1982) for saturated boiling heat transfer.

$$\psi = \frac{h_{TP}}{h_l}, \ h_l = 0.023 \, Re_l^{0.8} \, Pr_l^{0.4} \frac{k_l}{D} \ \text{ for } \ 0.6 \leq \text{Pr} \ \leq 160, Re \geq 10{,}000 \ \& \ \frac{L}{D} \geq 10$$

where:

For $N > 1$

$$\psi_{nb} = 230 \, Bo^{0.5} \text{ for } Bo > 0.3 \times 10^{-4} \ , \quad \psi_{nb} = 1 + 46 \, Bo^{0.5} \text{ for } Bo < 0.3 \times 10^{-4}$$

(C.1)

$$\psi_{cb} = \frac{1.8}{N^{0.8}}$$

$$\psi = \max(\psi_{nb}, \psi_{cb})$$

For $0.1 < N \leq 1.0$

$$\psi_{bs} = FBo^{0.5} \exp(2.74\, N^{-0.1})$$

$$\psi = \max(\psi_{nb}, \psi_{cb})$$

For $N \leq 0.1$

$$\psi_{bs} = FBo^{0.5} \exp(2.47\, N^{-0.15})$$

$$\psi = \max(\psi_{nb}, \psi_{cb})$$

For $Bo \geq 11 \times 10^{-4}, F = 14.7\,\&\,\, Bo < 11 \times 10^{-4}, F = 15.43$

Figure C.1 shows the comparison of the experimental heat transfer correlation in Grauso *et. al.* (2013) with the predicted values, as a function of quality (dryness fraction). The percentage difference between experimental and predicted values was found to be less than -10% on average.
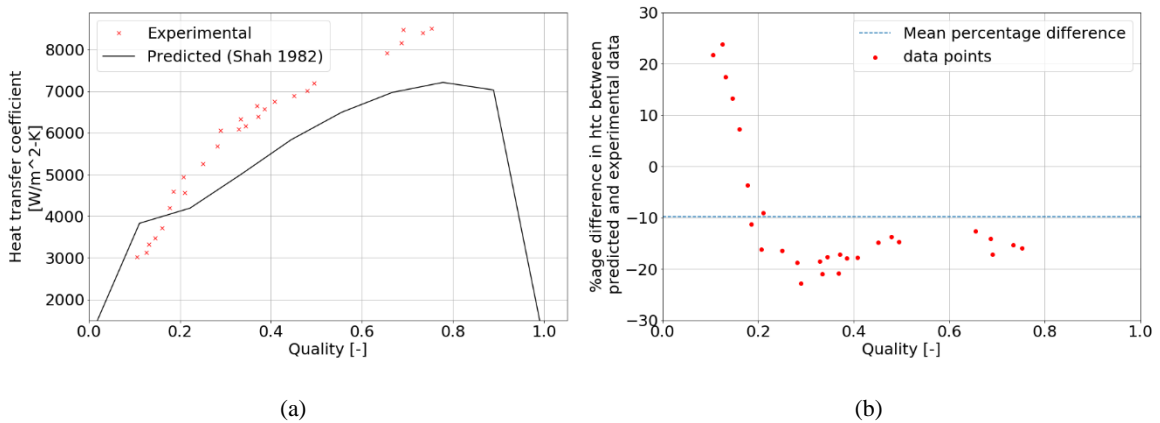

(a)

(b)

Figure C.1. (a) Comparison and (b) percentage difference of heat transfer coefficient predicted using correlation with predicted and experimental values in Grauso *et. al.* (2013)

C.2. Two phase pressure drop correlation verification

Grauso *et. al.* (2013) found that the best agreement of their experimental data for pressure drop in the two phase regime with R1234ze(E) was with the Friedel (1979) correlation. Equation (C.2) shows the Friedel (1979) correlation.

$$\Delta P_{frict} = \Delta P_L \phi_{fr}^2$$

$$\Delta P_L = 4f_L \left(\frac{L}{d_i}\right) \dot{m}_{ref}\left(\frac{1}{2\rho_L}\right)$$

$$f = \frac{0.079}{Re^{0.25}}, Re = \frac{\dot{m}_{ref}d_i}{\mu}$$

$$\phi_{fr}^2 = E + \frac{3.24FH}{Fr_H^{0.045}We_L^{0.035}}$$

$$Fr_H = \frac{\dot{m}_{ref}^2}{gd_i\rho_H^2} \tag{C.2}$$

$$E = (1-x)^2 + x^2(\rho_L f_G)/(\rho_G f_L)$$

$$F = x^{0.78}(1-x)^{0.224}$$

$$H = \left(\frac{\rho_L}{\rho_G}\right)^{0.91} \left(\frac{\mu_G}{\mu_L}\right)^{0.19} \left(1 - \frac{\mu_G}{\mu_L}\right)^{0.7} for \frac{\mu_L}{\mu_G} < 1000$$

$$We_L = \dot{m}_{ref}^2 d_i/\sigma\rho_H$$

$$\rho_H = \left(\frac{x}{\rho_G} + \frac{1-x}{\rho_L}\right)^{-1}$$

Figure C.2 shows the comparison of the experimental pressure drop in Grauso *et. al.* (2013) with the predicted values, as a function of quality. The percentage difference between experimental and predicted values was found to be less than 32% on average.

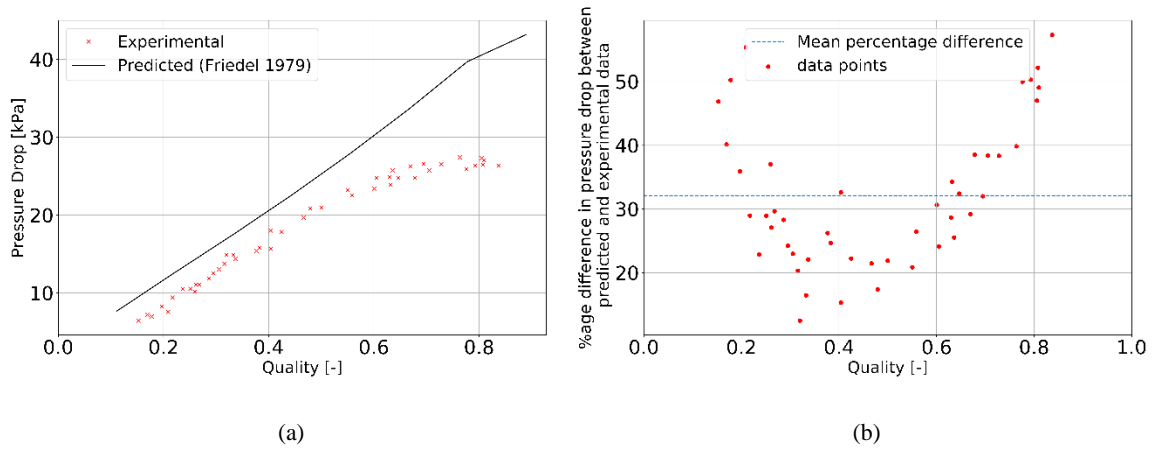(a)   (b)

Figure C.2. (a) Comparison and (b) percentage difference of pressure drop predicted using correlation with predicted and experimental values in Grauso *et. al.* (2013)

VITA

SAAD SALEEM

Candidate for the Degree of

Doctor of Philosophy

Dissertation: PREDICTING AND TESTING THE PERFORMANCE OF NEXT
GENERATION HEAT EXCHANGERS WITH LOW-GWP REFRIGERANTS

Major Field: Mechanical Engineering

Biographical:

Personal Data: Born in Lahore, Pakistan, in August 1990.

Education:
Completed the requirements for the Doctor of Philosophy in Mechanical
Engineering at Oklahoma State University, Stillwater, Oklahoma in
December 2021.

Received a Master's of Science in Renewable Energy (InnoEnergy double
degree program) at Polytechnic University of Catalonia (UPC) in Spain, and
KTH Royal Institute of Technology in Sweden in October 2016, and a
Bachelor's of Science in Mechanical Engineering at UET (Lahore) in
Pakistan in September 2013

Experience:
Worked as Concentrated Solar Power Engineer at ZED Solar Ltd, Pakistan
(Oct 2016-July 2017).
Master thesis intern at Catalonia Institute for Energy Research (IREC),
Spain (Feb 2016-July 2016).
Trainee Engineer of operations at Lalpir Thermal Power Ltd., Pakistan
(Sept 2013-July 2014).

Professional Memberships:
Student member ASHRAE